ISSN…..

STATE ATOMIC ENERGY CORPORATION ROSATOM

S C “A.A.Bochvar High-technology Research Institute of Inorganic Materials”

VOPROSY ATOMNOY NAUKI I TEKHNIKI

(ASPECTS OF NUCLER SCIENCE AND ENGINEERING)

Materials Science and New Materials Series

ISSUE № 1 (97)

2019

An English Version of the Russian Edition

VANT 1 (97) 2019

METALLURGY AND METAL TECHNOLOGY

CHEMICAL ENGINEERING

ENERGY ENGINEERING

8**.** *Krupkin A.V., Kuznetsov V.I., Novikov V.V., Petrov O.M.*
Finite-element strength analysis of welded junctions of VVER reactor fuel elements

9. *Karasev Yu.V., Korpusov V.Yu., Salunin N.I., Malchenkov A.V., Shevyakova S.A., Gubkin I.N., Nikulenkov E.V., Lukyanov P.A., Polikarpova M.V., Konovalov Yu.V., Abdyuhanov I.M.*
A study of the current-carrying capability of Nb-Ti-based superconductors for CBM detector magnet

10. *Kozlova E.V., Sheverdyaev M.S., Semyonov A.A., Gorlevsky V.V., Laushkin A.V., Chebotarev A.A., Volkov V.V.*
X-ray studies of composite materials based on porous beryllium

DEDICATED TO THE MEMORY OF LEONID IVANOVICH PONOMARYEV

UDC 621.039.546.3

EFFECTIVE MEANS OF RADIATION PROTECTION

V.K. Orlov, Yu.A. Metyolkin, A.A. Maslov
SC «A.A. Bochvar High-Technology Research Institute of Inorganic Materials»,Moscow

Physical and mechanical properties of uranium and its alloys enabling the development of radiation-generating devices and transportation containers for safe operation and radionuclide transportation are presented. Confidence characteristics of uranium blanks obtained from residues are stated that allow to recycle residues and return items to operation following the expiration of their warranty period.

Keywords: depleted uranium metal, smelting, casting, gamma radiation, absorption, container, spent nuclear fuel, normal operating conditions, emergency conditions.

Domestically-produced radiation-generating machines, radiation-generating process control devices, shipping packaging sets (SPS) intended for the transportation of ionizing radiation sources and certain types of containers used for the transportation and storage of spent fuel that are currently in service (the majority of which was developed and manufactured in late 1960s and early 1970s as the means of biological protection using led and rare grades of stainless steel) no longer comply with a number of requirements of current GOST standards, sanitary regulations and requirements of IAEA [1, 2]. JSC VNIINM carried out comprehensive studies of properties of depleted uranium of various origins and developed a manufacturing process and launched the production of biological protection containers for transport packages [2]. The use of uranium as a functional structural material was dictated by the following definite advantages:

- due to its high density, depleted uranium has the capacity for absorption of gamma radiation 20 % than that of the best competing expensive tungsten-based alloys;
- depleted uranium in combination with other materials (stainless steel, titanium and VNM, VNZh and other tungsten alloys) may be used as structural biological protection blocks.

To demonstrate this statement, let us review estimated properties of the mass of alternative structural materials (depleted uranium, tungsten and led) when used in manufacturing radiation protection items of transport packages [3], Table 1.

TABLE 1

Comparative characteristics of structural materials

Structural materials	Loading socket diameter of SPS, cm			
	2.5	5.0	10.0	15.0
M(Pb)/M(U)	1.8	1.68	1.52	1.43
M(Pb)/M(W)	1.29	1.23	1.17	1.12

M(W)/M(U)	1.4	1.37	1.3	1.27
M(Pb), M(U), M(W) is the mass of radiation protection made of led, uranium and tungsten alloy, respectively				

These values were determined as the result of estimation of the radiation protection weight which should ensure the radiation protection factor K=10000, in terms of cobalt-60, for various diameters of the radioactive content loading socket. The data confirm that uranium allows to achieve protection with the best possible weight and size characteristics [4].

While designing, radionuclide composition of uranium should be taken into consideration, as well as the fact that uranium itself is a source of radioactive radiation. Two types of uranium are distinguished in terms of the enrichment level:

- natural-occurring ^{238}U, comprised of a mixture of nuclides of ^{235}U-0.71%, ^{234}U-0.0058% and other materials;

- uranium with depleted isotope ^{235}U, obtained from natural raw materials and recycled uranium reconditioned from SNF, which contains, apart from 0.2 to 0.4% of ^{235}U, fission fragments and the nuclides ^{232}U and ^{234}U. Other than its radionuclide composition, properties of depleted uranium are not dependent from its origin.

The main contribution to specific activity of depleted uranium is made by the 234 row, namely, by ^{234}Th, ^{234}Pa, ^{234}U. β and γ fields created by depleted uranium are distinguished. In order to ensure the compliance of hazard class and the radiation safety class required when working with uranium, content of uranium-232 should not exceed $0.2 \cdot 10^{-9}$%, and activity of plutonium – 2 Bq/g [4].

The value of gamma radiation amount created by depleted uranium lies within the level of permissible dose rate recommended by radiation safety regulations for category A persons. The experimentally measured amount of gamma radiation created by a depleted uranium plate with the thickness of 5 mm and the diameter of 80 mm is 1000 to 2000 mcR/h [5].

According to an IAEA's requirement, packaging sets intended for the transportation and storage of radionuclides shall be stable at high temperatures without losing their protective properties. The products are tested in an open flame at the temperature of 800°C, over 30 minutes. For this reason, studies of the behavior of uranium and some of its alloys in an open flame at temperatures of up to 900 °C were required. Since the effectiveness of uranium oxidation depends on the ratio of surface area to volume, experiments were conducted using specimens similar to real-life products. The results of the studies are shown in Table 2, which states data of weight change of specimens following one hour of exposure to air within the temperature range of 500-900°C, as well as values of material density in the initial condition [6].

TABLE 2

Change of mass of specimens following one hour of exposure to air, in %

Material	Test temperature, °C				Density, g/cm^3
	500	700	800	900	
Unalloyed uranium	6.0	6.2	8.2	22.0	18.8
Uranium and 0.5% Hf alloy	7.2	5.8	8.0	21.0	18.6

Uranium and 0.5% Cu alloy	6.6	4.1	6.5	-	18.5
Uranium and 1.0% Cu alloy	5.8	3.8	6.4	-	18.31
Uranium and 1.0% Hf alloy	8.0	5.4	7.1	9.0	18.67
Uranium and 1.2% Mo alloy	-	-	6.1	11.0	18.6
Uranium and 0.5% Cu + Hf alloy	4.8	4.0	6.6	-	18.38
Uranium and 0.5% Cu + 1% Hf alloy	5.4	3.8	7.5	8.4	18.33
Uranium and 0.5% Cu + 1.5% Hf alloy	5.2	4.6	8.0	-	18.32
Uranium and 1.5% Mo +1% Ti alloy	-	-	5.6	5.9	18.4
Uranium and 1.5% Mo +1% Zr alloy	-	-	4.0	7.0	18.5
Uranium and 1.5% Mo +1.5% Hf alloy	5.2	5.1	6.4	8.0	18.4
Uranium and 9.0% Mo alloy	-	-	2.0	8.0	17.08

It should be noted that none of the specimens exhibited material burn-up during the tests, and the change of mass was attributable only to the surface oxidation of the test specimens. The insignificant oxidation of uranium and, especially, of its alloys can be explained by the fact that a layer of uranium oxide/protoxide is formed at the surface. This layer prevents penetration of oxygen into the metal.

Since the oxidation efficiency depends on the ratio of the surface area and the volume, experiments were conducted on specimens of the same thickness as that of real-life products. No burn-up of the test specimens was observed in any of the cases. The comparatively low oxidation of uranium and its alloys could be explained by the fact that a layer of uranium oxide/protoxide formed at the surface prevents penetration of oxygen into the metal. The data were corroborated by the results of burning the metal residues out of crucibles. Specifically, it takes about 2 hours to burn 11 kg of uranium in oxidizing flame [7].

The developed designs of biological protection products involve encasing of uranium items in 12C18N10T grade stainless steel. It is known that uranium and iron at 725°C form a eutectic mixture. Nevertheless, there are certain data indicating that the oxidated surface of uranium prevents the formation of a eutectic mixture on contact with steel at heating temperatures of up to 1000°C. This allows to use equipment made of ferrous alloys in smelting. Design calculations of biological protection structures of shipping packaging sets (SPS) demonstrate that if a container is subjected to “fire conditions” the temperature at the interface of steel and uranium does not exceed 600°C. This implies that the probability of the development of a liquid eutectic mixture of a SPS under “fire conditions” is virtually nonexistent [4].

To neutralize radiation of depleted uranium in biological protection structures, uranium parts must be encased in corrosion-resistant steel with the thickness of 1.5 mm and coated

with a standard Al-Zn-corundum powder modified by replacing corundum with boron carbide B_4C using the method of cold gas dynamic spraying.

Following the tests, the cast structure of alloys which demonstrates a pronounced pine-tree structure remained practically unchanged.

Industrial-scale production of packaging sets UKT1V-60-1, UKT1V-60-10 and UKT1V-60-100 was launched in Russia. These sets are intended for transportation by air and storage of enclosed radionuclide radiation sources based on cobalt-60 with the activity of up to $3.7 \cdot 10^{10}$ Bq (1 Cu), $3.7 \cdot 10^{11}$ Bq (10 Cu) and $3.7 \cdot 10^{12}$ Bq (100 Cu). The mentioned containers have been actively used in RIAR since 1998. A patent of the Russian Federation was issued for the container design, and the Ministry of Nuclear Energy issued permission certificates. These are products featuring increased mechanical stability and temperature resistance, they eliminate the possibility of loss and dispersal of radioactive contaminants, provide effective protection from radiation in emergencies during transportation caused by temperature and mechanical effects [7, 8].

Conclusions

1. The use of depleted uranium as a means of biological protection from ionizing radiation allows to improve weight and dimensional properties of transportation packaging sets and radiation generating devices, improve their protection under extreme conditions and enhance transportation and storage safety.

2. Reliable characteristic values for cast uranium blanks were obtained that use recycled residues of uranium manufacture, parts of medical products returned following warranty period expiration and special-purpose military products for production. It was demonstrated for the first time ever that no combustion of uranium or formation of low-melting eutectic mixtures occurs when using the products or in emergencies.

3. Depleted uranium emits radiation, with gamma and beta fields developing following the decay of daughter products: uranium-238, thorium-234 ekatantalum-234. The dose rate lies within the range of values permissible for category A of personnel subjected to radiation, according to Radiation Safety Standards NRB 99. To ensure protection from particle streams, it is sufficient to provide screening with stainless steel sheets no more than 1.5 mm thick.

References

1. Radiation Safety Standards (NRB 99). SP2.6.1 758-99 Ministry of Health of the Russian Federation 1999.

2. Orlov V.K., Metyolkin Yu.A., Semyonov A.G. Uranium in the national economy. Overview. Issue 3 (162), M., VNIINM, 1999.

3. Reliable biological protection from radiation. Depleted uranium. An advertising leaflet of JSC CMP, 1992.

4. Orlov V.K., Metyolkin Yu.A., Maslov A.A. Protective materials with increased absorption of gamma-radiation. Uranium metal - Atomic energy, 2014, 117, issue 6, pp. 266-269.

5. Metyolkin Yu.A., Orlov V.K. Biological protection based on depleted uranium. Problems of atomic research and industry. 2000., issue 1157, pp. 26-30.

6. Orlov V.K., Metyolkin Yu.A., Semyonov A.G. Use of depleted uranium as biological protection. Perspektivnye Materialy-2003, issue 6, pp. 37-42.
7. Biryukov S.I., Metyolkin Yu.A. Smelting and casting of uranium and its alloys. – M.: Energoatomizdat. 1983.
8. Permission certificate issued for UKT1V-60-1 RU047 No. VSI-85.

UDC 621.039

SIMULATION OF IONIZING RADIATION PROTECTION USING AN ALUMINUM-BASED COMPOSITE MATERIAL

D. O. Ivanov[1] , A.Yu. Gradoboyev[1], R.O. Vakhromov[1], A.Z. Kariov[2], K.N. Inkina[2]
[1] Institute of Light Materials and Technologies, LLC (ILM&T, LLC), Moscow,
[2]The Dimitrovgrad Division of Federal Center for Nuclear and Radiation Safety JSC (FCNRS JSC), Dimitrovgrad

The article discusses the prospects of application of an aluminum-based composite material with the addition of boron carbide (Al - 60% wt, B4C), used in structural elements of shipping packaging sets (SPS) used in transportation of spent nuclear fuel (SNF) as a means of protection from ionizing radiation. The model of an SPS used for transportation of spent fuel assembly (SFA) of a WWER-1200 reactor is considered as the simulation model selected for the estimation of the effective dose intensity (DI) of neutron and gamma radiation. The results of DI estimation showed that the proposed design provides nuclear and radiation safety of package under normal operating conditions as per the requirements of NP-053-16.

Keywords: simulation, ionizing radiation, shipping packaging set, spent nuclear fuel, aluminum-based composite material, boron carbide.

Introduction

Due to the growing number of commissioned NPP units and, consequently, to the increased amounts of spent nuclear fuel, ensuring the rate of transportation of SNF from storage facilities of NPPs to reprocessing facilities or for long-term storage is a crucial objective of today's nuclear industry. Presently, containers and carriers that belong to series 13 are used for the transportation of spent fuel assemblies (SFA) from NPPs equipped with WWER-1000 reactor systems [1].

SPS-13 was developed for transportation of SFA with fuel enrichment levels of up to 4.4 % in terms of uranium-235, fuel burn-up of up to 50 MW·day/kgU and the decay heat 1.67 kW. However, fuel assemblies have been improved over the recent years: the initial fuel enrichment level and the length of fuel column have been increased, fuel burnup has been improved and the operation mode of the new generation reactors has been changed. Besides, SPS-13 have a number of disadvantages, such as the availability of only a single protective cap, the use of liquid neutron protection and a relatively low capacity (12 SFAs). Consequently, SPS-13 should not be part of the design of new NPPs since it is not designed for the transportation of fuel assemblies of WWER-1200 reactors. Thus, the necessity to develop SPS of a new generation has arisen. These SPS should be compliant with modern requirements to radiation and nuclear safety in transportation of new types of SFA [2].

This task requires materials that would provide a high degree of protection and have improved mechanical properties. Aluminum-based composite materials (CMs) meet these requirements exhaustively: they have high corrosion-resistance and mechanical properties, low specific weight and a much higher thermal conductivity as compared with the existing materials. This is important in applications of SPS for transportation and storage of SNF with increased heat production. Besides, the principle of reinforcing the matrix material with a functional filling material enables to create materials providing comprehensive protection from various types of ionizing radiation by changing the filler.

Presently, a growing number of studies is performed using simulation. Despite the high cost of software this enables to reduce costs related to non-essential consumables and technology cycles.

This article studies the effect of boron carbide content, being a compound, which provides a high protection level from ionizing radiation, on the level of protection from neutron radiation when used as structural material of SPS, the novel design used for both transportation and storage of SNF. The study is carried out using the simulation method. A composite material of experimental composition was used as the means of radiation protection of the SPS. The composition includes 40% wt of boron carbide.

Simulation model description

In order to evaluate the advisability of application of the aluminum-based composite material doped with boron carbide as a radiation protection material, DI of neutron and gamma radiation were estimated in the vicinity of the SPS.

Spent nuclear fuel is a source of ionizing neutron and photon radiation. Neutron radiation is emitted as the result of spontaneous fission of actinides, as well as the result of the reaction (α,n) with oxygen nuclei. Photons are emitted mainly during the radioactive decay of nuclear fuel fission products and activation products of steel structural elements of SFA.

To estimate the intensity of radiation sources, the actual fuel burn-up of 56 MW·day/kgU and the SFA storage period of 9 years were assumed. The SPS includes: (i) a container, which is the main component of the structure, which provides the space for SFA storage, radiation protection of the personnel and population, prevents radionuclides from escaping the container and dissipates the residual heat generated by SFA into the environment; and (ii) casing placed within the container. It provides radiation protection, ensures orderly arrangement of eighteen SFAs, prevents the possibility of an self-sustaining chain reaction (SSCR) development and maintains geometrical dimensions of the SFA. The SPS casing is enclosed in the composite material of 13.5 cm thickness. The container is closed by two caps, the outer and the inner ones. These are made of stainless steel.

In the development of the simulation model, a number of simplifications was assumed. These do not affect the final result and are in line with the conservative concept. These simplifications are as follows: fixtures (nuts, pins etc.) and stud bolts were not simulated; SFAs were simulated as homogeneous both in the fuel section and in the head and back end areas; and transportation cushions were not taken into account.

Simulations used the Monte Carlo technique implemented using the Scale version 6.2.3. software suit [3]. The Monte Carlo technique is the most universal method applied in the simulation of emissions. The essence of the method lies in tracing every particle which leaves the source, from its origination to extinction (absorption, leak etc.). Particle travel is simulated on the basis of a selection of quasi-random numbers by estimating the probabilities of interaction of particles of this type with the substance.

Analysis of the obtained results

The spatial distribution of dose intensity radiated by SPS is shown in Fig. 1 and Fig. 2.

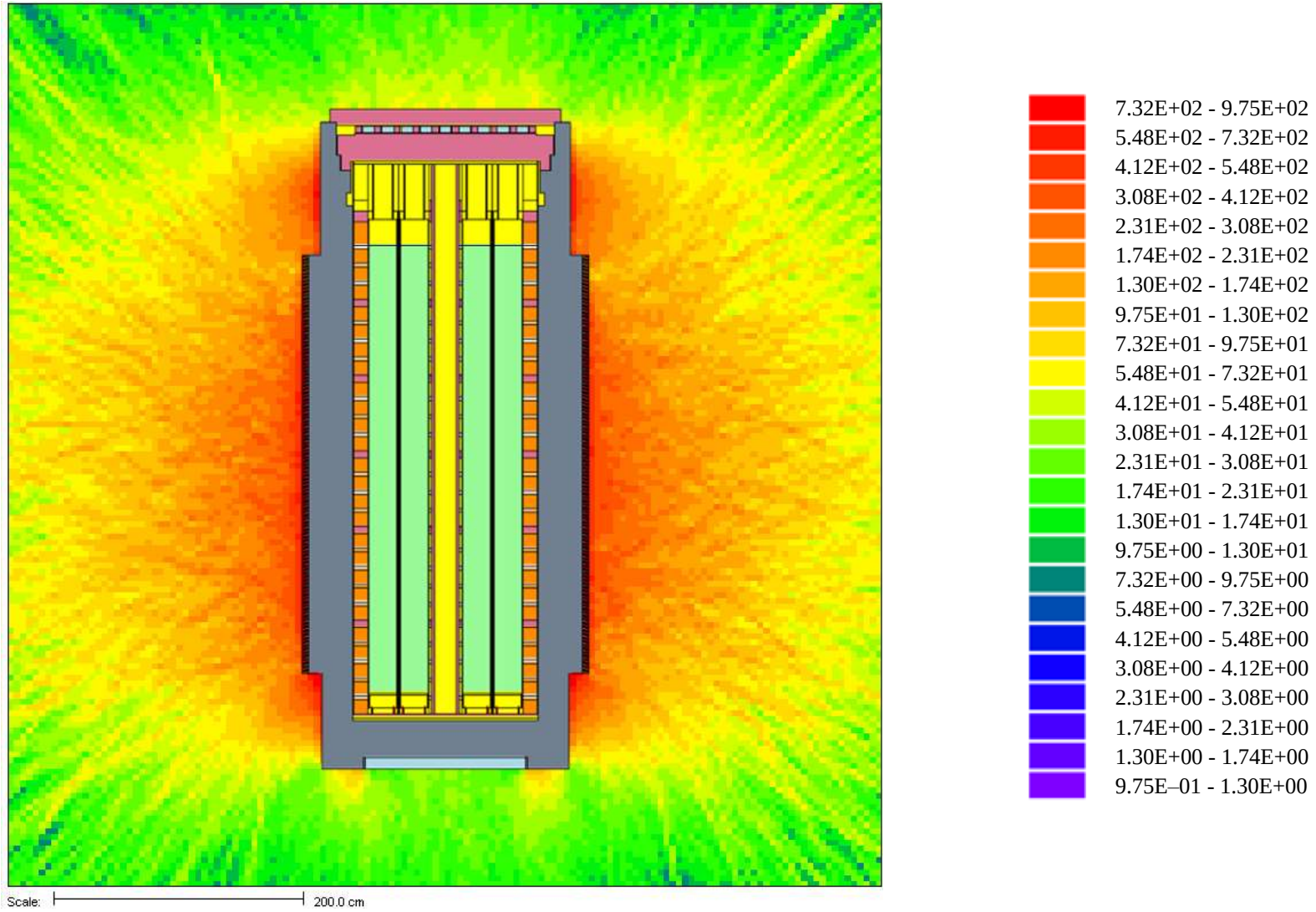

FIG. 1. Distribution of dose intensity depending on neutron radiation of SFA (uSv/h)

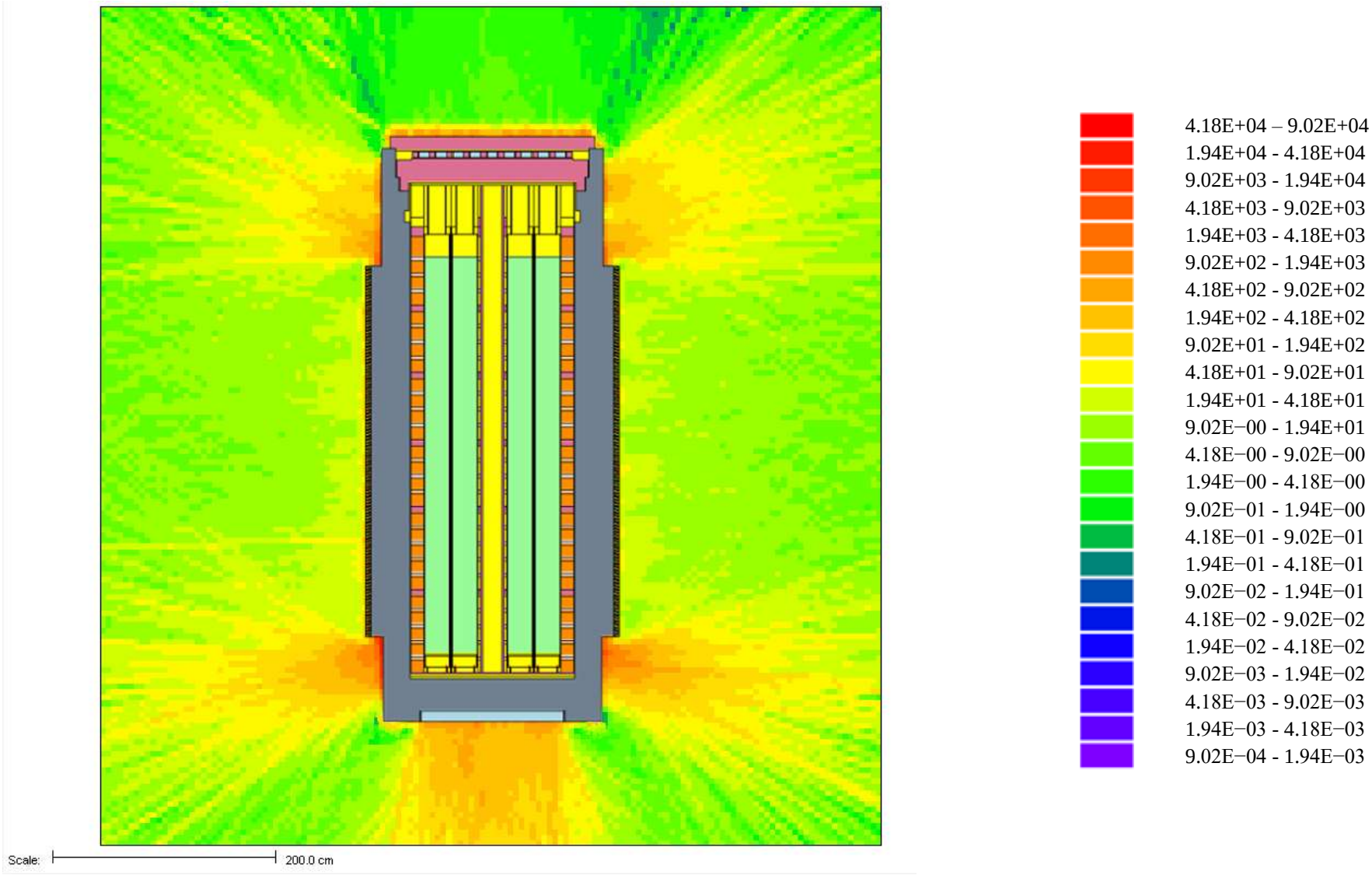

FIG. 2. Distribution of dose intensity depending on photon radiation of SFA (uSv/h)

The estimated maximum values of dose intensity and maximum allowable levels are shown in Table 1.

TABLE 1

Estimated and maximum allowable dose intensity
(the estimated values are stated with consideration of statistical uncertainty (+2σ))

Dose intensity recoding area	Maximum estimated dose intensity, mSv/h	Maximum allowable dose intensity, mSv/h
At the surface of the SPS	0.460	2
At the surface of the SPS transporter vehicle	0.308	2
At the distance of 1 m from the side surface of the SPS	0.093	–
At the distance of 2 m from the side surface of the SPS	0.076	0.1

The analyzed composition provides complete radiation safety with the permissible dose intensity of 2 mSv/h at the surface of the package and 0.1 mSv/h at the surface of 2 m from the surface of the package.

The neutron multiplication factor values were used in the analysis of nuclear safety. The effective neutron multiplication factor k_{eff} for any item of equipment containing fissionable materials shall not exceed 0.95.

The results of estimation of k_{eff} (taking into consideration statistical uncertainty (+2σ)) for normal operating conditions depending on the density of water in the container are shown in Table 2.

TABLE 2

The results of the estimation of neutron multiplication factor

Water density, kg/m^3	0.0	0.1	0.2	0.3	0.4	0.5	0.6	0.7	0.8	0.9	1.0
Value of k_{eff}	0.264	0.504	0.644	0.729	0.790	0.830	0.863	0.891	0.912	0.931	0.949

As we can see, the neutron multiplication factor does not exceed the permissible value of 0.95 under normal transportation and storage conditions of SFA of a WWER-1200 reactor in the SPS.

The obtained results evidence that the proposed design of SPS which uses the composite material Al-40 % wt B_4C for SNA of VVER-1200 ensures compliance with requirements of nuclear and radiation safety under normal operating conditions of the package.

References

1. Spent nuclear fuel and NPP radioactive waste treatment / M.A. Skachek. – M. : MEI Publishing, 2007.
2. Problems of transportation of WWER-1000 SNF Yu. V. Kozlov et al. Lecture at IX International Conference ATOMTRANS-2006, Saint Petersburg, 2006
3. Scale: A Comprehensive Modeling and Simulation Suite for Nuclear Safety Analysis and Design. Oak Ridge National Laboratory, 2018.

UDC 621.791.5/.7:[626.02:627.02].001.5

EVALUATION OF ABSORPTION CAPACITY OF METAL TARGETS FOR LASER-BEAM CUTTING IN AQUEOUS MEDIUM

M.V. Konyukhov[1], E.S. Shitova[1], A.S. Bykov[1], D.A. Podgorniy[1], A.A. Pertsev[2]
[1]FSEI HE National University of Science and Technology MISIS, Moscow
[2] SC A A. Bochvar High Technology Scientific Research Institute for Inorganic Materials Moscow

The study investigates the model used to evaluate the absorption capacity of metal targets in laser-beam machining under water at various hydrostatic pressure of the environment. The results of absorption capacity simulation for a number of pure metals are presented.

Keywords: laser radiation, aqueous medium, metals, Drude model, absorption capacity.

To achieve the required power density in laser-beam machining of metal surfaces, the optical system must form a small-radius light spot. The resulting intensity, the rate of energy input and, as the result, the rate of heating follow a specific dependency, and may vary in time. When laser radiation (LR) interacts with the surface of a material, only a portion of the applied energy is absorbed. As the result, a source of heat is formed and its characteristics are determined by a set of physical properties of the material and parameters of the LR. Generally, the heat from the surface of the source having the given symmetry permeates the solid body and heats it. The developing processes are generally nonlinear since in real-life conditions there is a significant dependency of the essential physical properties (optical, thermophysical, mechanical etc.) on the temperature. Thus, when simulating these processes, the nature of changes in these properties and their contribution to the general dynamics of the process must also be taken into account.

In the last decade, the use of LR in the processing of materials in aqueous media, e.g., in water, has become particularly promising.

Presently, there exist two approaches to underwater laser cutting: involving the formation of a dry zone at the machining location using a service gas stream [1-6], and exposing the material to LR directly through a layer of water [7-17]. It should be noted that the use of the method involving a dry zone has some severe limitations in terms of the process operation depth. This is mostly due to the presence of high-pressure gas systems. For this reason, the method of direct action of LR through a layer of water is more promising.

Interaction of LR with a material under conditions other than vacuum may be subject to a significant effect of properties of the gaseous or aqueous media and the type of interaction between the radiation and the surface material on the nature of developing processes. In this case, the effect of physical properties of the environment must also be considered due to their significant influence on the process of machining. These properties include chemical

composition, pressure and presence of flows. Another issue which must be considered is the significant heat transmission coefficient at the interface of the media.

In order to determine the nature and contribution to the process of machining of metallic materials by LR from a given source within an aqueous medium (e.g., in water), the dynamics of absorption capacity variation of the material depending on the temperature at the machining spot and the external hydrostatic pressure must be evaluated.

The nature of the metal target heating by LR within a given wavelength range is primarily determined by the absorption capacity which, in its turn, is determined by optical properties of the metal and the nature of the surface, as well as the temperature of the target, the exposure mode, etc. For this reason, the absorption capacity A and the reflective capacity R of the metal are the major criteria in the selection of the effective wavelength.

Metals typically manifest growth of absorption capacity with the decrease in emission wavelength from the infrared to the ultraviolet spectrum region. On the other hand, low values of absorption capacity of metals appear to make the use of laser radiation generators at wavelengths lying within the infrared region ineffective in the processing of metals. However, as practice shows, the value of absorption capacity grows significantly in the irradiation zone in the process of laser action due to an increase of the target temperature (as well as a number of other physical processes). Considering the above, research of physical phenomena that characterize the dynamics of absorption capacity variation in the process of machining is an important problem.

The value of absorption capacity of metals may be evaluated with the use of the relaxation model, or the Drude model. The Drude formalism [16] is based on the assumption that absorption of electromagnetic energy by metals occurs at the skin layer and is effected by electrons that pass their energy to the lattice as the result of collision.

In this study, the absorption capacity of metal targets was evaluated at wavelengths, and respective circular frequencies as stated in Table 1.

TABLE 1

Wavelengths λ and respective circular frequencies ω

λ, nm	1060	532	470
$\omega \cdot 10^{15}$, rad/s	1.77	3.54	4

According to the Drude relaxation model, the nature of absorption capacity of metals depends on the correlation of the circular frequency of laser radiation (ω), the relaxation frequency (G) and the plasma frequency (ω_p). Thus, depending on the nature of the metal and the circular frequency of LR, the absorption coefficient is determined based on the following three model cases:

1. Absorption capacity at $\omega^2 > \Gamma^2$:

$$A_D(T) = \frac{2\Gamma}{\omega_p}. \quad (1)$$

2. Absorption capacity at $\omega^2 \sim \Gamma^2$:

$$A_D(T) = \sqrt{\left(\frac{2\omega}{\pi\sigma_0}\right)\left[\sqrt{1+\omega^2\tau^2} - \omega\tau\right]}. \quad (2)$$

3. Absorption capacity at $\omega < \Gamma$:

$$A_N = \sqrt{\frac{2\omega}{\pi\sigma_0}}, \quad (3)$$

where σ_0 is the specific metal conductivity.

The value of G determines electron relaxation frequencies and is defined as follows:

$$\Gamma = \Gamma_{ep} + \Gamma_{ee} + \Gamma_{ed}, \quad (4)$$

where G_{ep} is the collision frequency of electrons and photons,

Γ_{ee} is the collision frequency of electrons with other electrons, and

G_{ed} is the collision frequency of electrons and defects.

A metal target is heated by laser radiation as the result of work performed by electrons under the action of electromagnetic fields at the skin layer. In their turn, the electrons pass energy to the lattice as the result of collisions that have the periodicity of t, which is related to G by the following correlation:

$$\tau = \frac{1}{\Gamma}. \quad (5)$$

Absorption capacity is related to the reflective capacity as follows:

$$A_D = 1 - R_D. \quad (6)$$

In the process of energy accumulation by the lattice, i.e., heating of the material, the length of free pass of electron in the skin layer l_e increases. This leads to a change in absorption capacity. Based on the above, A is represented as follows in order to account for the absorption mechanisms:

$$A = A_D + A_N. \quad (7)$$

For a constant electric field at ω=0 and laser radiation frequencies that satisfy the correlation of ω<<G, the relaxation frequency may be determined using the Lorenz Sommerfeld correlation [16]:

$$\sigma = \frac{n_e e^2}{m^* \Gamma}. \quad (8)$$

thus,

$$\Gamma = \frac{n_e e^2}{m^* \sigma}, \quad (9)$$

where n_e is the concentration of conduction electrons;

e is the electron charge;

m* is the effective mass of electron.

As a rule, electrons within the conduction zone contribute to the conductive properties in materials with a pronounced zonal energy structure. For this reason, effective electron mass of relaxation processes [17] is introduced for them.

$$m^* = m_e \frac{n_0}{n_e}. \quad (10)$$

However, metals, as opposed to semiconductors, have no exclusion zone, thus we assumed that the electric conductivity is provided by all the valence electrons, and the effective electron mass is equal to the mass of electron $m^*=m_e$ ($m_e=9.11\cdot10^{-28}$ g). Then conduction electrons concentration would be determined by atomic density:

$$n_e = V \frac{\rho N_A}{\mu}, \quad (11)$$

where V is valency;

ρ is the density of the metal;

μ is the molar mass of the metal; and

N_A is the Avogadro constant.

The electron concentrations calculated using the formula (11) are shown in Table 2.

TABLE 2

Calculation of electron concentration in certain pure metals

Element	Cu	Al	Ni	Zr	V	Nb	Ta	Ti
μ, g/mol	63.546	26.981	58.693	91.224	50.941	92.906	180.947	47.867
Valency (V)	1	3	2	4	5	5	5	4
$\rho_{T=20^oC}\cdot10^3$, kg/mol	8.93	2.70	8.6-8.9	6.44	5.96	8,4 (15)	16.6	4,5 (18)
$n_e\cdot10^{23}$, cm^{-3}	0.84	1.8	1.7	1.7	3.5	2.7	2.7	2.264

The value of specific conductivity is determined using the specific resistivity ρ, which, in its turn, depends on the metal temperature and the pressure of the environment acting on the target:

$$\sigma = \frac{1}{\rho}, \quad (12)$$

$$\rho(T) = \rho_{T_0}\big(1 + a(T - T_e)\big)\big(1 + bP_{\text{Среды}}\big), \quad (13)$$

where $a = \frac{1}{\rho}\frac{d\rho}{dT}$ is the coefficient of temperature variation of specific conductivity; and

$b = \frac{1}{\rho}\frac{d\rho}{dP}$ is the coefficient of variation of specific conductivity under the action of hydrostatic compression.

The values of the coefficients *a* and *b* are shown in Table 3 [18].

TABLE 3

Values of specific conductivity temperature variation coefficients (a) and of specific conductivity variation coefficients under the action of hydrostatic compression (b) for certain pure metals

Element	**Cu**	**Al**	**Ni**	**Zr**	**V**	**Nb**	**Ta**	**Ti**
$a \cdot 10^{-3}$, 1/deg	4.33	4.67	6	4.0	2.8	2.28	3.6	5.5
$\rho_{To=273K} \cdot 10^{-6}$, Ohm·cm	1.55	2.50	6.14	40.5	18.2	23.3	12.4	42
$b \cdot 10^{-3}$, cm^2/kg	1.92	4.29	1.77	0.32	1.2	1.4	1.62	1.19

Plasma frequency is determined using the expression [16]:

$$\omega_p = \sqrt{\frac{4\pi n_e e^2}{m^*}}, \tag{14}$$

where e is the electron charge; $e=1.602 \cdot 10^{-19}$ C.

Values of plasma frequencies for the studied elements estimated using (14) are shown in Table 4.

TABLE 4

Estimated values of plasma frequencies in certain pure metals

Element	Cu	Al	Ni	Zr	V	Nb	Ta	Ti
ω_p, deg/s	$1.63 \cdot 10^{13}$	2.39	2.32	2.354	3.33	2.93	2.93	2.68

Correlations of laser radiation frequencies and plasma relaxation frequencies stated in Table 1 and Table 4 indicate that their ratios comply with the condition (1) ($\omega_p^2 > \Gamma^2$), which defines the dependency for absorption capacity of metals. The estimated values of absorption capacity are shown in Fig. 1 through 8.

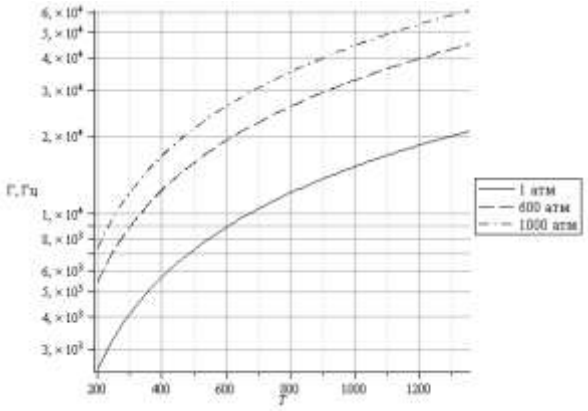

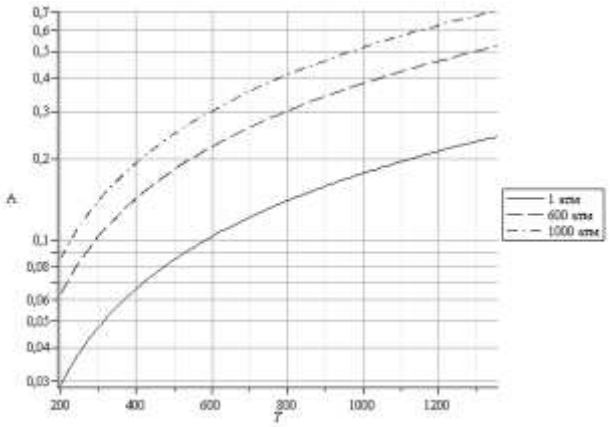

атм	atm

FIG. 1. Temperature dependence of G and A for Cu

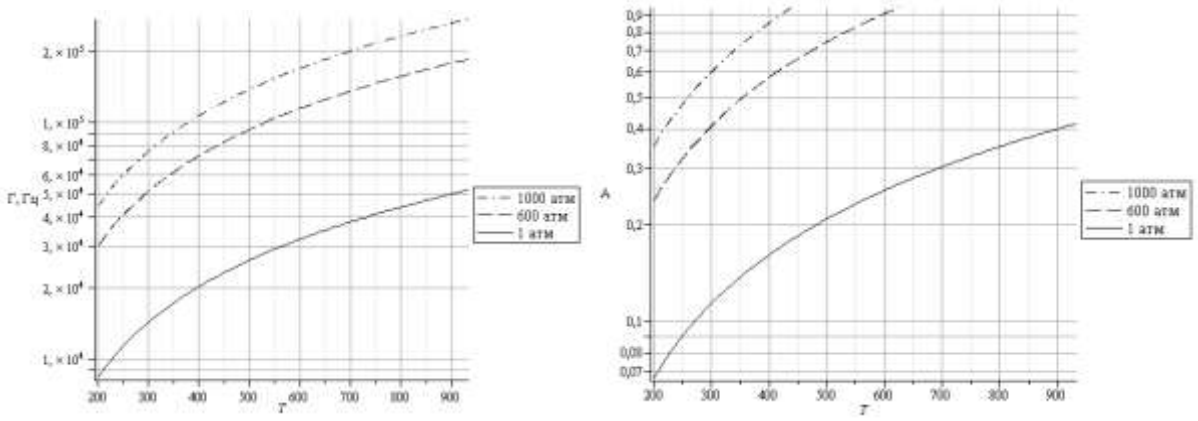

атм	atm

FIG. 2. Temperature dependence of G and A for Al

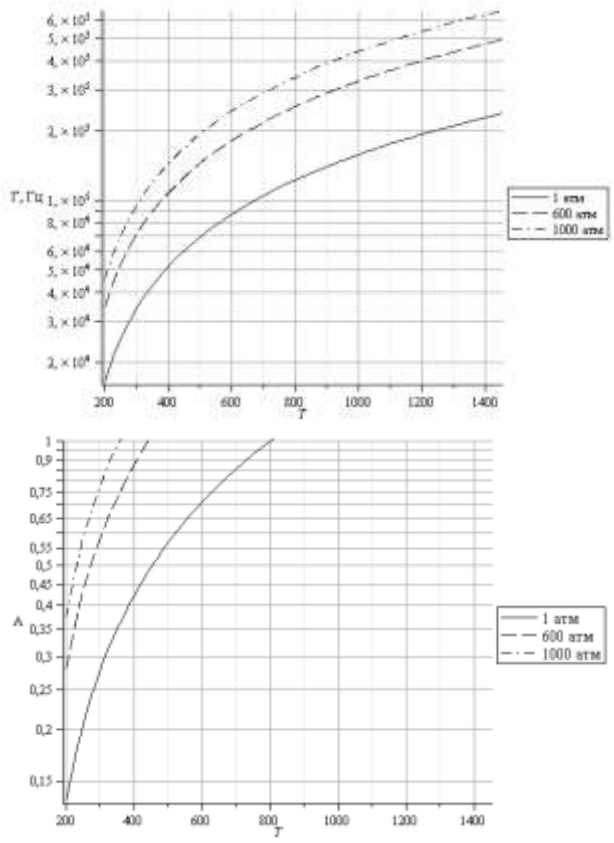

атм	atm

FIG. 3. Temperature dependence of G and A for Ni

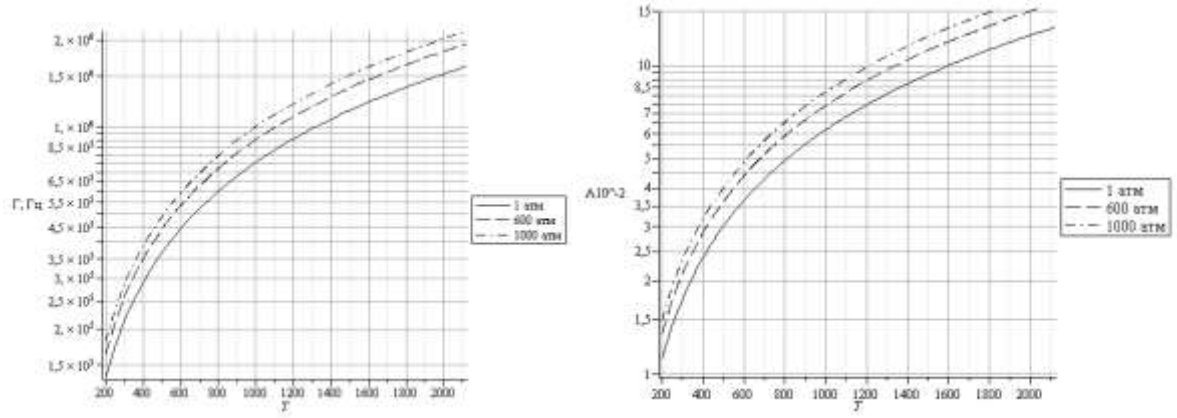

атм	atm

FIG. 4. Temperature dependence of G and A for Zr

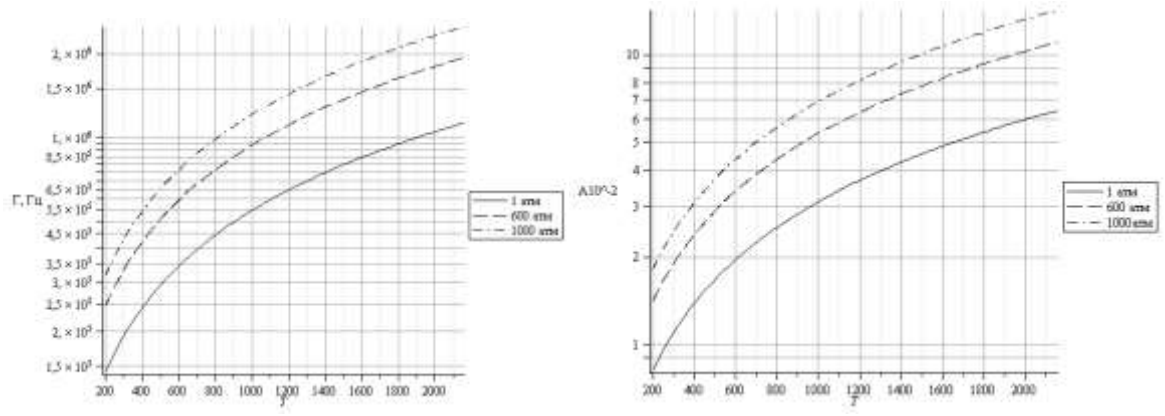

атм	atm

FIG. 5. Temperature dependence of G and A for V

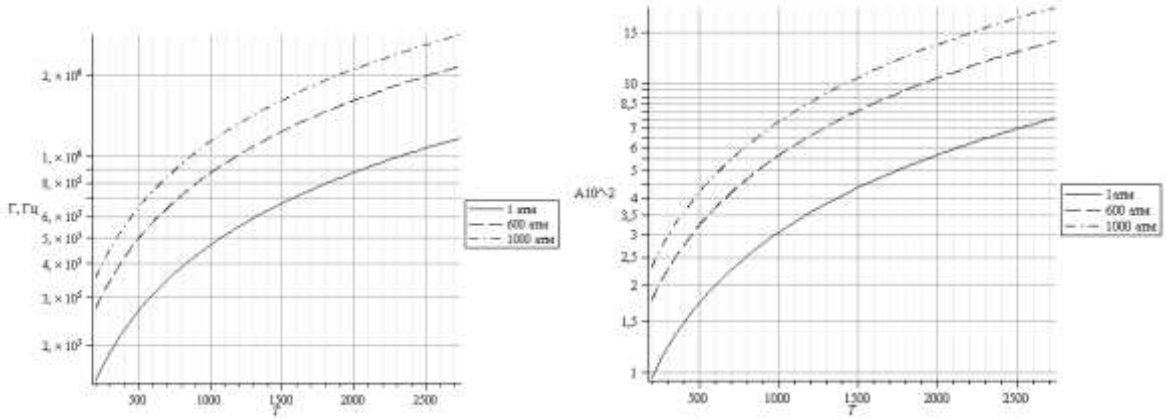

атм	atm

FIG. 6. Temperature dependence of G and A for Nb

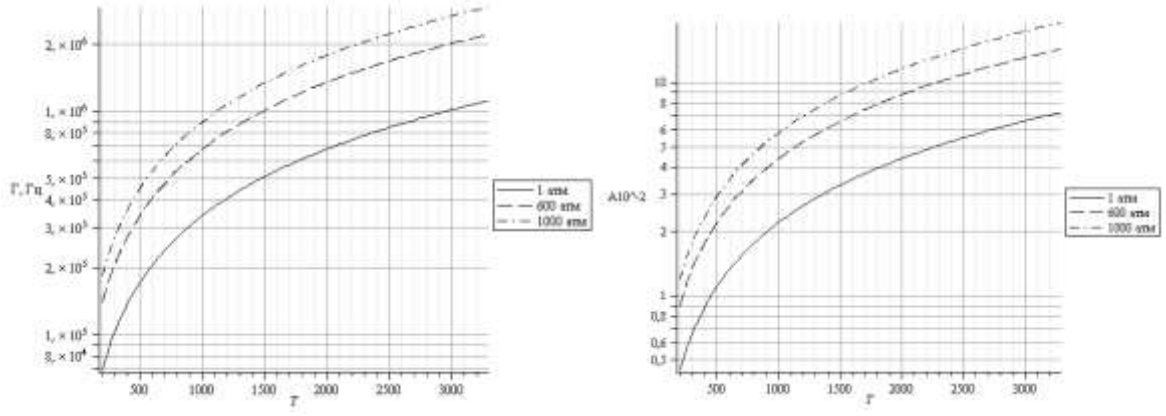

атм	atm

FIG. 7. Temperature dependence of G and A for Ta

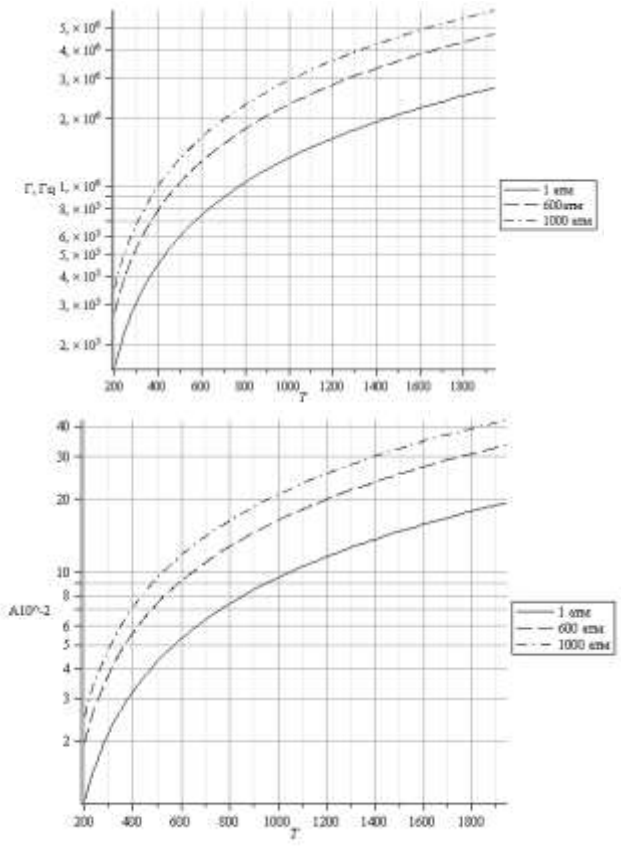

атм	atm

FIG. 8. Temperature dependence of G and A for Ti

Conclusion

The study evaluates the absorption capacity of metal targets depending on the temperature with various environment pressures based on the Drude formalism. The evaluation revealed that the absorption capacity of metals for model wavelengths of laser radiation increases by several times with the increase of hydrostatic pressure of the environment.

References

1. Kruusing A. Underwater and water-assisted laser processing: Part 1 - General features, steam cleaning and shock processing // Opt. LasersEng. 2004. T. 41. № 2. C. 307–327.

2. A. Kruusing. Underwater and water-assisted laser processing: Part 2 – Etching, cutting and rarely used methods / A. Kruusing // Optics and Lasers in Engineering. – 2004. – V. 41. – P. 329-352.

3. Y. Sano. Enhancement of Surface Properties of Metal Materials by Underwater Laser Processing / Y. Sano, N. Mukai, Y. Makino, M. Tamura et al. //The Review of Laser Engineering. – 2008. – V. 36. – P. 1195-1198.

4. R.K. Jain. Development of underwater laser cutting technique for steel and zircaloy for nuclear applications / R.K. Jain, D.K. Agrawal, S.C. Vishwakarma, A.K. Choubey et al. // Pramana: Journal of Physics. – 2010. – V. 75. – №. 6. – P. 1253-1258.

5. V. Senthilkumar. Laser cutting process – A Review / V. Senthilkumar // International Journal of Darshan Institute on Engineering Research & Emerging Technologies. – 2014. – V. 3. – №. 1. – P. 44-48.

6. P. Hilton. New developments in laser cutting for nuclear decommissioning / P. Hilton, A. Khan // Nuclear Waste Management Conference WM2014. Phoenix, USA, 2-6 Mar. – 2014. – P. 1-14.

7. M.V. Konyukhov. Determining the temperature profile of metal placed in an aqueous medium when subjected to heating by laser radiation / M.V. Konyukhov, K.A. Shcherbakov, E.S. Shitova, S.B. Sukhovey, A.A. Vorobiev, A.A. Pertsev // Problems of atomic research and industry: Material science and novel materials. – 2017. – vol. 3(90). – pp.46-54

8. S.A. Al-Mamun. Tuning the size of aluminum oxide nanoparticles synthesized by laser ablation in water using physical and chemical approaches / S.A. Al-Mamun, R. Nakajima, T. Ishigaki // Journal of Colloid and Interface Science. – 2013. – V. 392. – P. 172–182.

9. K. Siuzdak. Preparation of platinum modified titanium dioxide nanoparticles with the use of laser ablation in water / K. Siuzdak, M. Sawczak, M. Klein, G. Nowaczyk et al. // Physical Chemistry Chemical Physics. – 2014. – V. 16. – P. 15199-15206.

10. M. Vinod. Ag@Au core-shell nanoparticles synthesized by pulsed laser ablation in water: Effect of plasmon coupling and their SERS performance / M. Vinod, K.G. Gopchandran // Spectrochimica Acta Part A: Molecular and Biomolecular Spectroscopy. – 2015. – V. 149. – P. 913-919.

11. V. Tangwarodomnukun. Laser ablation of titanium alloy under a thin and flowing water layer / V. Tangwarodomnukun, P. Likhitangsuwat, O. Tevinpibanphan, C. Dumkum // International Journal of Machine Tools & Manufacture. – 2015. – V. 89. – P. 14-28.

12. K. Maximova. Size-controllable synthesis of bare gold nanoparticles by femtosecond laser fragmentation in water / K. Maximova, A. Aristov, M. Sentis, A.V. Kabashin // Nanotechnology. – 2015. – V. 26. – P. 65601-1-8.

13. M. Kanazawa, P. Koinkar, A. Furube. Enhancement in field emission of MoS2 nanosheets prepared in water using laser ablation method / M. Kanazawa, P. Koinkar, A. Furube // International Journal of Modern Physics B. – 2018. – V. 32. – P. 1-5.

14. L. Torrisi. Gold nanoparticles produced by laser ablation in water and in graphene oxide suspension / L. Torrisi, M. Cutroneo, L. Silipigni, F. Barreca et al. // Philosophical Magazine. – 2018. – V. 98. – №. 24. – P. 2205-2220.

15. A.V. Sokolov Optical properties of metals M.: Fizmatgiz, 1961, 465 p.

16. A.M. Prohorov, V.I. Konov, I. Ursu, I.N. Miheilesku Interaction of laser radiation with metals. Moscow. Nauka Publishing, 1988

17. P. Grosse. Mobile electrons in solid bodies. – M.: "MIR" 1982

18. I.K. Kikoin. Physical quantity tables / I.K. Kikoin. – M.: Atomizdat, 1976. – 1008 p.

UDC: 669·01716 [669.3+669.74

A STUDY OF THE STRUCTURE OF CU-0.5MN ALLOY MECHANICAL AND ELECTROPHYSICAL PROPERTIES

Yu. V. Karasyev, I.N. Gubkin, V.A. Drobyshev, M.V. Polikarpova, S.A. Shevyakova, A.V. Malchenkov, M.V. Kravtsova

SC «A.A. Bochvar High-Technology Research Institute of Inorganic Materials», Moscow

Comprehensive studies of the Cu-0.5Mn alloy were conducted. The alloy shows promise of use as a resistive matrix material in Nb-Ti superconductors intended for operation in variable magnetic fields. Metallographic and microroentgen spectral studies of specimens cut out from various parts of ingot were conducted. Mechanical properties of rolled specimens after annealing under temperatures of 350 to 500°C were studied, and comparative structural tests of the original copper and the Cu-0,5Mn alloy at temperatures of up to 700°C. This included theoretical assessment and experimental determination of specific electrical resistivity at room and cryogenic temperatures. It was shown that the electrical conductivity of the resistive alloy at the boiling point of liquid helium is lower by a factor of 100 than that of the original copper and thus the alloy may be used as a resistive matrix material.

Keywords: resistive alloy Cu-0.5Mn, microstructure, micro-homogeneity, instantaneous strength $\sigma_в$, conventional yield limit $\sigma_{0.2}$, specific electric resistivity, high-purity copper.

Introduction

Modern superconductors based on NbTi alloy are complex polyfilament composite wires that contain thin superconducting NbTi strands in metal matrix, each surrounded with a Nb barrier.

High-purity, highly electroconductive copper is usually used as the matrix, which, besides its process features, ensures stabilization of the superconductor during operation in magnetic system, especially in variable magnetic fields.

However, if the superconducting wire contains high-purity copper as the interfibre matrix, then electromagnetic pairing of threads can occur in a variable magnetic field due to the insinuation of supercurrents through the copper matrix.

To prevent this effect resulting in the increase of the thread effective diameter and a proportional increase of hysteresis losses, a certain distance between threads is ensured. The value of the interfibre distance depends on the electrical resistivity of the matrix material. For high-purity copper, minimum distances between threads should be at least 0.9 ÷1 um. If smaller interfibre distances are required, resistive Cu-Ni and Cu-Si alloys with the weight content of nickel of up to 30% and that of silicon of up to 2.5% are used. Additionally, application of Cu-Mn alloy is being discussed.

The use of a Cu-Mn matrix stems from its higher effectiveness in the prevention of electromagnetic coupling of threads, since besides the resistive dissipation which is characteristic of other resistive alloys, a Cu-Mn matrix also exhibits magnetic dissipation of superconducting electrons. The content of manganese in the copper at about 0.5% by weight ensures significant suppression of the “proximity effect” and makes it possible to place threads closer, up to the distance of ~ 0.17 um. [1]

Considering the above, the use of the resistive Cu-0,5Mn alloy as the interfibre matrix material should be considered in future development of new types of wires. The alloy is not currently produced industrially.

Before using this novel material in the production of superconducting wires, it must be studied, and the changes in physical and electrophysical properties of copper in the presence of manganese must be analyzed.

Materials and the procedure of the experiment

To produce an ingot of Cu-0.5Mn of 180 mm diameter and the height of 385 mm, semi-finished articles made of M0b grade copper (GOST 859-2001) and an additive alloy – 3.8% wt manganese. Smelting was carried out in a DR-1 model vacuum-induction furnace.

For the studies, templates approximately 50 mm thick were cut out at the top and the bottom parts of the ingot. Fig. 1 shows the diagram of cutting the ingot and templates.

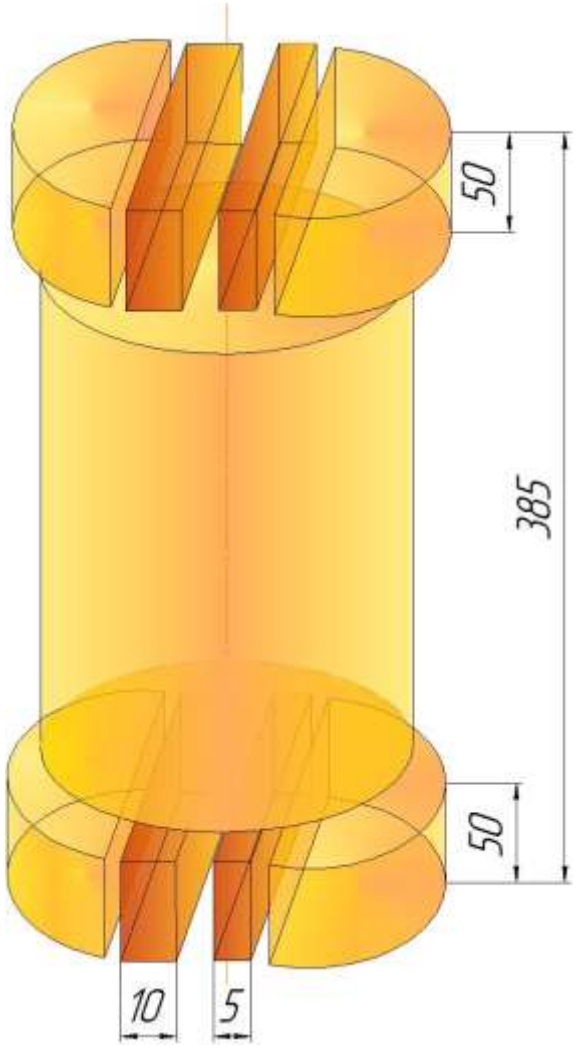

FIG. 1. Cu-0.5Mn ingot and template cutting diagram

Rectangular axial plates, 10 mm and 5 mm thick, were cut out from the central area of the templates. Cubical specimens of 10×10×10 mm were selected from the 10 mm thick plates. These were tested for the distribution of Mn within the alloy and used in metallographic studies and density determination using the hydrostatic method.

Manganese content was determined chemically using specimens of shavings taken from the top and bottom butt ends of the ingot.

Metallography studies of the ingot were carried out using an inverted-stage metallographic microscope OLYMPUS GX 51 and ColorView digital camera. AnalySIS FIVE software was used to process the images.

Using the microroentgen spectral analysis technique and the polished planes of the cubic specimens, the distribution of Mn in different locations of the ingot was studied (at the top and bottom of the ingot and at points located at different distances from the center: in the center and at the periphery of the ingot). Local microconcentration of Mn was determined in 40 locations spaced at 50 μm, at a 2 mm section selected at the center of the specimen.

Micro-homogeneity of Mn distribution within the alloy was measured using a Kamebax scanning electron microscope (SEM) equipped with a microroentgen spectral attachment.

To study physical properties, the 5 mm thick plates cut out of the ingot were rolled to the thickness of 0.5 mm. Flat specimens were cut out from the resulting plates for tensile tests. The form of the specimens is shown in Fig. 2, the dimensions of the working areas are given in Table 1. Other dimensions of the specimens comply with GOST 1497-84.

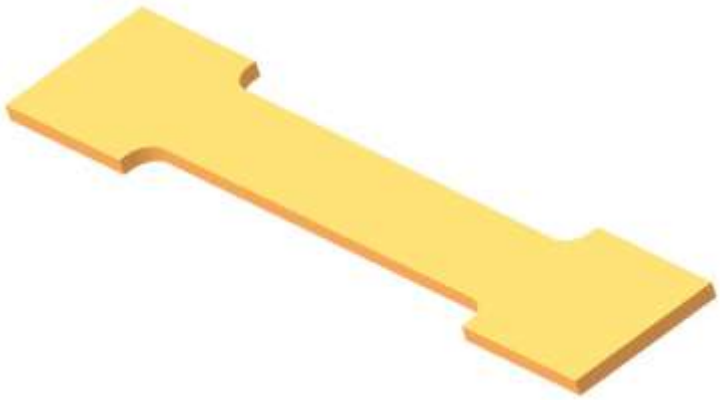

FIG. 2. Tensile test specimen

TABLE 1

Physical dimensions of specimen body used in tensile tests

Thickness, mm	Width, mm	Cross-section, mm^2	Initial effective length of the specimen, mm
0.5	6	3	10

Mechanical tensile tests were carried out at room temperature and within the temperature range of 500 to 700 °C, using the Instron 1185 testing machine which generated the tensile speed of 1 mm/min. At room temperature, the tests were conducted on cold-worked specimens and specimens annealed at temperatures of 350 to 500 °C for 1 hour. High-temperature tests were carried out at specimens annealed at the temperature of 500 °C for one hour.

Witness specimens were subjected to annealing along with physical test specimens. This was followed by a study of witness specimen crystalline structure using metallography techniques.

Specific electrical resistivity of the produced manganese alloy was both assessed theoretically and determined experimentally.

Theoretical assessment of specific electrical resistivity was carried out with consideration of Mattiessen's rule and the Nordheim’s law. Experimental specific electric resistivity of the alloy was determined on wire specimens with the diameter of 0.5 mm. The specimens were manufactured by drawing rectangular (2×2 mm) bars cut out after rolling the 10 mm thick plates. The wire specimens having the length of 70 to 80 mm were annealed in vacuum at the temperature of 500°C for 1 hour.

Study results

The analysis of the conducted studies revealed that the content of Mn in the ingot (in both its top and bottom parts) was 0.48% wt.

The density of the smelted Cu-0.5Mn alloy is 8.91 g/mm^2. As a comparison, the density of oxygen-free copper at 20 °C in the recrystallized state lies within the range of 8.45 to 8.90 g/mm^2. Density of copper in the strained condition varies from 8.7 to 8.94 g/mm^2.[2]

Fragments of the macrostructure of templates from the top and bottom part of the ingot (from its longitudinal axis) are shown in Fig. 3. As we can see, the ingot has a typical macrostructure: equiaxial grains at the center and at the periphery of the ingot, and elongated grains within a half-radius area. No defects, such as large pores, cracks, impurities etc., were revealed at the surfaces of the macro-sections.

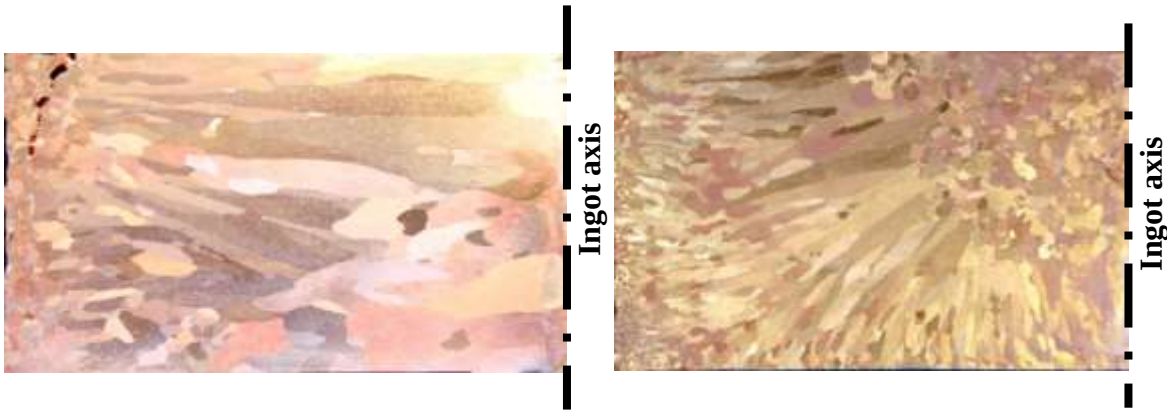

Ось слитка	Ingot axis

FIG. 3. Macrostructure of the Cu-0.5Mn alloy ingot along the longitudinal cross section ×1.5: a - top of the ingot, b - bottom of the ingot

Mn microconcentration profiles within the ingot are shown in Fig. 4. Studies revealed that, at the periphery, both at the top and bottom of the ingot, the distribution of manganese is uniform with some minor deviations of Mn concentration values from the medium value, unlike in the central part. This variance of microconcentration evidences a more pronounced segregation process occurring during the consolidation at the central part than at the periphery.

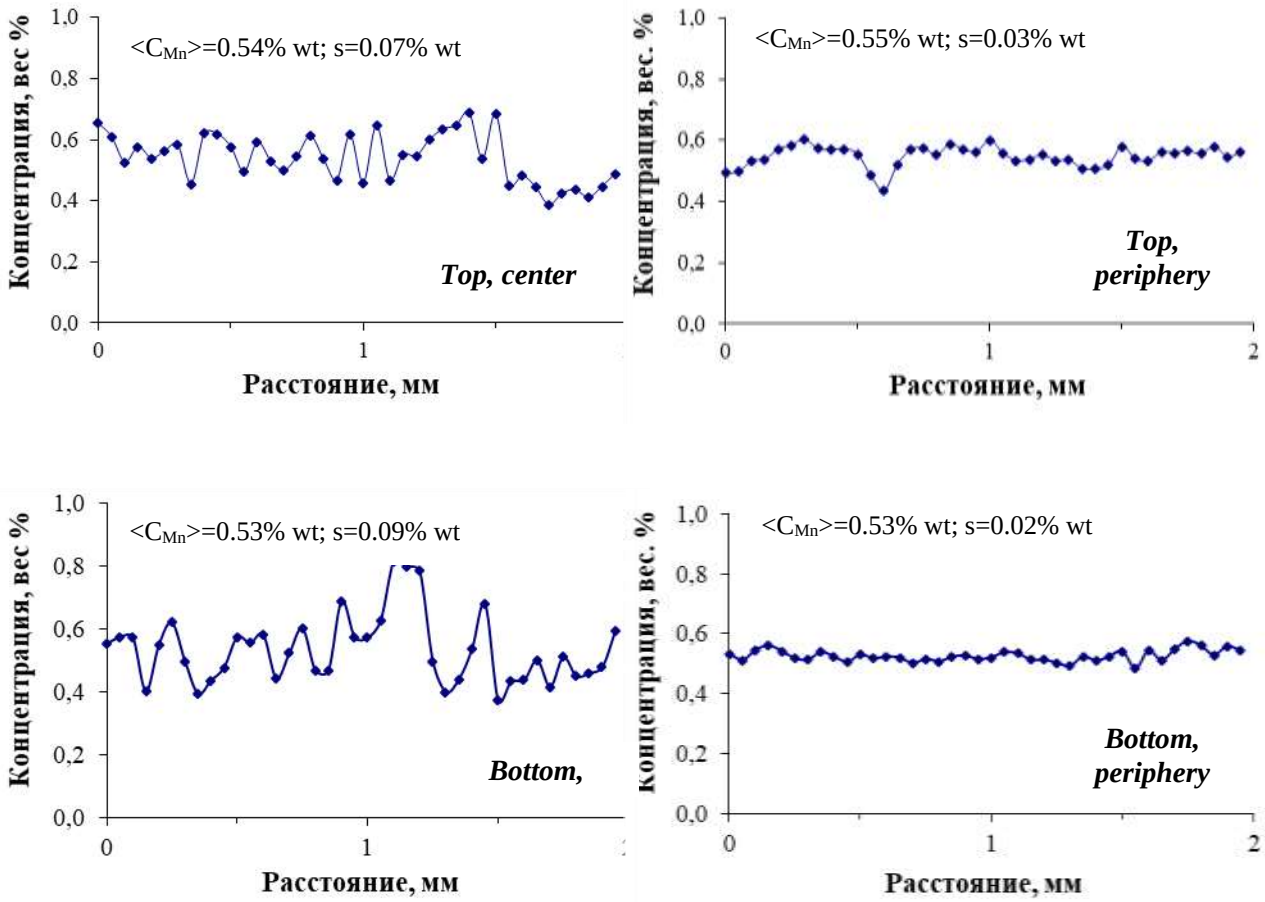

Концентрация, вес%	Concentration, % wt
Расстояние, мм	Distance, mm
Верх, центр	Top, center
Верх, периферия	Top, periphery
Низ, центр	Bottom, center
Низ, периферия	Bottom, periphery

FIG. 4. Mn microconcentration profiles at the top and bottom of the ingot.

The dependency of variation of instantaneous strength (σ_i) and the structure of the Cu-0.5Mn alloy on the annealing temperature is shown in Fig. 5 and 6.

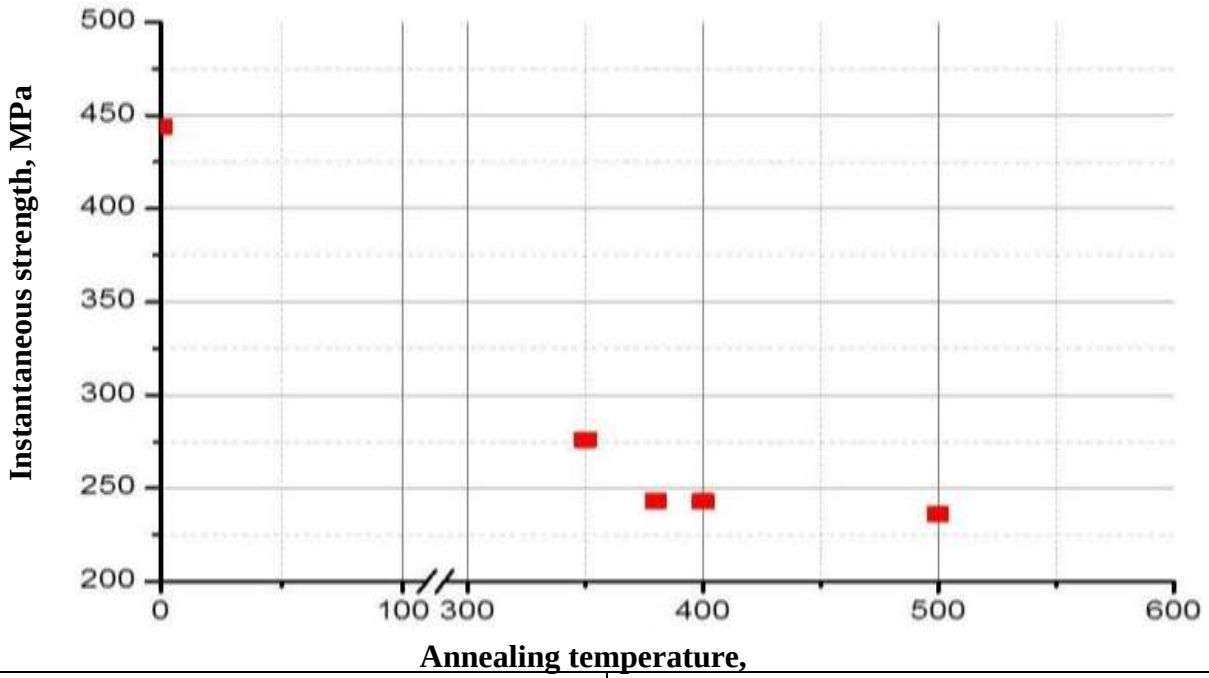

Временное сопротивление, Мпа	Instantaneous strength, MPa
Температура отжига, С	Annealing temperature, C

FIG. 5. Instantaneous strength of Cu-0.5Mn alloy specimens depending on the annealing temperature (holding time -- 1 hour)

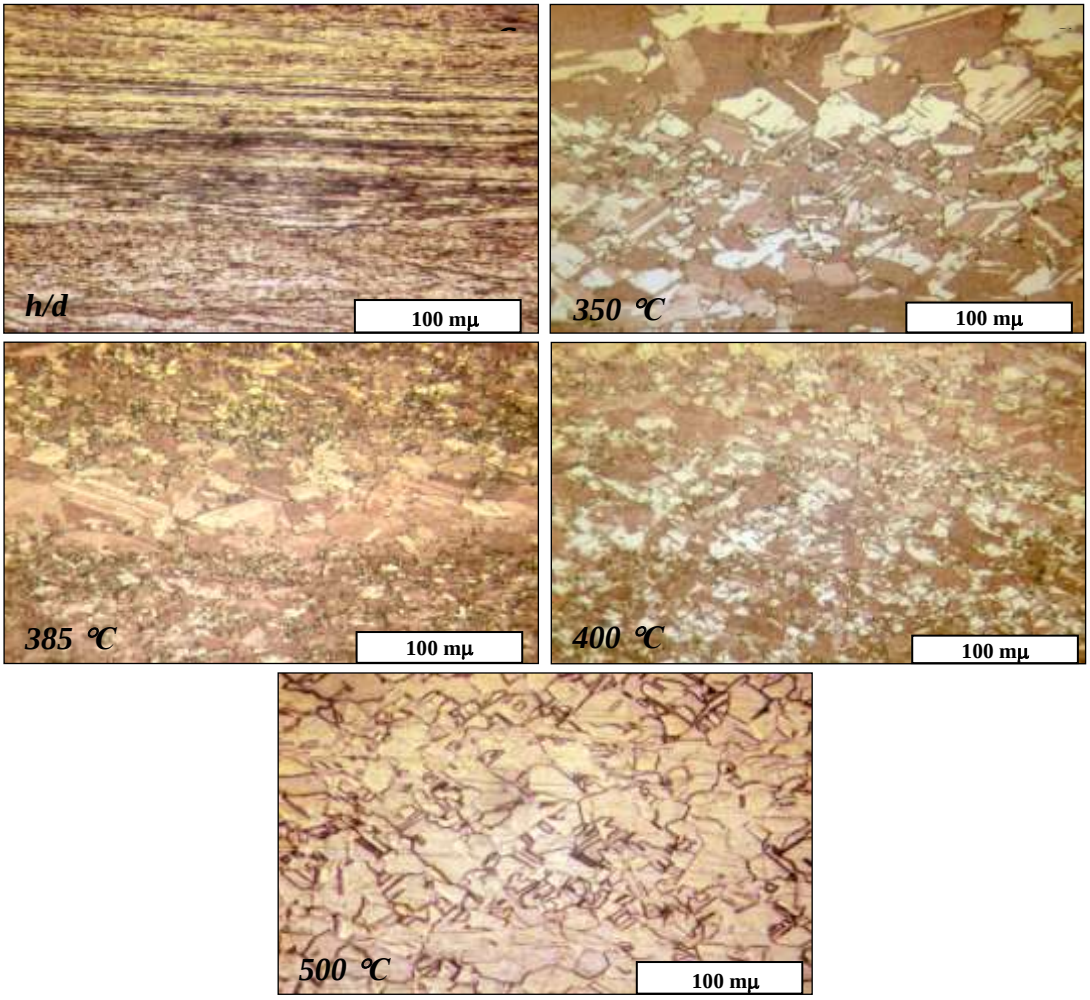

FIG. 6. Evolution of microstructure of the Cu-0.5Mn alloy following the annealing procedures.

The cold-worked structure of the alloy is fibrous with an indistinct division of the fractured and the crystals stretched along the direction of working: the value of instantaneous strength (σ_i) of the alloy at room temperature is 444 MPa. At the annealing temperature of 350 °C (1-hour annealing), elongated worked grains vanish and new grains are formed, while the instantaneous strength lowers to 275 MPa, that is, more than by a factor of 1.6. Besides that, the cold-worked fibrous structure is replaced with the structure characteristic to incomplete recrystallization. At the temperature of 385 °C, an area of variously directed faceted grains evolves, and fine equiaxial grains gradually form at the periphery of the specimen. Increasing the temperature to 400 °C results in the development of the recrystallization process, i.e., the majority of the space is occupied by fine faceted grains. Here, instantaneous strength decreases somewhat, down to 240 MPa. Following annealing at 500 °C, near-complete recrystallization of the alloy occurs: a polyhedral structure is observed both at the center and at the periphery, and instantaneous strength reaches 235 MPa. It should be noted that multiple annealing twins form within the alloy within the studied temperature range of 350 to 500°C.

As compared to the high-purity oxygen-free copper in the hardened (437 Mpa) and annealed (225 MPa) state [2], the addition of 0.5% wt of manganese improves the

instantaneous strength of the copper-manganese alloy insignificantly both in the cold-worked (444 MPa) and the annealed at 500°C (235 MPa) state.

The dependency of structural characteristics of the resistive Cu-0.5Mn alloy and oxygen-free copper on the test temperature is shown in Fig. 7.

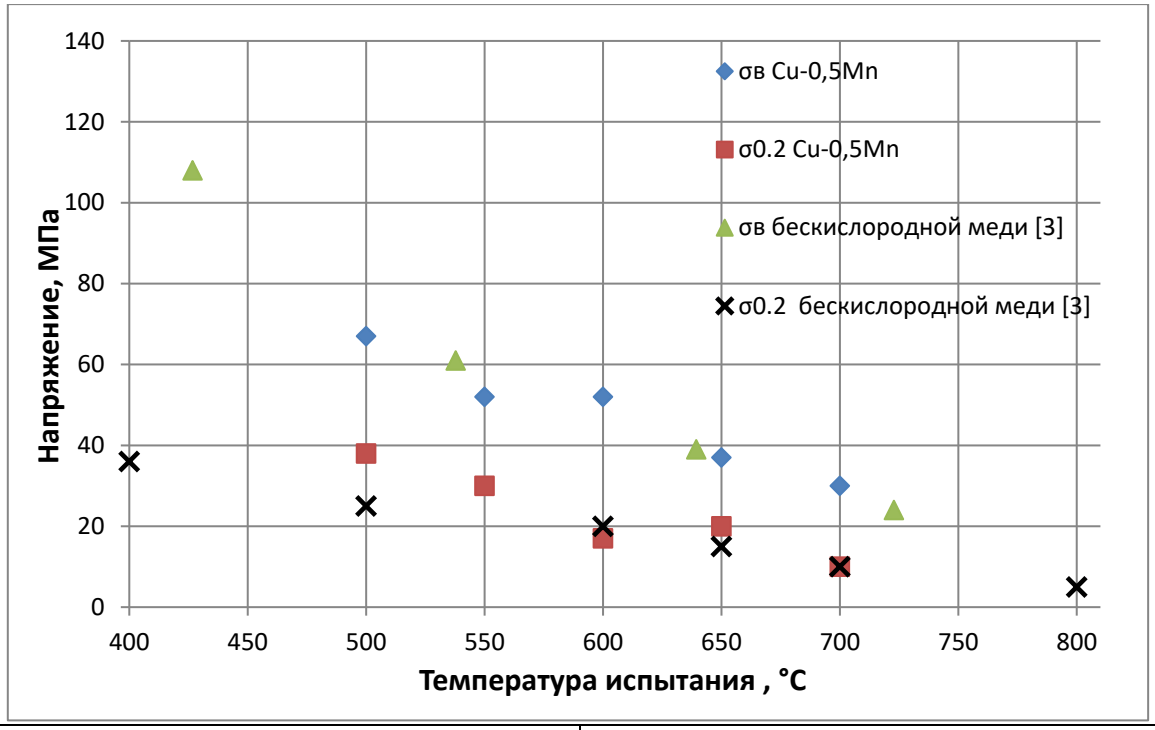

Напряжение, Мпа	Stress, MPa
Температура испытания, С	Test temperature, C
бескислородная медь	Oxygen-free copper

FIG. 7. The dependency of structural characteristics of the resistive Cu-0.5Mn alloy and oxygen-free copper on the test temperature

Figure 7 demonstrates that the instantaneous strength and the yield limit of copper and Cu-0.5Mn alloy are practically identical within the temperature range of 550 to 650°C.

Thus, mechanical properties of Cu-0.5Mn alloy are practically identical to those of oxygen-free copper, and its application in the production of superconducting composite wire would not result in any alteration of the manufacturing process of the composites.

In accordance with the Mattiessen's rule, specific resistivity of metals can be expressed in the following form:

$$\rho = \rho_{id}(t) + \rho_{re} \qquad (1),$$

where $\rho_{id}(t)$ is the ideal resistivity which depends on the temperature (for copper, at t = 20°C the value is 1.68 uOhm×cm [4]);

ρ_{re} is the residual resistivity which is determined by conduction electron scattering at crystal defects.

M0b grade copper (GOST 859-2001) which was adopted as the base in the smelting of the alloy has the specific resistivity of 0.01706 uOhm×m at the temperature of 20°C (according to [5]). Thus, ρ_{re} of the original copper stays at a level of NLT 0.026 uOhm×cm.

In accordance with the Nordheim's law, the change of ρ_{re} for solid-state solutions depends on the composition, and follows well the following parabolic dependency:

$$\rho_{re} = C\, X_a\, X_в = C\, X_в\, (1 - X_в) \qquad (2),$$

where C is the constant which depends on the nature of the alloy and X_a and $X_в$ are atomic fractions of the alloy components.

By representing the ascending branch of the parabola in the form of a line, as in the case of diluted solutions, we obtain, with a satisfactory accuracy:

$$\rho_{re} \approx C\, X_в \qquad (3),$$

where the constant C describes the variation of the residual resistivity $\Delta\rho_{re}$ per 1 at. fraction of the alloying component, in our case, manganese.

Considering that the value of the factor C for Mn is 2.9 *uOhm×cm/at %*[6], and the concentration of Mn is 0.48% wt, or 0.56 at %, the increment of the residual resistivity related to the introduction of the given quantity of Mn in the solid-state solution would amount to *1.624 uOhm×cm*. This value roughly corresponds to the specific resistivity of alloy specimens at 4.2 K ($\rho_{re} = \rho_{4.2\ K}$), and results in an increase of specific resistivity at room temperature by the same amount, as per formula (1), i.e.,

$$\rho_{20\,^oC} = \rho_{id}(t) + \rho_{re} = 1.68 + 0.026 + 1.624 = 3.33\ uOhm \times cm.$$

The measured and estimated values of the specific electrical resistivity of the resistive alloy Cu-0.5Mn at the temperature of 4.2 K are shown in Table 2.

TABLE 2

Specific electrical resistivity of Cu-0.5Mn alloy

Temperature	Specific resistivity ρ (uOhm×cm)	
	Experiment following vacuum annealing at 500 °C during 1 hour	Estimated value
293 K	3.42	3.33
4.2 K	1.70	1.65

Table 2 reveals that the measured values of the specific resistivity exceed the estimated values approximately by 3 %. The ratio of specific eclectic resistivity values ($\rho_{293}/\rho_{4.2}$) at temperatures of 293 K and 4.2 K is 2.01. This is by two orders less than the typical value ($\rho_{293}/\rho_{4.2}$) for the original copper, which is about 200 units.

Conclusion

The results of the studies demonstrate that:

- the density of the smelted Cu-0.5Mn alloy is 8.91 g/mm^3.
- The resulting Cu-0.5 Mn alloy has a highly-homogeneous distribution of manganese with low deviations of local values of Mn concentration from the average value at the ingot periphery, as opposed to its center;
- Following annealing at 500°C, the Cu-0.5Mn alloy undergoes a virtually complete recrystallization resulting in the formation of a polyhedral structure which features multiple annealing twins;
- Introduction of 0.5% wt of manganese into the copper matrix results in an insignificant increase of instantaneous strength both in the cold-worked and the annealed (at 500°C) state.
- The instantaneous strength and the yield limit of the copper and Cu-0.5 Mn alloy specimens determined during tests within the temperature range of 550 to 650°C were virtually identical.
- Specific electrical resistivity of the resistive Cu-0.5Mn alloy at the temperature of 293 K and at the temperature of 4.2 K is 3.42 uOhm×cm and 1.70 uOhm×cm, respectively. The specific resistivity of the alloy at cryogenic temperature is higher than that of the original copper by approximately two orders.

Thus, structural state and mechanical and physical properties of the resulting Cu-0.5Mn alloy comply with the requirements to the interfibre matrix material of the composite superconducting wire.

References

1. I.N. Gubkin et al., Conductors intended for operation in an alternating current. Problems of atomic research and industry. Coll., Issue 1 (53), 1996, p. 32

2. L.S. Vatrushin et al. "Oxygen-free copper", Metallurgy, Moscow, 1982.

3. P.I. Polukhin et al., Plastic resistance of metals and alloys, Reference book, p. 361, 1976.

4. M.P. Malkov et al. Physical and engineering basics of cryogenics reference M.: Energoatomizdat, 1985. – 432 p.

5. B.S. Tikhonov, Heavy nonferrous metals: Reference book. M.: Tsvetmetinformatsiya, 1999. - 416 p.

6. J.O. Linde «An Experimental study of the resistivity-concentration dependence of alloys» - Helv.Phys. Acta, 1968, v.41, p.1007-1015.

UDC: 621.039.7 : 66.074

PURIFICATION OF WASTE GASES FROM NITROGEN OXIDES IN RADIOACTIVE WASTE CALCINATION AND VITRIFICATION PROCESSES

O.A. Ustinov, S.A. Yakunin
SC "A.A. Bochvar High-Technology Research Institute of Inorganic Materials", Moscow

An overview of research and engineering information concerning systems of flue gas cleaning of radioactive waste calcination and vitrification installations was performed aimed at retrospective assessment of the problem of flue gas cleaning in processes of calcination and vitrification and the selection of the optimal scheme for the same providing effective removal of NO_x. The information was researched in 27 publications in 8 countries over the period starting in 1978 to the present day. The information on NO_x scrubbing (involving other gas treatment units) was reviewed in the following order: absorption, selective catalytic reduction (SCR) (in certain cases, in combination with selective non-catalytic reduction (SNCR) and hydrocarbon combustion.

Of the 12 gas cleaning systems including absorption-based removal one system was developed in France, in the United Kingdom and China, 2 systems -- in Germany (one of such operates in Belgium), 3 -- in Russia and 4 -- in the USA.--- Of the 10 gas cleaning systems that use SCR, 8 are employed in the USA and one in each Russia and South Korea. Non-selective ammonia reduction is used in one system developed in the USA, in combination with SCR units. Eight gas cleaning systems that use high-temperature hydrocarbon combustion were developed in the USA and one system -- in South Korea.-

The comparison of the above methods of nitrogen oxide scrubbing in flue gases resulted in the conclusion that the gas cleaning techniques used in calcination and vitrification processes are complex and costly, but necessary. Preference was given to high-temperature reduction processes due to lower quantities of liquid radioactive waste produced. Use of various methods of nitrogen oxide removal is defined by the specific vitrification process and the properties of the gases formed during the process.

Keywords: radioactive waste, calcination, vitrification, flue gases, gas cleaning, nitrogen oxides, absorption, selective catalytic reduction, non-selective catalytic reduction, hydrocarbon combustion.

Introduction

Gases resulting from calcination and vitrification of radioactive wastes usually contain nitrogen oxides (NO_x) in concentrations many times higher than the permitted allowable limits of atmospheric emissions. For this reason, gas cleaning is one of essential issues in the implementation of these processes. The research and engineering information presented below was overviewed in order to perform a retrospective assessment of the problem and select the optimal arrangement of gas cleaning by way of calcination and vitrification to ensure effective removal of NOx_x. A number of surveys had been previously published on the topic.

In 1988, a report of Technical Committee of IAEA was published dedicated to issues of design and operation of flue gas cleaning systems at highly radioactive waste reclamation installations [1]. The report reviewed various types and designs of gas cleaning installations. It was noted that the main types of nitrogen oxide removal installation are usually absorbers, both packed and bubble-type. Flue gas cleaning systems of seven vitrification and calcination installations used in 6 countries were described in adequate details. Notably, special devices intended for nitrogen oxide scrubbing were mentioned in descriptions of only three of installations.

In 1992, US Environmental Protection Agency published a reference book on vitrification technologies [2] which contained some insignificant information on flue gas cleaning systems in High Radioactive Waste (HRW) vitrification, which indicated that a typical sour gas scrubbing unit contained two sequentially arranged spray scrubbers. The reference book has no detailed information on the cleaning of flue gases in HRW vitrification installations.

In 1996, a report was published in the USA on the selection of a flue gas cleaning system for Low Radioactive Waste (LRW) vitrification installations [3]. The report proposes selection criteria and reviews five different systems with regard to initial gas composition and depending on the type of main vitrification device -- the melter. SCR, staged hydrocarbon combustion and SNCR units were stated as the most essential means of scrubbing nitrogen oxides from gas flows. Devices and purposes of the used instruments were described and the costs required to install a specific unit were stated.

In 2001, a report was published in the USA describing simulation of three options of nitrogen oxide scrubbing from vitrification of sodic wastes: staged combustion, SNCR and high-temperature (up to 2850^{o}C) decomposition of NO_x [4]. The information contained in the report is of some interest, but is not corroborated by practical evidence.

In 2014, IAEA published a report (effectively, a reference book) on the treatment of gaseous radioactive waste [5] which contained an addendum on a compact disk [6]. This contained description of nine RAW vitrification installation gas cleaning systems used in five countries, as well as designs and operating principles of the used systems. Only 7 designs mention nitrogen oxide scrubbing devices.

The materials of the reviews mentioned above were used in the preparation of this overview and were considerably supplemented with information from other sources.

The information on NO_x scrubbing (involving other gas treatment units) was reviewed in the following order: absorption, selective catalytic reduction (SCR) (in certain cases, in combination with selective non-catalytic reduction (SNCR) and hydrocarbon combustion. Other units of gas cleaning systems (wet dust control systems, condensation, filtration, removal of sour gases with dry reagents) may, to a degree, facilitate scrubbing of NO_x from flue gases but are not specifically reviewed in terms of solving the problem.

1. Absorption

1.1. In France (Marcoule) the calcination and vitrification installation AVM has been operating since 1978. Its performance in terms of initial solution is 60 dm^3/h. The flue gas cleaning system includes a reflux scrubber, a condenser, two sequentially arranged water-sprinkled absorbers and a HEPA filter. Nitrogen oxide capture efficiency is 96 to 98 % [7]**.** The absorbing liquid is returned from the first scrubber to the calcination unit. The treated gas is mixed with ventilation air and passes an additional filter before discharge.

1.2. In 1980, data on tests of a spray-type calcination unit and a melter for radioactive waste vitrification conducted in the USA by PNL were published. Non-radioactive solutions were tested at the initial stage. The gas cleaning system comprised a filter made of sintered stainless steel particles, a Venturi scrubber sprinkled with a weak (0.1 M) nitric acid, a shell and tube condenser, a packed alkaline scrubber with a demister and a HEPA filter. Non-condensable gas consumption was 6.7 dm^3/s.

1.3. Subsequent tests were conducted on actual HRW. These tests are covered in more details in reports [9, 10]. It should be noted that the authors did not consider cleaning the flue gases from non-radioactive components. The gas cleaning systems used in real-life HRW included porous metal filters, a sprinkled cooler filled with pall rings made of stainless steel, an evaporator designed to increase concentration of HRW, ensure concentration of condensate during calcination and cleaning of flue gases from aerosols, a condenser, a reflux tower, a packed absorber featuring absorber solution recirculation and porous metal filter and HEPA filters. Following the final filtration, flue gas was discharged into the ventilation system of the facility where it was mixed with ventilation air down to 47 m^3/s. Before dilution, the volume fraction of NO_x in the exhaust gas was 0.5 % (NO – 0.3 %, NO_2 – 0.2 % [8]), thus, the permissible atmospheric discharge level was primarily achieved due to dilution with air (NO – 3 ppm, NO_x – 5 ppm) [10].

1.4. According to information published in 1980 concerning preliminary simulation tests of a HRW vitrification plant in the Nuclear Research Center of Karlsruhe, Germany [11], flue gases exiting the melter that had the temperature of 180-250°C successively passed the SS (with the NO_x decontamination factor of 2-8) (in order to prevent steam condensation, temperature of 85-90°C was maintained in the SS), the 1st adsorber which provided entrapment of ruthenium, the condenser (with the NOx_x decontamination factor of 2), two packed absorbers providing NO_x removal (with the NO_x decontamination factor of 5-10), the 2nd adsorber for ruthenium removal and a HEPA filter. The final NO_x decontamination factor was 75 which corresponds to 99% effectiveness. The SS removed 120 g/h of dust with the melter operating at the capacity of 30 dm^3/h. Particle removal effectiveness was 90-95 %. A

considerable number of liquid aerosols produced by the SS were removed by a demister located in its upper part. The test demonstrated that the scrubber removes not only dust particles, but also a significant part of volatile ruthenium compounds.

1.5. According to information published in 1982, 1988 and 1992 [1, 12], an installation for the removal of nitrogen oxides which operated in Belgium included a bubble-type tray absorber sprinkled with 5 M of nitric acid with an addition of hydrogen peroxide. The volume fraction of NO_x at the melter exit was 4%. Large solid particles were removed by a reflux in the wet scrubber located within the melter, at the flue gas discharge. The first chamber of the gas cleaning system contained a tubular condenser, a jet scrubber and the above-mentioned absorber. Final cleaning of the gas was performed by the second chamber of the gas cleaning system equipped with a HEME demister and two successive HEPA filters. The flue gas was heated above the dew point before entering the HEPA filters. After leaving the filters, the gas flow was cooled down to 30ºC, and remaining moisture was extracted by a separator.

1.6. Starting 1989-1991, a bubble plate absorber was used as the main unit of the gas cleaning system in the active vitrification lines in the UK (the Sellafield facility). A SS condenser was also used [13].- In 2002, the second line was launched and in 2004 - the advanced third line [14] featuring a gas cleaning system which included a SS, a condenser, a NO_x absorber (removal using water of nitric acid), as well as electrostatic precipitators and HEPA filters. The design was based on the AVM installation (France).

1.7. A report dated 1992 on the vitrification installation used in West Valley City (WVDP) mentions SS, HEME, HEPA and the NO_x removal system itself (comprising a packed absorber and a bubble absorber), a heater, strainer filters, HEPA filters and a SCR unit [15].

1.8. In 1992, some information on tests conducted in Russia of the EP-100 pilot vitrification installation was published. The installation used an absorption column to capture nitrogen oxides as part of its gas cleaning system, a strainer and fine particle filters and an absorber for removal of ruthenium tetroxide [16].

1.9. According to information published in 1992 [17], China developed a vitrification installation project with a gas cleaning system which comprised an FC, a wet SS, a condenser, a jet scrubber, a NO_x absorber, a fibrous glass strainer filter and two HEPA filters.

1.10. Russian Mayak Enterprise developed and has operated since 1987 the EP-500 vitrification installation with a NO_x absorber as part of its gas cleaning system [6] (published in 2007). The gas cleaning system also includes a condenser, a strainer and fine particle filters and a pyrolusite column for the removal of ruthenium tetroxide.

1.11. In 1999, Russia-based Radon Enterprise operated an installation for the vitrification of Liquid Radioactive Waste (LRW) produced by treatment of WWER and RBMK type reactors. The installation used an absorber which, along with other gas cleaning system units (a cool air dissolution unit, a sock filter, HEPA filters and an SCR plant), provided the NO_x separation factor of 7000 and the reduction of NO_x concentration in processed gases of down to 10 mg/m^3 [6].

1.12. In 2005, information on the DBVS project was published in the USA, - vitrification within the container intended for subsequent disposal. The gas cleaning system

included a high-temperature porous metal filter, a water absorber, an alkaline absorber, an SCR installation and a SS[18].

2. Selective catalytic reduction (SCR)

The report of Pacific Northwest National Laboratory (PNNL), USA [3], covers only five alternative gas cleaning systems for the vitrification of low-activity waste (LAW). Three of these (the 1st, 3rd and 4th) involved SCR as the main unit of NO_x scrubbing. Depending on the type of the main vitrification station (melter), gas flow speed of 6.6 or 2.1 m^3/s was adopted, with initial NO_x volume fraction of 1.6 or 5.0%, respectively.

2.1. The first system comprised FC, SS and HEME before the SCR unit. Gas discharged from HEME was heated in an exchanger up to ~ 290-370°C as required for the reducing reactions with ammonia in the SCR unit. Absorption of nitrogen dioxide in the SS caused certain reduction of NO_x concentration at the SCR system intake. Velocities of ammonia introduction into the SCR were controlled by continuous monitoring of NO_x levels in the exhaust pipe. Following the SCR, the gas was cooled down to ~ 70-120°C and passed through a number of filters to ensure complete removal of radionuclide particles. A strainer was installed before each of the HEPA filters to extend their operating life. The expected NO_x removal efficiency should be no less than 90-99 %, depending on the number of SCR devices in the line. Considering the effectiveness of one SCR unit to be equal to 90%, at least three units are needed to ensure the required reduction of NO_x emissions. Due to the absence of residual ammonia absorption, there is a risk of high levels of emissions of the latter.

2.2. In the third system, the exhaust gas flow is directed from the melter to the SNCR unit for the reduction of 30-50 % of nitrogen oxides into molecular nitrogen using ammonia. For the reduction reaction to proceed, the temperature of ~ 870-1090°C is needed (if temperature is below ~ 870°C, the majority of ammonia fails to react and must be captured at later stages. Heated above ~ 1090°C, ammonia oxidizes and forms an additional amount of NO_x). After the treatment, the gas passes to SS where its temperature is reduced down to ~ 290-370°C. This is the normal temperature range for the following SCR unit. After leaving the SCR unit, the gas is transported to sour gas absorber sprinkled with a sodic alkaline solution. After the absorber, the gas flow is directed towards the demister, the HEME, the metal filter and the HEPA filter. Nitrogen oxide removal efficiency is approximately 99.3% (30% in SNCR and 99% in the two SCR units).

2.3. The fourth system is similar to the third one except that the first device intended for solid particles is a scrubber instead of a metal filter. This system is less suitable for the melter which generates a relatively large flow of aerosols since the SCR unit is vulnerable to high aerosol concentrations. The initial reduction of nitrogen oxides occurs in the combustion chamber located over the melter. Then the refrigerator evaporator reduces temperature to ~ 290-370°C, and two SCR units are located after it. The aggregate efficiency of nitrogen oxide removal in the 4th system is ~ 99.4%. The gas discharged from the SCR unit is cooled either in the refrigerator evaporator or by a pre-saturator installed before the wet scrubber. Temperature of the gas at the scrubber input shall be no lower than ~ 120°C.

2.4. In 1997, the HRW vitrification plant operating in West Valley City, USA, was described. The plant had flue gas processing capacity of 0.708 m^3/s. It included a SS followed by HEME and HEPA, as well as a SCR unit where catalytic reduction of NO_x with ammonia is performed at 320°C in two layers (Raschig rings and granules). [19]. It was noted that nitrogen oxide NO_x concentration at the discharge was compliant with permissible levels. The plants performance was about 30 kg/h of glass. The installation was decommissioned in 2002 after it had processed 24 MC of HRW to 275 glass canisters of ~ 2 tons each [18]. No information on whether NO_x was removed in units of the system upstream of the SCR was published.

2.5. In 2001, in the Idaho National Laboratory, USA, a research was performed on the simulation of the vitrification process of sodic waste [20]. The research studied three options of the gas cleaning system suitable for the Hanford, Savannah River and West Valley. The West Valley process flow included the following units: an FC, a packed sprinkled cooler, a Venturi scrubber, a knockout drum, a demister, a HEPA filter, adsorbers for mercury removal, HEME, a pre-filter, a trap, two HEPFA filters, an adsorber with granular activated carbon for mercury and organic compound removal, SCR units operating at 400-450ºC (two units operating in parallel), an HMW unit for repeated supplementary combustion of the organic component, a cooler.

2.6. In 2000, the project of LAW vitrification melter gas cleaning (> 1.25 t/h of glass) containing organic components was published as part of the Hanford River Protection Project (RPP). The LAW vitrification melter gas cleaning installation was to include the primary and the secondary gas cleaning systems. The primary system included an FC, a SS and an electrostatic precipitator. The secondary system included a filtering unit (a heater and a HEPA filter), a TKO unit, SCR units and an alkali absorber for iodine-129 and system dioxide removal. The efficiency of NO_x removal was estimated at 99.7%.

2.7. In a 2005, publication [18] described a somewhat different version. The LAW vitrification melter gas cleaning installation included an FC, a SS, a wet electrostatic precipitator, two HEPA filters, a charcoal absorber for mercury removal, a gas heat exchanger, a heater, a TKO unit, two SCR units, a packed alkaline absorber and HEME.

2.8. In 2007, a report assessing the status of the technology of HRW vitrification for the Hanford Waste Treatment and Immobilization Plant (WTP) was published in the USA [22]. The process flow included the primary system comprising: an FC, a SS, a wet electrostatic precipitator, HEME, HEPA (heated to 65ºC to prevent condensation); and the secondary system comprising: TKO and SCR units, an Au-mordenite adsorber and a charcoal adsorber. According to the report, only the SCR unit was designed for NOx_x removal.

2.9. The plant for the vitrification of LRW resulting from WWER and RBMK reactor fuel processing mentioned in 1.13, which included an absorber, also performs NO_x cleaning using an SCR unit [6].

3. Hydrocarbon combustion

As was noted in Section 2, PNNL (USA) issued a report [3] in 1996 reviewing five alternative gas cleaning systems for the process of low-activity waste (LAW). Two of these

(the 2nd and 5th) involved staged hydrocarbon combustion as the main unit of NO_x scrubbing.

3.1. In the second system suitable for all types of melters, gas discharged from the melter is processed in the natural gas combustion chamber installed directly above the melter. The device provides regeneration of approximately 60% of nitrogen oxides into molecular nitrogen. Subsequently, the gas is cooled in a refrigerator evaporator using a sprinkler supplying water which contains suspended solids to prevent the formation of submicronic particles during drop evaporation. The main device used for aerosol removal is a porous metal filter. Volatile metal chlorides and mercury compounds can pass it while in the gaseous form. The cleaned gas flow is discharged from the filter at ~ 340-370°C. This is the temperature most appropriate for the downstream SCR units. After the SCR, sour gases are trapped by the system comprising a refrigerator evaporator which lowers the temperature down to ~ 120°C and an absorber. The alkali-based absorbing liquid with the of pH 6-9 is used to achieve a high efficiency level of HF, HCl, HI and SO_2 absorption. In addition to the removal of sour gases, the absorber system may also be used to trap ammonia residues discharged from SCR. Following that, the HEME system eliminates droplets and condensation aerosol. The heat exchanger located downstream from the HEME serves to heat the gas flow to ~ 70-120°C in order to prevent condensation of the moisture in downstream HEPA filters. Nitrogen oxide removal efficiency is 99.6% (60% in SNCR and 99% in the two SCR units).

3.2. The fifth system is suitable for melters that generate low quantities of aerosols. Flue gas is initially processed in the combustion chamber in order to regenerate nitrogen oxides. Then the gas flow is cooled down to ~ 290-370°C and is transported to SCR units. After these, the scrubber spray dryer is used to remove HF, HCl, HI and SO_2. Lime pulp with the dry solids content of 5-15% by mass is injected into the spray dryer (gas dwell time is 6-20 s). A cloth filter is used to collect dry reaction products from the spray dryer. Design nitrogen oxide removal efficiency is approximately 99.6% (60% in combustion chamber and 99% in the two SCR units).

3.3. A staged combustion unit (NOxidizer™) was tested in the USA in 1996. [23]. Combustion of hydrocarbons was carried out at 1400°C, and supplementary combustion of organic impurities residues - at 1000-1100°C. With the initial volume fraction of NO_x of 3.1% at the unit intake, the removal efficiency was 99.2%.

3.4. According to information published in 2004 and 2005 [24, 18], the system operated at the NWCF installation in the USA since 1982, included a cyclone separator, a spray-type cooler, a Venturi scrubber, a separator, a condenser, a demister, a heater, a packed adsorber for ruthenium removal, three stages of HEPA filters, a two-stage compressor, a demister, a heater and a HEPA filter. The system did not include a dedicated unit for NO_x scrubbing, however. The described system did not meet the environment protection requirements and was put out of operation in 2000. It was proposed to supplement it with staged combustion units to ensure decomposition of NO_x and organic compounds, as well as with a spray-type cooler, a demister, a charcoal adsorber for mercury removal and HEPA filters.

3.5. According to information dated 2004-2005 published in [24, 18], INL developed a project of vitrification of sodic wastes. The gas cleaning system comprised a FC, an acid removal tower, a Venturi scrubber, a high-efficiency demister, a heater, a strainer, a HEPA

filter, a staged combustion unit for NOx,$_x$ decomposition, a sprinkled cooler, an alkali scrubber, a demister, a heater, a charcoal adsorber for mercury removal and a HEPA filter.

No information regarding NO_x removal upstream of the staged combustion unit is available for either of the above systems.

3.6. Tests of the staged combustion unit NOxidizer™) conducted in INEEL were described in 2001 [25, 26]. Two stages of hydrocarbon fuel combustion (at 1300°C and at 1000°C) with the initial volume fraction NO_x of 4% made it possible to reach the removal efficiency of 92 to 97%.

As was mentioned earlier, a research was performed in the USA (INEEL) in 2001 on the simulation of the sodic waste vitrification [20]. The activities involved, among other things, options for gas cleaning system with respect to Hanford and Savannah River facilities' operations.

3.7. The gas cleaning system, being part of process flow at Hanford, included two consecutive FCs, a SS, a wet electrostatic precipitator, a HEME, a heater, HEPA filter No. 1, an alkali scrubber, the staged reduction combustion chamber Noxidizer (1100-1200ºC), a spray cooler (100-500ºC), the oxidation chamber NOxidizer for oxidation of CO and hydrocarbon residues, a packed spray-type cooler, a demister, HEPA filter No. 2 and an adsorber with granular activated carbon for mercury removal.

3.8. The process flow at the Savannah River facility included an FC, an ejector/smoke scrubber, two serially located hydro/sound scrubbers, a condenser, a HEME, HEPA filter No. 1, the staged reduction combustion chamber NOxidizer (1100-1200ºC), and other units as per the Hanford process.

3.9. In 2003, information was published on a pilot installation for LAW and MAW vitrification developed in South Korea which included a flue gas treatment system (FGTS) handling two melters of different types [27]. The FGTS included cooled pipelines, a high-temperature ceramic filter, a secondary combustion chamber a Venturi tube, a four-section liquid-based gas scrubber, a HEPA filter and a SCR unit. 80 tests were conducted with wastes of various origin. Concentrations of impurities in the flue gases discharged from the ventilation system were below permissible levels.

Conclusions

Information about flue gas cleaning systems used in radioactive waste calcination and vitrification installations was analyzed in relation to the problem of nitrogen oxide removal. The information was sourced from 27 publications published in 8 countries over the period since 1978 till the present.

Two distinct approaches to the problem of nitrogen oxide removal were identified:

- absorption by water-based solutions at temperatures approaching room temperature;
- high-temperature reduction (SCR, in combination with SNCR in some cases or combustion of hydrocarbons, often in combination with SCR).

Absorption-based removal is mentioned in earlier studies; later surveys tend towards high-temperature processes, mainly SCR.

Of the 12 gas cleaning systems including absorption-based removal, one system was developed in France, in the United Kingdom and China, 2 systems - in Germany (one operates in Belgium), 3 - in Russia and 4 - in the USA.---

Of the 10 gas cleaning systems that use SCR, 8 are employed in the USA and one in each Russia and South Korea.

Non-selective ammonia reduction is used in one system developed in the USA, in combination with SCR units.

Eight gas cleaning systems that use high-temperature hydrocarbon combustion were developed in the USA and one system - in South Korea.-

The problem was most deeply researched in the USA (19 descriptions). Three systems were developed in Russia, two - in Germany (one system operates in Belgium), one each in France, the United Kingdom, China and South Korea.

In order to meaningfully compare nitrogen oxide removal methods, one must consider that flue gases may contain, in addition to nitrogen oxides, the following components: fission product and glass aerosols, water and nitric acid vapors, ruthenium tetroxide and, in some cases, HF, HCl, HI, I_2 and other impurities.

Liquid-based aerosol entrapment at the initial stage produces large volumes of LRW that need to be returned for secondary treatment which complicates the process. Entrapment of solid aerosols with dry filters (a bulk filter, a MTF, a fibrous glass HEPA filter) requires less space and thus is preferable. Subsequent removal of iodine, ruthenium tetroxide, HF, HCl and HI is also carried out at elevated temperatures using the chemosorption methods. Vapors of nitric acid, water and nitrogen oxides pass through the high-temperature units in the gaseous form. After that, there is a bifurcation in the process. The high-temperature gases are either recovered by ammonia in SCR units supplemented by an additional ammonia deactivation unit, and only after that the gas flow is cooled to condense nitric acid (if it has not been recovered by the SCR unit) and water. Otherwise, the gases are cooled to achieve preliminary acid and water condensation and are reheated again and pass through SCR units.

The SCR technology has its drawbacks:

- the technique is intended for cleaning flue gases of CHPs that are characterized by a relatively uniform flow and low content of nitrogen oxides. This does not agree with high nitrogen oxide content and non-uniform gas flow in vitrification processes;

- the need to introduce an additional unit in order to prevent slip of ammonia, which may develop an explosive situation in increased concentrations (this disadvantage is aggravated by the influx of nitrogen oxides during vitrification operations);

- high cost of catalysts and their tendency to deteriorate in the presence of impurities contained in flue gases;

- the provisional low performance of nitrogen oxide removal by a single unit (due to low ammonia supply to prevent its slip);

- possible formation of environment-damaging and hard-to-remove nitrous oxide.

The option which involves cooling of flue gases after the bifurcation includes collection of water and acid condensate. At this stage, absorption-based removal of nitrogen oxides is possible. Nevertheless, the absorption processes and installations described in the overview provide nitrogen oxide removal with a low efficiency. Thus, based on the information

included in the overview, passing flue gases through a SCR unit seems preferable despite the stated disadvantages since it allows to achieve high efficiency by using a series of such units.

SNCR and hydrocarbon combustion (Noxidizer) at high (over 1000°C) temperatures are viable, and are more often than not applied at the melter discharge. However, in most cases their efficiency is low and they must be used along with an SCR unit. Besides, hydrocarbon combustion impairs the safety level of the gas cleaning system due to associated explosion and fire hazards.

Sequential cooling and heating of flue gases before transporting them into the mentioned SCR units increases the complexity and cost of the system.

It should also be noted that HEME, HEPA, SCR, SNCR, NOxidizer and other systems must be disposed as hazardous SRW after their decommissioning.

Based on the above, we can conclude that technologies of gas cleaning in conclusion and vitrification processes are complex and costly, but necessary. Ultimately, the use of various methods of nitrogen oxide removal is defined by the specific vitrification process and the properties of the gases formed during the process.

List of abbreviations

HRW – highly radioactive waste

WWER – pressurized water type reactor

LRW – liquid radioactive waste

L-RW – low-radiation waste

SS – submerged scrubber

FC – film cooler

RAW – radioactive waste

RBMK – boiling water cooled graphite moderated pressure tube type reactor

ILW – intermediate level waste

SCR – selective catalytic reduction

SNCR – selective non-catalytic reduction

FGTS – flue gas treatment system-

TCO – thermocatalytic oxidation

SRW – solid radioactive waste

EP-100 – electric melter with the solution output rate of 100 dm^3/h

EP-500 – electric melter with the solution output rate of 500 dm^3/h-

AVM - Atelier Vitrification Marcoule (Установка остекловывания в Маркуле)

DBVS - Demonstration Bulk Vitrification System (Демонстрационная система насыпного остекловывания)

HEME – high efficiency mist eliminator (высокоэффективный туманоуловитель)

HEPA - high efficiency particulate air filter (высокоэффективный фильтр взвешенных частиц)

INEEL - Idaho National Engineering and Environmental Laboratory (Национальная инженерная и экологическая лаборатория Айдахо)

INL - Idaho National Laboratory (Национальная лаборатория Айдахо)

NWCF - New Waste Calcining Facility (Новая установка кальцинирования отходов)

PNL - Pacific Northwest Laboratory (Тихоокеанская северо-западная лаборатория)

PNNL - Pacific Northwest National Laboratory (Тихоокеанская северо-западная национальная лаборатория)

RPP – River Protection Project (Проект защиты рек)

WVDP - West Valley Demonstration Project (Демонстрационный проект Уэст Вэлли)

References

1. Design and operation of off-gas cleaning systems at high level liquid waste conditioning facilities. Technical reports series No. 291. Vienna: IAEA, 1988, P. 52-55.

2. Handbook: Vitrification Technologies for Treatment of Hazardous and Radioactive Waste. EPA/625/R-92/002. Washington: USEPA, 1992, 100 p.

3. Peurrung L. M., Deforest T. J., Richards J. R. Process System Evaluation - Consolidated Letter Reports. Volume 1 – Alternatives for the Off-Gas Treatment System for the Low-Level Waste Vitrification Process. PNNL-11056. Richland, Washington: Pacific Northwest National Laboratory, , 1996, 108 p.

4. Wood R.A. Modeling of NO_x Destruction Options for INEEL Sodium-Bearing Waste Vitrification. INEEL/EXT-01-01220., Bechtel BWXT Idaho: Idaho National Engineering and Environmental Laboratory, LLC, 2001, 81 p.

5. Treatment of radioactive gaseous waste. Vienna: International Atomic Energy Agency, 2014, 53 p. — (IAEA-TECDOC series, ISSN 1011–4289; No. 1744).

6. CD-ROM: Capture, Retention and Conditioning of Gaseous Radioactive Waste.. Annex to "Treatment of Radioactive Gaseous Waste" Vienna: IAEA, 2014,494 p.

7. Design and Operation of Off-gas Cleaning Systems at High Level Liquid Waste Conditioning Facilities. Technical Reports Series No. 291. Vienna, IAEA: 1988. p. 48-51.

8. Hanson M.S., Goles R.W., Hamilton D.C. Behaviour of selected contaminants in spray calciner/in-can melter waste vitrification off-gas. // IAEA-SM-245/24. Management of Gaseous Wastes from Nuclear Facilities. Proceedings of a symposium, Vienna, 18-22 February 1980, jointly organized by IAEA and NEA (OECD). Vienna: IAEA, 1980, p. 371-391.

9. Wheelwright E. J., Bjorklund W. J., Browne L. M. et al. Technical Summary Nuclear Waste Vitrification Project. PNL-3038, Richland, Washington: Pacific Northwest Laboratory 1979 – 87 p.

10. Goles R. W., Hamilton D. C., Brauer F. P. et al. Characterization of Gaseous and Particulate Effluents from the Nuclear Waste Vitrification Project. PNL-3181, Richland, Washington: Pacific Northwest Laboratory, 1979 – 37 p.

11. Weisenburger S., Seiffert H. Off-gas cleanup system designed for HLLW vitrification in a liquid-fed ceramic waste melter. // IAEA-SM-245/36. Management of Gaseous Wastes from Nuclear Facilities. Proceedings of a symposium, Vienna, 18-22 February 1980, jointly organized by IAEA and NEA (OECD). Vienna, IAEA, 1980, p. 531-543.

12. Design and Operation of High Level Waste Vitrification and Storage Facilities. Technical reports series No. 339. Vienna: IAEA, 1992, p 31-36.

13 Beveridge G.D. Product quality and process control in the Windscale Vitrification Plant. High Level Radioactive Waste Management. // Proceedings of the Second Annual International Conference Las Vegas, Nevada, April 28-May 3, 1991. La Grange Park, Illinois, USA: American Nuclear Society, Inc., New York, New York, USA: American Society of Civil Engineers,. Vol. 1, p. 420-426.

14. Bradshaw K., Gribble N.R., Hughes D.O., Riley A.D. UK Full-Scale Non-active vitrification development and implementation of research findings onto the waste vitrification plant. // WM'07 Conference, February 26-March 2, 2007, Tucson, AZ. – 15 p.
15. Design and Operation of High Level Waste Vitrification and Storage Facilities. Technical reports series No. 339. Vienna: IAEA, 1992, p 48-51.
16. Design and Operation of High Level Waste Vitrification and Storage Facilities. Technical reports series No. 339. Vienna: IAEA, 1992, p. 57-63.
17 Design and Operation of High Level Waste Vitrification and Storage Facilities. Technical reports series No. 339. Vienna, IAEA, 1992, p. 63-65.
18. Soelberg N. Advanced Off-Gas Control System Design for Radioactive and Mixed Waste Treatment. INL/CON-05-00658 Preprint. Idaho National Laboratory, 2005. – 9 p.
19. Vance R.F., Brill B.A., Carl D.E. et al. Design of Equipment Used for High-level Waste Vitrification at the West Valley Demonstration Project. Topical Report DOE/NE/44139-73, West Valley, NY: West Valley Nuclear Services Company, Inc., June 1997, 74 p.
20. Nichols T.T., Taylor D.D., Lauerhass L., Barnes C.M. Process Option Description for Vitrification Flowsheet Model of INEEL Sodium Bearing Waste, INEEL/EXT-01-00173, Idaho Falls, Idaho, Idaho: National Engineering and Environmental Laboratory High Level Waste Program, February 2001, 50 p.
21. Anderson T.D., Fergestrom L.J. An offgas system for a low activity waste melter. // 26th Nuclear Air Cleaning & Treatment Conference, 2000, 15 p.
22. Holton L., Alexander D., Babel C. et al. Technology Readiness Assessment for the Waste Treatment and Immobilization Plant (WTP) HLW Waste Vitrification Facility. 07-DESIGN-046. U.S. Department of Energy, Office of River Protection, August 2007, 116 p.
23. Battleson D.M., Johnson S.E., Montgomery J.L. et al. NOxidizer™ System for High-level NO_x Reduction Preliminary Test Results at MSE Technology Applications, Inc.'s Off-gas Test Unit. Butte, Montana: MSE Technology Applications, 3 p.
24. Barnes C.M., Olson A.L., Taylor D.D. Sodium-Bearing Waste Treatment Technology Evaluation Report. INEEL/EXT-04-01692. Idaho National Engineering and Environmental Laboratory, Bechtel BWXT Idaho, LLC, 2004. – 541 p.
25 Marshall D.W. FY-2001 Accomplishments in Off-Gas Treatment Technology Development. INEEL/EXT-01-01302., Bechtel BWXT Idaho, LLC: Idaho National Engineering and Environmental Laboratory, 2001. – 15 p.
26. Barnes C.M., Taylor D.D. Review of FY2001 Development Work for Vitrification of Sodium Bearing Waste. INEEL/EXT-02-00194. Bechtel BWXT Idaho, LLC:
Idaho National Engineering and Environmental Laboratory, 2002. – 112 p.
27. Miung-Jai Sangh. Vitrified waste // Foreign Nuclear Engineering, 2003, No. 10 pp. 14-18.

UDC: 669.781

THERMODYNAMIC SIMULATION OF VARIOUS OPTIONS OF BORON TRICHLORIDE SYNTHESIS

A. A. Tsurika[1], A. A. Syemenov[2], A. V. LIzunov[2]
[1]JSC Solikamsk Magnesium Works (JSC SMW),
618541, Perm Territory, Solikamsk, 9 Pravdy Str.
[2]SC «A.A. Bochvar High-Technology Research Institute of Inorganic Materials»,
Moscow

The article discusses various options of boron trichloride synthesis. It reviews main types of boron-containing materials and instruments produced by JSC SMW that can be used for chlorination of these materials. A thermodynamic analysis of various boron trichloride synthesis options and their economic assessment are presented. Drawbacks and advantages of various chlorinating agents are discussed in their application to various types of initial boron-containing raw materials, as well as specifics of chlorination process organization. Recommendations on the procedure for boron trichloride synthesis are formulated with regard to engineering capabilities of JSC SMW in relation to processes involving chlorine.

Keywords: boron trichloride, boron isotope separation, chlorination, chlorinator, chlorinating agent, boric acid, borax, sodium tetraborate, boron carbide, ferroboron, magnesium boride, thermodynamic analysis.

Introduction

Boron trichloride is used in various fields of research and technology. It is used as a polymerization and synthesis catalyst in Friedel-Crafts type reactions when synthesizing boron hydride and organoboron compounds, in the production of high-purity boron and metal borides, as well as a reagent in boron nitride synthesis, as the agent for extinguishing burning magnesium, etc. [1, pp. 131-132]. Besides the above, boron trichloride is considered as a potential working substance in boron isotope separation. In this regard, the substance is of interest for the national nuclear industry which has experienced a severe shortage [5] of materials with a high content of boron-10 content in recent decades. The cataclysmic collapse of the Soviet Union 26 years ago resulted in the fact that the only enriched boron-10 production facility in the USSR, Research Institute for System Studies, located in Tbilisi was isolated from the Russian Federation. Despite the numerous attempts to establish national boron-10 production facilities in Russia, the issue of import-independent supply of the nuclear industry enterprises with this isotope has not been solved to date. Apart from the challenges relating to the organization of isotope isolation itself, there is also the problem of providing such a facility with source working substances.

Presently, the most feasible process of boron isotope separation is the so-called anisole process which uses boron trifluoride as a working substance [6, 7]. The process involves the reaction of chemical isotope exchange between gaseous boron trifluoride and its liquid complex formed with anisole:

$$^{10}BF_{3\ (g)} + {}^{11}BF_3 \cdot C_6H_5OCH_{3\ (l)} = {}^{11}BF_{3\ (g)} + {}^{10}BF_3 \cdot C_6H_5OCH_{3\ (l)} \quad (1)$$

The reaction (1) is shifted to the right, and features a rather high isotope separation factor α, which reaches the value of 1.03 in this reaction. This separation process is very practical, as the reversal of flows within the column is produced thermally: the anisole complex is decomposed due to heating in the lower part, while gaseous boron trifluoride returns to the counterflow separation process, and cooled anisole binds the gaseous trifluoride with the liquid anisole complex in the upper part of the column, which subsequently irrigates the separation column. Thus, the anisole process of boron isotope separation combines the advantage of chemical exchange processes (that provide a high isotope separation factor) and the convenient thermal flow reversal which is typical for rectification processes. In Russia, the anisole process of boron isotope separation was implemented at RISS (located in Tbilisi).

The second most widely used method of boron isotope separation is low-temperature rectification of boron trifluoride [7]. This method has a lower isotope separation factor (α of up to 1.007) and requires constant low temperatures (190-200 K), nevertheless, this is feasible in some cases. Here, boron fluoride-10 is also concentrated at the liquid phase. In the USSR, a boron trifluoride rectification column operated successfully producing tens of kilograms of boron-10-enriched product per year.

Rectification of boron trichloride as a method of boron isotope separation has an even lower separation factor ($\alpha\approx$ of 1.003). This makes the process labor-intensive and inefficient [7]. Besides the above, it is currently unknown whether this method can produce a product highly enriched with boron-10 since boron trichloride also contains various isotopes of chlorine and thus it is made up of 8 isotopomers, and thus far the distribution pattern of chlorine isotopes during the rectification of this chemical compound is unknown. Despite the above challenges, application of boron trichloride as a working substance in boron isotope separation was and is considered in several works [2-4]. This is due to a more favorable temperature range of $BCl3_3$ rectification, its wider accessibility and lower toxicity and cost as compared to BF_3.

Boron trichloride BCl_3 is a colorless liquid fuming in moist air, having the boiling point of 12.6 °C, the density of 1.343 g/cm^3 (at 11°C) and the critical thermal point of 178.8°C [1, p. 128]. BCl_3 is soluble in carbon, silicon and titanium tetrachlorides, sulfur chlorides SCl_2 and S_2Cl_2 and liquid SO_2. Water hydrolyzes $BCl3_3$ and forms a mixture of chlorine hydride and boric acid. Being a Lewis acid, boron trichloride forms adduct compounds with ethers, amines and chlorides of other elements. This property is used in a convenient method of storing boron trichloride as a solid adduct compound with dimethyl sulfide from which it may be extricated by way of thermal decomposition. Boron trichloride reacts with alcohols by forming relevant boric acid ethers.

Following the collapse of the Soviet Union, production of both boron trichloride and trifluoride has been halted. Presently, it appears that no bulk production of boron trichloride exists in Russia. Disintegration of the mining industry infrastructure resulted in the deterioration of the national production of boron-containing raw materials. Nevertheless, boric acid is being manufactured and marketed by some three dozens of Russian enterprises. Besides, it is also supplied to Russia from abroad, and is not considered a scarce product [8]. Publications [1, pp. 132-139] mention a method of industrial-scale production of boron trichloride by way of chlorination of boric anhydride or of dry sodium tetraborate with gaseous chlorine in the presence of coke deoxidant, charcoal or carbon monoxide. The options of chlorination of boric anhydride in molten salts and using carbon tetrachloride as a chlorination agent were also considered. A thermodynamic comparison of different methods of boron trichloride production with considering specifics of the unique capabilities of the longest-standing Russian chlorine manufacturing facility, namely Solikamsk Magnesium Works, is of certain interest.

This is the objective of the research.

Initial materials and reagents

1. Boric acid H_3BO_3 is the most readily available feed. However, it is hard to dehydrate, it is highly volatile in water vapors at 160-500°C, and even at 500°C the molten substance contains 5% of water [9]. Boric oxide B_2O_3 produced by anhydrification of H_3BO_3 cannot be chlorinated without complete dehydration since the yield of $BCl3_3$ will be lower due to hydrolysis.

Nevertheless, to obtain boric oxide B_2O_3 in industrial-scale production, methods of gradual dehydration of H_3BO_3 both in vacuum and at normal atmospheric pressure and the temperature of 250-300°C are employed to produce 98 to 99% B_2O_3 [10, pp. 248-249].

This material is quite suitable for chlorination which produces BCl_3.

According to estimates, B_2O_3 contains up to 31% of boron and, respectively, up to 69% of oxygen.

2. Sodium tetraborate $Na_2B_4O_7$ is produced by dehydration of decahydrate, the borax mineral $Na_2B_4O_7 \cdot 10H_2O$- under temperatures of 350 to 400 °C [11, p. 313]. Borax is dehydrated more easily and effectively than boric acid, besides, it does not evaporate with water vapor.

Dehydrated sodium tetraborate $Na_2B_4O_7$ is very much suitable as a material for chlorination; it contains up to 23% of sodium, up to 21.5 % of boron and more than 55.5% of oxygen.

3. Boron carbide B_4C is a black colored substance produced by way of synthesis from boron and carbon at temperatures exceeding 1,300°C [12, p. 1, p. 148] and the decomposition temperature of over 2,450°C [13, p. 79]. Boron carbide can also be produced by reducing B_2O_3 in furnaces using carbon. B_4C is not produced in Russia, it is purchased in China.

Boron carbide B_4C contains up to 78.3% of boron and up to 21.7% of carbon.

4. Ferroboron is the alloy of iron which contains 8 to 20% or more of boron (as per GOST 14849-69). It has been in use since 1893, and is produced using the ladle metallothermic method or is extracted by melting in electric furnaces from boron-containing ores [12, vol. 2, pp. 638-639].

The following alloy composition was assumed for estimation: 16.2% of boron, 83.8% of iron (FeB).

5. Magnesium borides MgB_2 to MgB_{12} are formed as intermediate products of magnesiothermic reduction of boron oxide. Magnesium metal is the most effective reducer of B_2O_3,, and the magnesiothermy method is the most widespread industrial method of boron production [14, p. 128-140].

The magnesiothermy method of boron oxide reduction produces boron which is contaminated with magnesium to a certain degree in the form of various magnesium borides. The degree of contamination depends on the process conditions. At temperatures of about 900°C, the initial reaction within the furnace mixture

$$B_2O_3 + 3Mg = 2B + 3MgO \qquad (2)$$

also forms MgB_{12} and includes other secondary processes [14, p. 132].

The maximum output of boron does not comply with stoichiometry but is rather the result of magnesium surplus. The highest content of boron in products of reduction under laboratory environment is achieved by using the reaction mix consisting of 35% w/w% of Mg. After removing all the magnesium content in acid, the product contains 88.6% of boron [14, p. 133].

Let us assume that magnesiothermic boron contains 88.9% of B and 11.1% of Mg (MgB_{18}).

6. We will consider combinations of chlorine with carbon (in the form of graphite) or with sulfur (in the form of vapors) as boron oxide and sodium tetraborate chlorinating agents. Boron carbide, ferroboron and elemental boron with magnesium impurities are chlorinated using gaseous chlorine and do not require addition of graphite or sulfur into the reaction mix.

Thermodynamics of chlorination processes

The objective of thermodynamic analysis presented by this article is determination of temperature dependency of Gibbs energies and equilibrium constants of chemical reactions of boron trichloride $BCl3_3$ synthesis during chlorination of non-metallic and metallic boron-containing materials. Additionally, thermal effects or reaction enthalpies were estimated for the purpose of calculating thermal balances of chlorination apparatuses.

In order to ensure acceptable chlorination reaction speeds and yields using the experimental data [1, p. 133], let us assume the temperature range of chlorination and thermodynamic calculation of relevant reactions at 500 to 900°C (773 to 1173 K).

Table 1 states thermodynamic properties of the substances participating in intended boron trichloride $BCl3_3$ synthesis reactions for the selected range of temperatures under chlorination of the above boron-containing materials.

TABLE 1

Thermodynamic properties of substances [13, 16, 17]

Substance	Phase	$\Delta H^{o}_{T_П}$, kJ/mol	$\Delta S^{o}_{T_П}$, J/(K·mol)	T_p, K	ΔH^{o}_{p}, kJ/mol	$s_r = a + b\cdot T + s\cdot T^{-2}$, J/(K·mol)			Range ΔT, K
						a	$b\cdot10^{3}$	$c\cdot10^{-5}$	
B	s	0	5.86	298	–	19.82	5.78	-9.21	298-1,700
B_4C	s	-71.6	27.1	298	–	96.25	22.61	-44.88	298-1373
BCl_3	g	-403.2	290.1	298	–	80.33	1.19	-16.19	298-2000
B_2O_3	l	-1254	78.5	723	22.2	127.7	0	0	723-1800
$C_{(graphite)}$	s	0	5.74	298	–	24.46	0.435	-31.65	298-4000
CO_2	g	-393.8	213.8	298	–	44.17	9.04	-8.54	298-2000
Cl_2	g	0	223.1	298	–	36.93	0.25	-2.85	298-3000
$Fe_{\alpha,\delta}$	s	0	27.3	298	–	37.15	6.17	0	298-1809
H_2	g	0	130.67	–	–	27.30	3.266	0.502	298-3000
HCl	g	-92.37	186.91	298	–	26.25	5.19	1.26	298-2000
Mg*	s	0	32.7	298	–	22.32	10.26	-0.43	298-922
	l	26.6	74.1	922	8.8	32.66	0	0	922-1150
$MgCl_2$*	s	-642	89.7	298	–	79.13	5.945	-8.625	298-987
	l	-539.7	236.6	987	43.1	92.53	0	0	987-1500
$NaBO_2$	s	-976	74	298	–	50.66	53.72	0	298-1239
	l	–	–	1239	36.3	146.5	0	0	>1239
$Na_2B_4O_7$*	s	-3291	190	298	–	229	107.44	0	298-1015
	l	-2981	641	1015	94.8	420.7	0	0	>1015
NaCl*	s	-412.9	72.2	298	–	45.97	16.33	0	298-1074
	l	-340.5	169.9	1074	28.0	66.99	0	0	1074-1738
$NaFeCl_4$*	s	-813.7	192.8	298	–	136.8	28.93	0	298-436
	l	-775.3	290.1	436	18.0	198.9	0	0	436-1257
S_2	g	128.7	228.2	298	–	36.51	0.67	-3.77	298-3000
SO_2	g	-297.1	248.2	298	–	43.46	10.63	-5.94	298-2000

*Enthalpy and entropy of liquid magnesium after smelting at the temperature of 922 K:

$\Delta H^{o}_{922}(Mg_l) = 0 + [22.32\cdot(922–298) + 10.26\cdot10^{-3}\cdot(922^2–298^2)/2 – 0.43\cdot10^{5}\cdot(1/922–1/298)]/1000 + 8.8 = 26.6$ kJ/mol,

$\Delta S^{o}_{922}(Mg_l) = 32.7 + 22.32\cdot(\ln922–\ln298) + 10.26\cdot10^{-3}\cdot(922–298) – 0.43\cdot10^{5}\cdot(1/922^2–1/298^2)/2 + 8.8\cdot10^{3}/922 = 74.1$ J/(K·mol).

Enthalpy and entropy of liquid magnesium chloride after smelting at the temperature of 987 K:

$\Delta H^{o}_{987}(MgCl_{2l}) = –642 + [79.13\cdot(987–298) + 5.945\cdot10^{-3}\cdot(987^2–298^2)/2 – 8.625\cdot10^{5}\cdot(1/987–1/298)]/1000 + 43.1 = –539.7$ kJ/mol,

$\Delta S^{o}_{987}(MgCl_{2l}) = 89.7 + 79.13\cdot(\ln987–\ln298) + 5.945\cdot10^{-3}\cdot(987–298) – 8.625\cdot10^{5}\cdot(1/987^2–1/298^2)/2 + 43.1\cdot10^{3}/987 = 236.6$ J/(K·mol).

Enthalpy of formation of $Na_2B_4O_7$ from $NaBO_2$ and B_2O_3 in the reaction of $2NaBO_{2s} + B_2O_{3l} = Na_2B_4O_{7s}$ is

$\Delta H^{o}_{298} = \Delta H^{o}_{298}(Na_2B_4O_7) – 2\cdot\Delta H^{o}_{298}(NaBO_2) – \Delta H^{o}_{298}(B_2O_3) = –3291 – 2\cdot(–976) – (–1254) = –85$ kJ/mol $Na_2B_4O_7$.

Since enthalpy of the reaction of combination $NaBO_2$ and B_2O_3 is of low importance as compared with the enthalpy of formation of these substances, the properties of $Na_2B_4O_7$ will be similar to those of $NaBO_2$+B_2O_3 when taken in mole ratio of 2:1. The thermal capacity of solid $Na_2B_4O_7$ can be estimated using the rule of additivity from respective thermal capacities of solid $NaBO_2$ and liquid B_2O_3:

$\Delta c_p\ (Na_2B_4O_{7s}) = 2\cdot\Delta c_p\ (NaBO_{2s}) + \Delta c_p\ (B_2O_{3l}) = 2\cdot(50.66 + 53.72\cdot10^{-3}\cdot T) + 127.7 = 229 + 107.44\cdot10^{-3}\cdot T$, J/(K·mol),

$\Delta c_p(Na_2B_4O_{7l}) = 2\cdot\Delta c_p\ (NaBO_{2l}) + \Delta c_p\ (B_2O_{3l}) = 2\cdot146.5 + 127.7 = 420.7$ J/(K·mol).

The enthalpy of melting, $\Delta H^o_m\ (Na_2B_4O_7) = 2\cdot\Delta H^o_m\ (NaBO_2) + \Delta H^o_m\ (B_2O_3) = 2\cdot36.3 + 222 = 94.8$ kJ/mol.

Enthalpy and entropy of liquid sodium tetraborate $Na_2B_4O_7$ at 1015 K is:

$\Delta H^o_{1015}\ (Na_2B_4O_{7l}) = -3291 + [229\cdot(1015-298) + 107.44\cdot10^{-3}\cdot(1015^2-298^2)/2]/1000 + 94.8 = -2981$ kJ/mol,

$\Delta S^o_{1015}\ (Na_2B_4O_{7l}) = 190 + 229\cdot(\ln1015-\ln298) + 107.44\cdot10^{-3}\cdot(1015-298) + 94.8\cdot10^3/1015 = 641$ kJ/(K·mol).

Enthalpy and entropy of liquid sodium chloride after smelting at the temperature of 1074 K:

$\Delta H^o_{1074}\ (NaCl_l) = -412{,}9 + [45.97\cdot(1074-298) + 16.33\cdot10^{-3}\cdot(1074^2-298^2)/2]/1000 + 28.0 = -340.5$ kJ/mol,

$\Delta S^o_{1074}\ (NaCl_l) = 72{,}2 + 45.97\cdot(\ln1074-\ln298) + 16.33\cdot10^{-3}\cdot(1074-298) + 28.0\cdot10^3/1074 = 169.9$ J/(K·mol).

Enthalpy and entropy of liquid sodium tetrachloroferrate (III) $NaFeCl_4$ after smelting at the temperature of 436 K:

$\Delta H^o_{436}\ (NaFeCl_{4l}) = -813.7 + [136.82\cdot(436-298) + 28.93\cdot10^{-3}\cdot(436^2-298^2)/2]/1000 + 18.0 = -775.3$ kJ/mol,

$\Delta S^o_{436}\ (NaFeCl_{4l}) = 192.8 + 136.82\cdot(\ln436-\ln298) + 28.93\cdot10^{-3}\cdot(436-298) + 18.0\cdot10^3/436 = 290.1$ J/(K·mol).

The thermodynamic calculation of the reactions uses the Tiomkin-Schwartzman method [15] which allows to replace integrals of substance thermal capacity variation

$$\Delta c_p = \Delta a + \Delta b\cdot T + \Delta d\cdot T^{-2} + \Delta e\cdot T^2 \qquad (3)$$

in the expression used for the calculation of Gibbs energy [16]:

$$\Delta G^o_T = \Delta H^o_{298} - T\cdot\Delta S^o_{298} - T\cdot\int_{298}^{T} dT/T^2\cdot\int_{298}^{T}\Delta c_p\cdot dT = \Delta H^o_{298} - T\cdot\Delta S^o_{298} + \int_{298}^{T}\Delta c_p\cdot dT - T\cdot\int_{298}^{T}(\Delta c_p/T)dT, \qquad (4)$$

with tabled coefficients M_0, M_1, M_{-2} and M_2. This simplifies the calculations without impairing computational accuracy. The dependence of ΔG^o_T on the temperature is expressed as follows [15]:

$$\Delta G^o_T = \Delta H^o_{298} - T\cdot\Delta S^o_{298} - T\cdot(M_0\cdot\Delta a + M_1\cdot\Delta b + M_{-2}\cdot\Delta d + M_2\cdot\Delta e), \qquad (5)$$

where coefficients M_0, M_1, M_2 and M_{-2} are functions of temperature only [15]:

$$M_0 = \ln(T/298.15) + 298.15/T - 1, \qquad (6)$$

$$M_1 = (T - 298.15)^2/(2T), \qquad (7)$$

$$M_2 = T^2/6 + (298.15)^3/(3T) - (298.15)^2/2, \qquad (8)$$

$$M_{-2} = (1/298.15 - 1/T)^2/2. \qquad (9)$$

If the substances undergo phase transitions in the temperature range considered, application of the Tiomkin-Schwartzman formula becomes more problematic [18].

Thermodynamic properties of substances change abruptly at transformation points when a different phase forms. In the formula (5), calculation of ΔG^{o}_{T} begins at the standard temperature of 298 K (25°C). After the phase transition of the substances involved in reaction, the dependency $\Delta G^{o}_{T} = f(T)$ is no longer valid, thus after each phase transition at T_t of any of the substances within the temperature range of $T_t \div T$, the formula (5) has the following form:

$$\Delta G^{o}_{T} = \Delta H^{o}_{T\Pi} - T \cdot \Delta S^{o}_{T\Pi} - T \cdot (M_0 \cdot \Delta a + M_1 \cdot \Delta b + M_{-2} \cdot \Delta d + M_2 \cdot \Delta e), \quad (10)$$

where $\Delta H^{o}_{T\Pi}$ and $\Delta S^{o}_{T\Pi}$ are values of enthalpy variation following the phase transition at T_t of the respective substance. The formula (10) is more general than the formula (5).

ΔH^{o}_{T} and ΔS^{o}_{T} can be calculated using the following formulas [16]:

$$\Delta H^{o}_{T} = \Delta H^{o}_{298} + \Sigma[a_i \cdot (T - T_i) + b_i \cdot (T^2 - T_i^2)/2 - d_i \cdot (1/T - 1/T_i) + e_i \cdot (T^3 - T_i^3)/3]/1000 + \Sigma \Delta H^{o}_{i}; \quad (11)$$

$$\Delta S^{o}_{T} = \Delta S^{o}_{298} + \Sigma[a_i \cdot (\ln T - \ln T_i) + b_i \cdot (T - T_i) - d_i \cdot (1/T^2 - 1/T_i^2)/2 + e_i \cdot (T^2 - T_i^2)/2] + \Sigma \Delta H^{o}_{i} \cdot 10^3/T_i, \quad (12)$$

where a_i, b_i, d_i and e_i are the coefficients of the thermal capacity equation $\Delta c_p = \Delta a + \Delta b \cdot T + \Delta d \cdot T^{-2} + \Delta e \cdot T^2$ of the reaction within the temperature range of $T_i \div T$ from the i-th phase transition having the enthalpy of ΔH^{o}_{i}.

Based on the resulting values ΔG^{o}_{T}, the values of equilibrium constants K_e may be calculated for respective temperatures using the formula:

$$K_e = \exp[-\Delta G^{o}_{T}/(R \cdot T)] = \exp[-\Delta G^{o}_{T}/(8.31441 \cdot T)]. \quad (13)$$

In order to formulate thermal balances of processes, it is important to know their specific enthalpy values in terms of one gram or kilogram of reagent.

$$\Delta H^{o}_{уд} = -\Delta H^{o}_{T}/M \text{ [J/g or kJ/kg (MJ/kg)]}, \quad (14)$$

where M, g/mol or kg/mol is the molar weight of the reagent. For chlorine $M(Cl_2)$ this equals to 70.9 g/mol.

Dependencies of functions ΔG^{o}_{T}, ΔH^{o}_{T}, ΔS^{o}_{T}, K_e and $\Delta H^{o}_{уд}$ from absolute temperature T were calculated using batch value calculation functions of Microsoft Excel. These dependencies (with the exception of K_e) are not much different from linear ones and are approximated to linear equations when using the least square method.

The calculation results are presented below for reactions of chlorination of various types of boron-containing feed at selected temperatures, within the range of 500-900°C (773, 873, 973, 1073 and 1173 K) and at phase transition points of respective substances.

1. Chlorination of the mix of B_2O_3 and graphite at 500-900°C according to reaction equation:

$$2B_2O_{3l} + 3C_{(graphite)} + 6Cl_{2g} = 4BCl_{3g} + 3CO_{2g}. \quad (15)$$

Chlorination produces a mixture of boron trichloride and carbon dioxide.

The calculation of thermodynamic functions of BCl_3 synthesis in the reaction (15) is presented in Table 2.

TABLE 2

Functions of synthesis of BCl_3 in the reaction (15) at temperatures of 773÷1173 K

Function ΔF^o_T	Temperature T, K					$\Delta F^o_T = A + B \cdot T$		
	773	873	973	1073	1173	A^*	$B^* \cdot 10^3$	$\pm\delta^*$
$-\Delta H^o_T$, kJ/mol Cl_2	52.52	53.61	54.68	55.72	56.72	-44.422	-10.51	0.0286
ΔS^o_T, J/(K·mol Cl_2)	38.91	37.58	36.42	35.40	34.51	47.239	-10.97	0.1362
$-\Delta G^o_T$, kJ/mol Cl_2	82.60	86.42	90.12	93.71	97.21	-54.49	-36.50	0.1023
K_e	$3 \cdot 10^{33}$	$1 \cdot 10^{31}$	$1 \cdot 10^{29}$	$2 \cdot 10^{27}$	$9 \cdot 10^{25}$	–	–	–
$\Delta H^o_{уд}$, MJ/kg Cl_2	0.7408	0.7561	0.7712	0.7859	0.8000	0.6266	0.1482	0.0044

*Coefficients A and B in functions ΔF^o_T were calculated according to the least square method based on the values stated in the tables using the formulas:

$$A = [\Sigma X \cdot \Sigma(X \cdot Y) - \Sigma X^2 \cdot \Sigma Y] / [(\Sigma X)^2 - N \cdot \Sigma X^2],$$

$$B = [\Sigma X \cdot \Sigma Y - N \cdot \Sigma(X \cdot Y)] / [(\Sigma X)^2 - N \cdot \Sigma X^2],$$

where X are values of points along the X axis (the temperature),

Y are values of points along the Y axis (the function),

N is the number of value points (in our case, 5),

$\pm\delta$ is the mean-square deviation from the linear dependence:

$$\pm\delta = [\Sigma(A + B \cdot T - \Delta F^o_T)^2 / (N - 1)]^{0.5}.$$

The results stated in Table 2 allow us to conclude that synthesis of boron trichloride by chlorination of the boron oxide-carbon mixture is a medium-energy chemical process with a reasonable decrease of enthalpy and Gibbs energy, high values of equilibrium constants and a low specific chlorination heat. Based on practical experience of JSC SMW, an effective implementation of such processes would require external heating of the reaction mixture to temperatures of about 500°C or higher.

When carrying out chlorination using a solid reducer, carbon in the form of coke, the coke must be broken down into particles with the sizes of < 0.1 mm and a 3 to 4-fold excess of the reducer to achieve the acceptable speeds and degree of chlorination.

The method of reductive chlorination using the mixture of chlorine and vapor of reducers -- sulfur chlorides $SCl_2 + S_2Cl_2$. These are active chlorine-based agents produced by passing chlorine above sulfur, however, at room temperature. To carry out chlorination of oxygen compounds, chlorine is first passed through the mixture of liquid sulfur chlorides at temperatures of 38÷40 °C [19] at which the gaseous phase reaches an equilibrium atomic ratio of S to Cl which is approximately equal to 1: 4 [20].

Thermal dissociation of SCl_2 occurs at temperatures above 100°C, and that of S_2Cl_2 – above 300°C [21, p. 21]. For this reason, S_2 disulfur vapor was used in calculations at temperatures > 500°C.

The equation of reaction B_2O_3 with chlorine mixed with disulfur vapor at 500-900°C is as follows:

$$4B_2O_{3l} + 3S_{2g} + 12Cl_{2g} = 8BCl_{3g} + 6SO_{2g}. \quad (16)$$

Chlorination produces a mixture of boron trichloride and sulfur dioxide.

The calculation of thermodynamic functions of BCl_3 synthesis in the reaction (16) is presented in Table 3.

TABLE 3

Functions of synthesis of BCl_3 in the reaction (16) at temperatures of 773÷1173 K

Function ΔF^o_T	Temperature T, K					$\Delta F^o_T = A + B \cdot T$		
	773	873	973	1073	1173	A	$B \cdot 10^3$	$\pm\delta$
$-\Delta H^o_T$, kJ/mol Cl_2	38.50	39.52	40.44	41.29	42.06	-31.706	-8.896	0.0745
ΔS^o_T, J/(K·mol Cl_2)	-3.60	-4.84	-5.84	-6.67	-7.36	3.438	-9.351	0.1693
$-\Delta G^o_T$, kJ/mol Cl_2	35.72	35.29	34.76	34.13	33.43	-40.252	5.741	0.0868
K_e	$9 \cdot 10^{28}$	$2 \cdot 10^{25}$	$2 \cdot 10^{22}$	$9 \cdot 10^{19}$	$7 \cdot 10^{17}$	–	–	–
$\Delta H^o_{уд}$, MJ/kg Cl_2	0.5430	0.5574	0.5704	0.5824	0.5932	0.4472	0.1254	0.0032

Table 3 allows us to conclude that synthesis of boron trichloride by chlorination of boron oxide using chlorine-disulfur vapor mixture is also a medium-energy chemical process with a reasonable decrease in enthalpy and Gibbs energy, high values of equilibrium constants and a low specific chlorination heat. This process also requires external heating of the reactive mixture.

2. The reaction of chlorination using dehydrated borax mixed with graphite at 500-900°C occurs in accordance with the following reaction equation:

$$2Na_2B_4O_{7s,l} + 7C_{(graphite)} + 14Cl_{2g} = 8BCl_{3g} + 7CO_{2g} + 4NaCl_{s,l}. \quad (17)$$

Chlorination results in boron trichloride, carbon dioxide and NaCl.

The calculation of thermodynamic functions of BCl_3 synthesis in the reaction (17) is presented in Table 4.

TABLE 4

Functions of synthesis of BCl_3 in the reaction (17) at temperatures of 773÷1173 K

Function ΔF^o_T	Temperature T, K					$\Delta F^o_T = A + B \cdot T^*$		
	773	873	973	1073	1173	A	$B \cdot 10^3$	$\pm\delta$
$-\Delta H^o_T$, kJ/mol Cl_2	75.06	75.48	76.00	133.95	112.69	-70.715	-5.51	0.0758
ΔS^o_T, J/(K·mol Cl_2)	41.16	40.64	40.08	-48.10	-17.55	45.539	-5.63	0.0246
$-\Delta G^o_T$, kJ/mol Cl_2	106.88	110.97	115.01	82.32	92.11	-75.954	-40.07	0.0529
K_e	$1 \cdot 10^{101}$	$9 \cdot 10^{92}$	$3 \cdot 10^{86}$	$1 \cdot 10^{56}$	$3 \cdot 10^{57}$	–	–	–
$\Delta H^o_{уд}$, MJ/kg Cl_2	1.0587	1.0646	1.0719	1.8893	1.5894	1.0350	0.0337	0.0073

*Up to the temperature of 1015 K – the temperature of melting of borax $Na_2B_4O_7$.

We can see that synthesis of boron trichloride by chlorination of the borax-carbon mixture is also a medium-energy chemical process with a reasonable decrease of enthalpy and Gibbs energy, high values of equilibrium constants and a low specific chlorination heat. This process also requires external heating of the reactive mixture.

The equation of reaction of borax with chlorine mixed with disulfur vapor at 500-900ºC is as follows:

$$4Na_2B_4O_{7s,l} + 7S_{2g} + 28Cl_{2g} = 16BCl_{3g} + 14SO_{2g} + 8NaCl_{s,l}. \quad (18)$$

Boron trichloride, sulfur dioxide and sodium chloride are formed during chlorination.

The calculation of thermodynamic functions of BCl_3 synthesis in the reaction (18) is presented in Table 5.

TABLE 5.

Functions of synthesis of BCl_3 in the reaction (18) at temperatures of 773÷1173 K

Function ΔF^{o}_{T}	Temperature T, K					$\Delta F^{o}_{T} = A + B \cdot T^{*}$		
	773	873	973	1073	1173	A	$B \cdot 10^3$	±δ
$-\Delta H^{o}_{T}$, kJ/mol Cl_2	61.04	61.39	61.76	119.52	98.04	-57.999	-3.897	0.0299
ΔS^{o}_{T}, J/(K·mol Cl_2)	-1.35	-1.78	-2.18	-90.18	-59.42	1.738	-4.015	0.0088
$-\Delta G^{o}_{T}$, kJ/mol Cl_2	60.00	59.84	59.64	22.74	28.33	-61.715	2.173	0.0374
K_e	$3 \cdot 10^{113}$	$2 \cdot 10^{100}$	$4 \cdot 10^{89}$	$1 \cdot 10^{31}$	$2 \cdot 10^{35}$	–	–	–
$\Delta H^{o}_{уд}$, MJ/kg Cl_2	0.8609	0.8659	0.8711	1.6858	1.3828	0.8431	0.0256	0.0060

*Up to the temperature of 1015 K – the temperature of melting of borax $Na_2B_4O_7$.

As in the previous cases, synthesis of boron trichloride by chlorinating borax with the chlorine and disulfur vapor mixture is a medium-energy chemical process with a reasonable decrease in enthalpy and Gibbs energy, high values of equilibrium constants and a low specific chlorination heat. It requires external heating of the reaction mixture.

Considering that boron oxide is produced from boric acid and boric acid is produced from borax, the use of borax as the feed for the production of boron trichloride seems to be rather feasible. Sodium chloride, which is produced as a by-product of the synthesis reaction is not a waste product since it is the production environment of the salt chlorinator.

3. Boron carbide is chlorinated under the same conditions, according to the following reaction equation:

$$B_4C_s + 6Cl_{2g} = 4BCl_{3g} + C_s. \quad (19)$$

Chlorination results in boron trichloride and carbon.

The calculation of thermodynamic functions of BCl_3 synthesis in the reaction (19) is presented in Table 6.

TABLE 6

Functions of synthesis of BCl_3 in the reaction (19) at temperatures of 773÷1173 K

Function ΔF^o_T	Temperature T, K					$\Delta F^o_T = A + B \cdot T$		
	773	873	973	1073	1173	A	$B \cdot 10^3$	±δ
$-\Delta H^o_T$, kJ/mol Cl_2	256.64	256.52	256.41	256.32	256.26	-257.37	0.962	0.0173
ΔS^o_T, J/(K·mol Cl_2)	-33.07	-32.92	-32.80	-32.72	-32.66	-33.827	1.023	0.0277
$-\Delta G^o_T$, kJ/mol Cl_2	231.07	227.77	224.49	221.21	217.95	-256.44	32.819	0.0096
K_e	$5 \cdot 10^{93}$	$6 \cdot 10^{81}$	$2 \cdot 10^{72}$	$4 \cdot 10^{64}$	$2 \cdot 10^{58}$	–	–	–
$\Delta H^o_{уд}$, MJ/kg Cl_2	3.6197	3.6181	3.6165	3.6152	3.6144	3.6299	-0.0135	0.0026

Unlike the options discussed above, synthesis of boron trichloride from boron carbide is a high-energy chemical process featuring a high decrease of enthalpy. Both Gibbs energy, equilibrium constants and the specific chlorination heat are high. After the initiation of the process, it can be maintained without external heating.

4. Chlorination of the mixture of ferroboron and sodium chloride at 500-900ºC will run in accordance with the following equation:

$$FeB_s + NaCl_{s,l} + 3Cl_{2g} = BCl_{3g} + NaFeCl_{4l}. \quad (20)$$

Chlorination produces boron trichloride and sodium tetrachloroferrate (III), a non-volatile complex able to maintain ferric trichloride solution under temperatures of up to 1000ºC.

Due to low energy of FeB alloy formation as compared to the energy of its chlorination, hereinafter ferroboron was regarded as the mixture of Fe + B.

The calculation of thermodynamic functions of BCl_3 synthesis in the reaction (20) is presented in Table 7.

TABLE 7

Functions of synthesis of BCl_3 in the reaction (20) at temperatures of 773÷1173 K

Function ΔF^o_T	Temperature T, K					$\Delta F^o_T = A + B \cdot T^*$		
	773	873	973	1073	1173	A	$B \cdot 10^3$	±δ
$-\Delta H^o_T$, kJ/mol Cl_2	234.98	233.56	232.22	230.98	256.60	-244.83	12.859	0.0879
ΔS^o_T, J/(K·mol Cl_2)	-21.74	-20.00	-18.56	-17.34	-53.73	-31.923	13.491	0.2232
$-\Delta G^o_T$, kJ/mol Cl_2	218.17	216.09	214.16	212.37	193.57	-232.49	18.691	0.1255
K_e	$2 \cdot 10^{44}$	$6 \cdot 10^{38}$	$3 \cdot 10^{34}$	$1 \cdot 10^{31}$	$7 \cdot 10^{25}$	–	–	–
$\Delta H^o_{уд}$, MJ/kg Cl_2	3.3142	3.2942	3.2753	3.2578	3.6192	3.4251	-0.1492	0.0024

*Up to the temperature of 1074 K, the melting temperature of sodium chloride NaCl.

Chlorination of ferroboron with chlorine is a high-energy chemical process featuring a high enthalpy decrease and Gibbs energy, high values of equilibrium constants and specific

chlorination heat. As in the previous case, it requires heating of the reaction mixture only at the initial stage of the process.

Despite the relatively low content of boron, ferroboron is the most inexpensive feed containing elemental boron which is available in bulk quantities. Much like the bulk production of silicon tetrachloride by chlorinating ferrosilicon [1, pp. 192-204], chlorination of ferroboron may become the main industrial method of boron trichloride production. JSC SMW owns the technique of molten ferrous alloy chlorination, e.g., of ferroniobium [22]. In order to bind iron and aluminum during ferroalloy chlorination, patent [23] recommends to add industrial salt in molten low-volatile chloride complexes in the amount of 1.2 kg per 1 kg of Fe and 2.2 kg/kg of Al. A drawback of this synthesis method includes high waste content in the form of molten salt containing ferric chloride.

5. The process of chlorination of magnesiothermic boron or magnesium boride at 500-900°C may be represented by the following reaction:

$$MgB_{18s} + 28Cl_{2g} = 18BCl_{3g} + MgCl_{2s,\,l}. \qquad (21)$$

Chlorination results in boron trichloride and low-volatile magnesium bichloride.

Due to low energy of MgB_{18} alloy formation as compared to the energy of its chlorination, hereinafter magnesium boride was regarded as the mixture of Fe + B.

The calculation of thermodynamic functions of BCl_3 synthesis in the reaction (21) is presented in Table 8.

TABLE 8

Functions of synthesis of BCl_3 in the reaction (21) at temperatures of 773÷1173 K

Function ΔF^{o}_{T}	Temperature T, K					$\Delta F^{o}_{T} = A + B \cdot T^{*}$		
	773	873	973	1073	1173	A	$B \cdot 10^{3}$	±δ
$-\Delta H^{o}_{T}$, kJ/mol Cl_2	281.47	281.38	282.36	278.34	278.30	-279.23	0.812	0.0264
ΔS^{o}_{T}, J/(K·mol Cl_2)	-37.05	-36.93	-38.53	-32.64	-32.61	-33.603	0.879	0.0360
$-\Delta G^{o}_{T}$, kJ/mol Cl_2	252.83	249.13	244.86	243.31	240.05	-278.44	32.730	0.0082
K_e	$2 \cdot 10^{478}$	$2 \cdot 10^{417}$	$1 \cdot 10^{368}$	$4 \cdot 10^{331}$	$2 \cdot 10^{299}$	–	–	–
$\Delta H^{o}_{уд}$, MJ/kg Cl_2	3.9299	3.9281	3.9268	3.9258	3.9253	3.9383	-0.0115	0.0004

*After exceeding the temperature of 987 K, the melting temperature of magnesium bichloride $MgCl_2$.

The data of Table 8 indicates that in terms of enthalpy and Gibbs energy decrease, equilibrium constant and specific reaction heat the process of chlorination of magnesiothermic boron is the most effective of all the previously described processes. Due to its reactivity, magnesium metal, a substance related to boron in the feed, would even improve all the thermodynamic properties of the chlorination process, besides, it forms a low-volatile chloride $MgCl_2$ which causes virtually no contamination of the volatile chlorination product, BCl_3. Due to production process specifics of JSC SMW, the resultant magnesium bichloride may be reused as a cycling feed in the electrolytic production of magnesium. This would make it possible to set up a low-waste production of boron trichloride.

For ease of comparison, the Gibbs energy changes of the chlorination reactions of various boron-containing materials are grouped in Fig. 1.

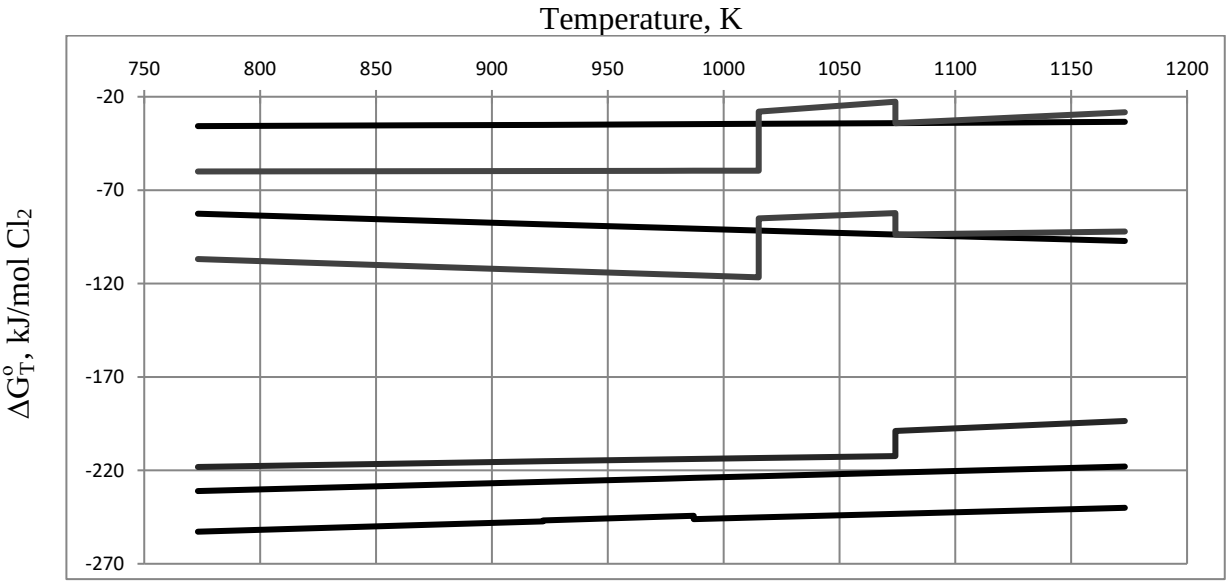

FIG. 1. The dependence of $\Delta G^o_T = f(T)$ *for chlorination reaction 15-21 ranged by* ΔG^o_T *decrease:*

$4B_2O_{3l} + 3S_{2g} + 12Cl_{2g} = 8BCl_{3g} + 6SO_{2g}$; (16)

$4Na_2B_4O_{7s,l} + 7S_2 + 28Cl_{2g} = 16BCl_{3g} + 14SO_{2g} + 8NaCl_{s,l}$; (18)

$2B_2O_{3l} + 3C_{(graphite)} + 6Cl_{2g} = 4BCl_{3g} + 3CO_{2g}$; (15)

$2Na_2B_4O_{7s,l} + 7C_{(graphite)} + 14Cl_{2g} = 8BCl_{3g} + 7CO_{2g} + 4NaCl_{s,l}$; (17)

$FeB_s + NaCl_{s,l} + 3Cl_{2g} = BCl_{3g} + NaFeCl_{4l}$; (20)

$B_4C_s + 6Cl_{2g} = 4BCl_{3g} + C_s$; (19)

$MgB_{18s} + 28Cl_{2g} = 18BCl_{3g} + MgCl_{2s,l}$. (21)

Optimal conditions of heat and mass transfer and the highest specific speed of chlorination processes are achieved by chlorination in melt. This engineering solution is widely used at JSC SMW in chlorination of various raw materials. It should not be difficult to adapt the process for the production of boron trichloride. The process may be carried out in compact chlorinators featuring smooth adjustment of process speed and temperature by way of varying the rate at which chlorine is fed into the station under the molten layer. Chlorination of magnesiothermic boron would make it possible to set up an autothermal process which would require no external heat supply even in case of low-performance chlorinators. In the absence of elements forming other low-boiling chlorides in the feed, vapors exiting the chlorinator could yield boron trichloride content of almost 100%. Otherwise, produced boron trichloride following its condensation may be purified by rectification at atmospheric pressure and the temperature of +12÷15ºC.

Hardware arrangements options of the chlorination process.

As a rule, industrial chlorinators have the form of devices with a steel shell lined from the inside with a refractory and chlorination-resistant material -- kaolin or silica bricks, graphite etc. Chlorinators allow to carry out chlorination within a pile of furnace mix pellets -- a compressed mixture of the chlorinated material with a reducer or without one, placed within the fluidized bed of furnace mix powder having a specific coarseness or suspended within a melt of crushed material.

Chlorination within the pile of furnace mix pellets has its drawbacks: low performance due to countercurrent diffusion of reagents and reaction products within pellets, the need to manufacture the pellets beforehand (additional processing stages include mixing, pressing (pelletizing), drying and cooking of pellets), inconsistency of temperatures in various areas of the pellet heap and the need to clean the chlorinator of the non-chlorinated residuals (tails).

Chlorination in fluidized bed requires a furnace mix of components with a certain coarseness to form the fluidized medium; as a rule, the volume of gases after the chlorination is lower than the volume of supplied chlorine. This calls for the application of a carrier gas (nitrogen) which reduces the concentration of the reagent and reaction product. Boiling of the powder is disrupted when melting chlorides are formed. High dust loss (5 to 10% of the initial load) requires to install dust collectors that provide furnace mix recovery.

Chlorination in melt is free from a number of drawbacks that are inherent to chlorination in a heap or in fluidized bed -- optimal conditions of heat and mass exchange allow to achieve the highest specific capacity of chlorination processes. In order to ensure effective chlorination of magnesium and rare metal feed, Solikamsk Magnesium Works uses molten-substance chlorinators only.

The experimental shop of JSC SMW features a semi-production experimental plant designed for the production of niobium and tantalum pentachlorides by way of chlorination within molten alloys of these metals, particularly, of ferroniobium (over 6 tons of the alloy has been chlorinated). Replacing the scraper type condenser [23] used for solid low-volatile pentachlorides with a liquid $BCl3_3$ condenser cooled with brine to –30÷40°C would make it possible to produce the product in quantities amounting to hundreds of kilograms per day in the process of chlorination of boron-rich metal materials -- ferroboron (with the addition of salt) or, better yet, of magnesiothermic boron with low magnesium content (see. Fig. 2).

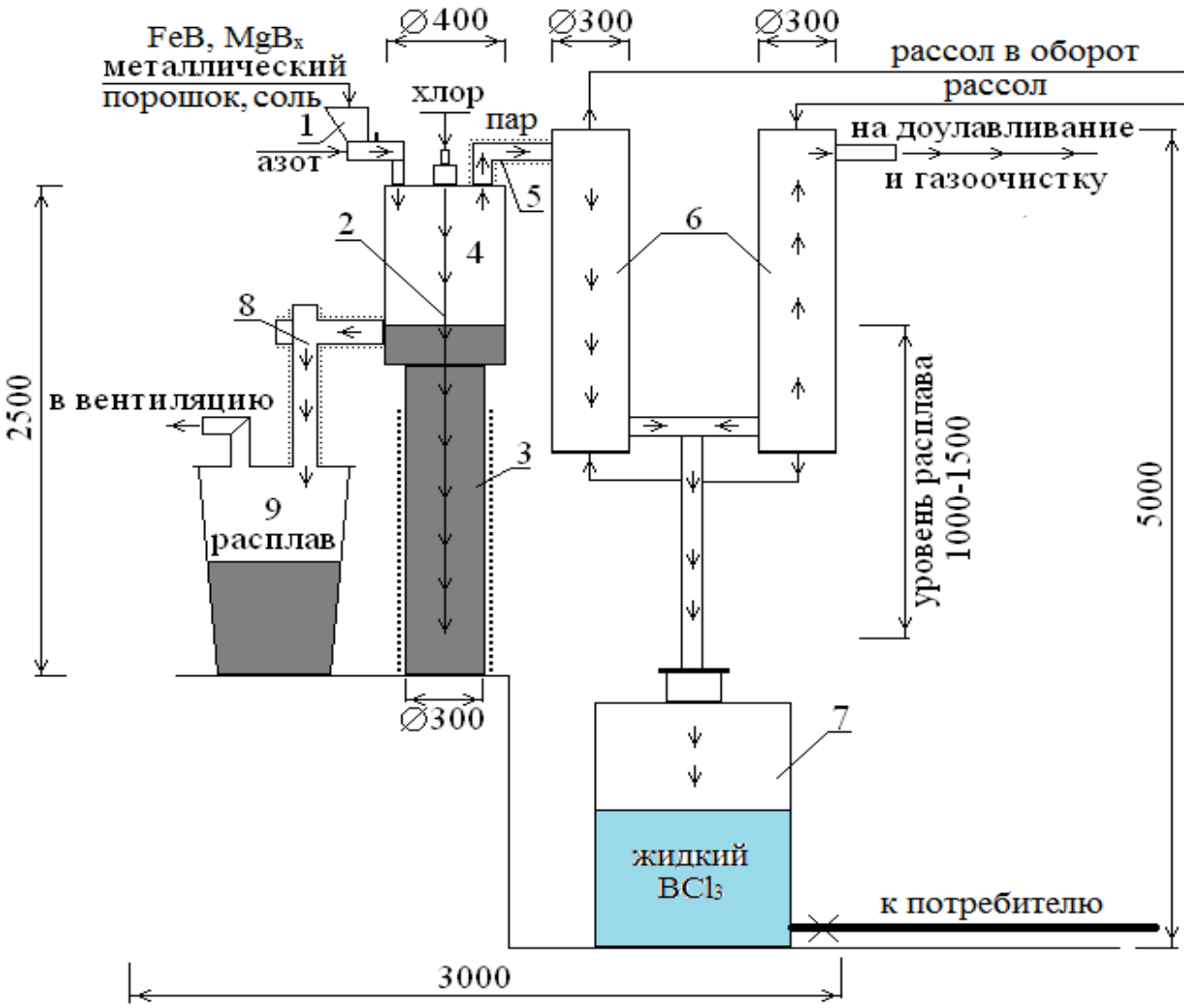

FIG 2. The plant for melt-based chlorination of metal boron-containing materials: 1 – screw feeder; 2 – graphite chlorine feeder; 3 – melting area of the chlorinator with a water cooling loop; 4 – separation chamber; 5 – $BCl3_3$ vapor exhaust pipe; 6 – shell and tube condenser/exchangers; 7 – chloride sump;
8 – melt draining unit; 9 – melt pan.

Fig. 2 also shows principal overall dimensions of the plant.

Conclusions

Theoretical analysis and simulation of the boron trichloride synthesis process using different raw materials allows us to conclude that elemental boron produced by magnesiothermic reduction method has the highest free energy and the highest specific chlorination heat of all the analyzed boron-containing materials. This process of chlorination has a number of advantages as compared to the chlorination of other types of boron-containing raw materials, and may be recommended for practical application.

References

1. Furman A. A. Inorganic chlorides: chemistry and technology – M.: Chemistry, 1980. – 416 p.

2. Sevryugova N. N., Uvarov O. V., Zhavoronkov N. M. in volumes: Boron. The proceedings of the symposium dedicated to chemistry of boron and its compounds – M.: Goshimizdat, 1958. – p. 30.

3. Aloyev A. S., Kaminskiy V. A., Kudziyev A.G., Matreveli R. Sh. Determination of separation factors of boron isotopes during the distillation of BCl3 within the temperature range of 278 to 438 K // Atomic Energy, 1980, V. 49, issue 2, p. 98–101.

4. S. P. Andriyets, A. A. Guschin, A. L. Kalashnikov et al. The development and testing of a pilot plant for boron isotope separation by rectification of BCl3 -- Perspektivnye Materialy, 2010, No. 8, p. 193 – 198.

5. V. D. Risovanyi, A. V. Zakharov, E. V. Klotchkov, T. M. Guseva. Boron in the nuclear industry -- 2nd edition (revised and extended) -- Dimitrovgrad: RIAR JSC, 2011 -- p. 668

6. Baranov V. Yu. Isotopes: properties, production and application. – M.: IsdAT 2000, - 704 p.

7. Andreev B. M., Zelvenskiy Ya.D., Katalnikov S.G. Separation of stable isotope using physicochemical methods. – M.: Energoatomizdat. 1982. – 206 p.

8. The market for boric acid in Russia in 2018 Figures and forecasts. Tebiz Group Analytics Company. – 51 p.

9. Tkachyev K.V., Plyshevskiy Yu.S. The technology of inorganic boron compounds. – Leningrad: KHIMIYA, the Leningrad Division. 1983. – 208 p.

10. Akhmetov T.G., Porfirieva T.G., Gaisin L.G. et al. Chemical engineering of inorganic substances: in 2 volumes. Volume 1. Learning guide.// Eds T.G. Akhmetova – M.: Vysshaya Shkola, 2002. – 688 p.

11. Pozin M.E. Mineral salts engineering (fertilizers, pesticides, industrial salts, oxides and acids). Pt. 1. 4th edition (revised) – L.: Chemistry, 1974. – 792 p.

12. Inorganic Materials Encyclopedia: in 2 volumes. V. 1, 2.// ed.-in-chief I.M. Fedorchenko – Kiev: ed.-in-chief of Ukrainian Soviet Encyclopedia, 1977. – pp. 840, 816

13. Lidin R.A., Andreeva L.L., Molochko V.A. Inorganic substance constants.// Reference book eds. R.A. Lidin 3rd reprint edition. – M.: Drofa, 2008. – 685 p.

14. Samsonov G.V., Perminov V.P. Magnesiothermy. – M.: Metal Engineering, 1971. – 176 p.

15. Karapetyants M. H. Chemical thermodynamics. 3rd edition (revised and extended) -- M.: Chemistry, 1975. – 584 p.

16. Kubasjevskiy O., Alcock K.B. Metallurgic Thermochemistry.// translated from English -- M.: Metal Engineering, 1982. – 392 p.

17. Morachevskiy A.G., Sladkov I.B. Physical and chemical properties of molecular inorganic compounds (experimental data and estimation procedures): Reference edition. – L.: Chemistry, 1987. – 192 p.

18. Kireev V. A. Practical procedures of estimation of chemical reaction thermodynamics – M.: Chemistry, 1970. – 520 p.

19. Glukhov I.A., Shalukhina L.M.// DAN Tadjik SSR, 1960, vol. III, No. 2; 1961, vol. IV, No. 1; 1961, vol. IV, No. 3; 1961, vol. IV, No. 4.

20. Rozebuum H., Aten A.// Proc. Akad. Amsterdam, 1904, v. 6, p. 559.

21. Morozov I.S. Application of chlorine in the metallurgy of rare and nonferrous metals: Basic physics and chemistry. – M.: Nauka, 1966. – 256 p.

22. Tsurika A.A. The estimation of basic physical and chemical processes and the development of the process of chlorination of man-made Nb, Ta and Ti-containing metal materials in chloride melts: Thesis paper of Candidate of Science – M.-Solikamsk: MITHT; JSC SMW, 2008. – 125 p.

23. A procedure of chlorination of polymetallic niodium- and tantal-contaning feed, and the apparatus for the implementation of the procedure./ Drobot D.V., Detkov P.G., Tsurika A.A. Chub A.V.// Rus. Pat. No. 2331680, IPC C22B 34/24, C22B 1/08. A.c. 2006117701. Subm. 24.05.06. Publ. 20.08.08.

THE PROSPECTS OF THE ELECTROMAGNETIC METHOD OF ISOTOPE SEPARATION AND POTENTIAL WAYS OF ITS MODERNIZATION

N.R. Gall[1], L.N. Gall[2], A.S. Berdnikov[2], A.A. Semyonov[3], A.V. Lizunov[3], A.M. Safiulina [3]
[1]Physics and Engineering Institute named after A. F. Ioffe of RAS, Saint Petersburg
[2]Institute for Analytical Instrumentation of RAS, Saint Petersburg
[3] SC "A.A. Bochvar High-Technology Research Institute of Inorganic Materials", Moscow

The current state and prospects of the electromagnetic method of isotope separation (EMS) which has no alternative in relation to certain chemical elements. The most important isotopes produced using the electromagnetic method are described. The reasons why EMS has mostly lost its industrial value are discussed. A conceptually new approach to the hardware implementation of the EMS method is described, and its considerable advantages over the available ways of implementation are discussed.

Keywords: isotopes, isotope separation, electromagnetic method of isotope separation, electromagnetic separation, ion beam, ion-optical arrangement, mass separator, space charge.

Introduction

Electromagnetic separation holds the place among the methods of isotope separation which is both historically and practically important [1]. Nevertheless, the application of this method is substantially impeded by both its engineering complexity, much higher product cost [2] and lower capacity as compared with other isotope separation methods [3-4] achieved within the concept of engineering implementation of the method available today. Consequently, electromagnetic separation (EMS) is only applied today in cases when it is not practical to employ physicochemical or gas-centrifugal methods that are much cost-effective and productive than the electromagnetic method and, besides, enjoy the required infrastructure. Whereas the development of EMS was initially driven by the atomic project, today it could be said that the isotope separation method does not find much use in either the atomic defense complex or the atomic energy industry. The narrow tasks it is employed in are related to fundamental scientific research and the production of radiopharmaceuticals. These do not require high production capacities and the product cost is not a constraint. Low demand for EMS has led to the stagnation of its development with regard to isotope separation which we witness today: after the 1970s, no new engineering solutions in the processes of electromagnetic isotope separation have been developed [5, 6]. Nevertheless, EMS has an undeniable advantage over all the current separation technologies as it makes it possible to both separate and accumulate all the isotopes of the separated element. If an engineering solution could be found that would make EMS more productive and cost-effective, new areas of its application in isotope separation would certainly crop up, including applications in the atomic energy industry.

This article is an overview of spheres of isotope separation where electromagnetic isotope separation is used presently. It also discusses the prospects of EMS application and possible options for the development of novel, more powerful and cost-efficient plants for this type of separation based on current advances in charged particle optics and electrophysical installations.

The objectives of isotope separation solved by using the electromagnetic method

During the last 70 years, the major portion of the known natural isotopes of the chemical elements throughout the periodical table have been obtained for fundamental scientific research purposes using electromagnetic separation. This was driven, in particular, by the already mentioned unparalleled advantage of electromagnetic separation over any other methods, that is, the ability to produce all the isotopes of an element simultaneously, in a single separation cycle with a high degree of purity. Since the need for medical and other applications in pure isotopes vary widely, we shall consider only the elements with isotopes are presently produced by the EMS method, as well as those with isotopes that could be advisably produced by EMS separation in the future [5-6].

The lightest of the elements with isotopes, which are presently serially produced using electromagnetic separation is potassium [6]. The stable isotope ^{41}K (6.73% in the natural mixture) and the radioactive isotope ^{40}K (0.012% in the natural mixture) are important ingredients of agrochemical research. These are separated from the lightest of the naturally occurring isotope of potassium ^{39}K. In this case, it is the ballast base (93.258%).

Isotopes of calcium are also separated using the electromagnetic method. Naturally, this chemical element is represented by a mix of six isotopes: ^{40}Ca which accounts for over 96.9% of the mixture and rather rare isotopes 42, 43, 44, 46 and 48. Isotopes of calcium have a number of applications. Isotopes ^{43}Ca and ^{44}Ca with contents in the natural mixture of 0.135 and 2.086 %, respectively, are used to produce the ^{43}K radiopharmaceutical. The heaviest of the stable calcium isotopes, ^{48}Ca, which accounts for 0.187% of the mixture is used today in fundamental scientific physics research.

The slightly radioactive natural isotope ^{87}Rb (its content is 27.83% in the natural mixture with ^{85}Rb) is used in geophysical studies and, besides, in the form of vapors - in high-sensitivity magnetic field sensors that operate on the nuclear resonance principle, as well as in atomic resonance frequency references and atomic clocks [6].

Isotope strontium-84 which amounts to only 0.56% of the natural mixture with other, heavier isotopes with the weights of 86, 87 and 88, is used for the production of ^{85}Sr radiopharmaceutical used in the diagnostics of skeletal disorders [6].

Natural zirconium, which is a mix of five isotopes having the weights of 90, 91, 92, 94 and 96 accumulates radioactive isotopes ^{93}Zr, ^{95}Zr and ^{97}Zr when used in nuclear reactors [7]. Whereas the two heavier radionuclides are short-lived and could be disposed of by a few years of curing, ^{93}Zr has the half-life of 1.5 million years which prevents irradiated zirconium from being reused. Isotopes of zirconium may be separated using EMS [8]. Development of a cheap and productive method of ^{93}Zr isotope separation from the mixture with other isotopes would promote the reuse of reactor zirconium which today has to be permanently disposed.

Palladium which is classified as a platinum group metal is in much demand in various fields of research and development. As engineering demands in it grow, it becomes increasingly sought-after. It should be also noted that stable isotopes of the element are accumulated in considerable quantities in spent nuclear fuel (SNF) of nuclear power plants [9, 10]. Whereas WWER type reactor fuel may contain more than one kilogram per one ton of SNF, spent nuclear fuel of fast nuclear reactors may contain up to 5 kg of palladium per one ton. The idea to separate palladium contained in SNF is very attractive in itself. Unfortunately, such palladium also contains the beta-radioactive isotope ^{107}Pd whose half-life is $6{,}5 \cdot 10^6$ years which accounts for 14 to 16% depending on the burn-up range of SNF and its curing time. If an economically acceptable method of ^{107}Pd removal could be developed, all other isotopes of palladium may find use. Due to the complexity of handling volatile compounds of palladium, EMS is an advantageous and technically feasible method of separating its isotopes today.

Rare earth metal (REM) isotopes are widely used for various research, engineering and medical applications. There are prospects of large-scale application that are impeded, however, by the engineering complexity of their production. REM do not form volatile compounds, accordingly, there are no viable alternatives to the expensive EM separation of their isotopes today. Examples of certain REM isotopes that are most noteworthy in terms of their practical application [6] are discussed below.

Isotopes ^{151}Eu and ^{152}Gd are used for the production of radionuclide ^{153}Gd which has certain technical applications.

Isotopes of neodymium (^{148}Nd) and samarium (^{154}Sm) are used in geophysical studies as the reference when determining the age of rocks [6].

Gadolinium and erbium have been used for over 20 years as burnable absorbers that enable to improve the effectiveness of nuclear fuel at NPP significantly [11-13]. Gadolinium is also used as part of nuclear fuel for WWER type reactors [11, 12] whereas erbium is used as part of RBMK channel type boiling water reactor fuel. As an example, adding 0.6% erbium in RBMK type reactor fuel reduces void coefficient of reactivity and energy release variance considerably, reduces the number of fuel assembly failures and, besides that, improves fuel burn-up and reduces consumption of fuel assemblies. Use of highly enriched isotopes of gadolinium ^{157}Gd, (15.65% in the natural mixture) and erbium ^{167}Er (content in the natural mix - 22.93%) may improve their efficiency in burnable absorbers. Unfortunately, high cost and low output of modern generators that produce these isotopes restraints their use.

Lutetium-177 is a potentially attractive radioisotope which is widely used in treatment of oncology diseases. The isotope is produced by irradiation of ^{176}Yb (12.76% in the natural mixture) or ^{176}Lu (2.59 %) in a reactor. The first method produces a carrier-free target radioisotope. This makes it possible to approximate to the level of theoretically possible specific activity of ^{177}Lu following the stage of radio chemical reprocessing of the irradiated target. In the second case, ^{177}Lu is contaminated with other lutetium isotopes (primarily with the radioactive isomer ^{177m}Lu), which has an adverse impact on the quality of radiopharmaceuticals based on it. In both cases, the electromagnetic mass separation method is used to improve the yield when irradiating in a reactor for the purpose of initial enrichment in terms of the initial isotope (^{176}Yb or ^{176}Lu). [14, 15]. Isotope ^{168}Yb, which naturally

accounts for 0.13% of the total ytterbium isotope mix, also finds certain applications. It is used to produce the radionuclide ^{169}Yb which, in its turn, is used both in the medical industry and in gamma-ray spectroscopy.

The EM separation method is also used to produce isotope thallium ^{203}Tl which is the initial material for cyclotron production of the radiopharmaceutical ^{201}Tl. Electromagnetic separation is combined with other separation techniques in the production of isotopes of mercury and zinc [6].

More recently, researchers conducting biophysical studies have shown considerable interest in the role of isotope composition of trace elements that form biological regulatory molecules. It was demonstrated, for example, that replacing the naturally occurring magnesium with pure ^{25}Mg boosts the efficiency of both regulatory molecules responsible for anaerobic respiration [16] and respective medicinal preparations. It was also determined that isotope compositions of iron and zinc in human body depend on the person's gender status and race [17]. Scientific knowledge of the role of isotopes in living systems is currently just being formulated, however, appropriate growth in demand is expected for respective isotope products that may be produced using the EM separation method.

The history of the electromagnetic isotope separation method

The history of the electromagnetic isotope separation technique is presented in sufficient details in [2, 6]. These documents also discuss physical concepts of the method and the basics of developing the relevant equipment. Besides that, quantitative characteristics that determine the operation of EMS electrophysical devices are described in detail. The EMS method is based on the same concepts as mass spectrometry: atoms of the element subject to isotope separation are transformed into ions, accelerated to a certain energy, which is constant for all the ions, and are sent through a transverse uniform (or, in some rare cases, non-uniform) magnetic field. The ions are spatially separated within the field depending on their mass, and are collected at special accumulators (pockets) with every isotope in a separate pocket. Theoretically, the separation ration may be quite high, and is defined by ion-optical parameters of the mass-separator and characteristics of the beam created by the source of ions. The main advantage of this method over all the other procedures of isotope separation is the principal possibility of separation of all the isotopes in a single cycle, and the resulting purity of isotopes of almost 100%. The main fundamental limitation of this method of isotope separation is its low performance.

Performance of the separation plant is determined, above all else, by ion current that may be, firstly, extracted from a source of ions, and secondly, passed through the separator [2]. This second part of the process proves to be the "bottleneck" of the procedure since the space charge of the ion beam at high densities of current starts to play the key role, which leads to non-observance of ion-optical conditions needed to focus it [18]. That being said, the capacity of the plant is directly related to ion current which is split in the separator. This current must be at least 1 mA to achieve any reasonable performance. Indeed, at ion current of

1 mA, all the accumulator of the separator receive $1{,}6 \cdot 10^{17}$ ions, or $2{,}5 \cdot 10^{-7}$ mol of particles per second. This makes it possible to accumulate at all of the accumulators $\sim 2 \cdot 10^{-2}$ mol. In case of uranium, this amounts to 5 g. However, if the initial substance is naturally-occurring uranium then fissile isotope ^{235}U accounts only for 0.035 g thus producing only 13 grams per year. Naturally, major efforts of developers of EMS and devices that implement the method were focused on increasing the current of the separator. This issue will be discussed in more detail in the following chapter.

Historically, two stages may be singled out in the development of the EMS method. At the first stage, uniform sectoral magnetic fields were used. Mass dispersion of ions within these fields was directly proportional to their turning radius within the magnetic field. The problem of space charge and the simultaneous increase of linear distance between the accumulators was solved by increasing ion energies to tens of thousands volts with simultaneous respective increase of dimensions of the magnetic field. This ion-optical solution was implemented in the form of very large electrophysical installations with a turning radius of ions being a number of meters. To support such a current, considerable magnetizing currents were required with respective power of tens of kilowatts [2]. Despite the huge energy consumption, however, the resulting grade of purity of isotope separation achieved by the separators was insufficient, as was their performance.

At the second stage, in 1960s, it was theoretically proven that the use of magnetic fields non-homogeneous in terms of radius would allow to increase their dispersion significantly, and thus increase the distance between the accumulators without the need to increase the magnet itself. Nevertheless, the development of inhomogeneous magnetic field separators that were much more compact than separators of the first generation neither resulted in the reduction of energy consumption per 1 unit of separation action (EPP, SWU) [19], nor allowed to achieve any fundamental success in attaining isotope separation purity. These setbacks may, to a degree, be explained by incomplete theory of charged particle optics and the physics of ion beam transportation, as well as by certain limitations in the field of vacuum technologies.

Today, Russian enterprise FGUE Kombinat Elekrohimpribor located in Lesnoy of the Sverdlovsk Region is one of the largest isotope producers which uses the electromagnetic separation principles. Historically, one of the aims of the enterprise was production of uranium-235 for atomic charges. Following the development of gaseous-diffusion and gas-centrifugal methods of isotope separation, the powerful separation facilities of FGUE Kombinat Elekrohimpribor have become unnecessary. Since that time, the facilities have been mainly used to produce stable isotopes of a variety of chemical elements. Certain similar or more advanced EMS installations that use the same theory operate today in France, Israel and the USA [5, 6].

The problems of the electromagnetic isotope separation method

In order to develop not just operational but also effective separation installation, a number of complex theoretical and engineering problems had to be solved. These problems include the following: developing methods that ensure element ionization and ion extraction

that would be almost 100% efficient, and devices that implement these methods; developing an ion-optical arrangement and the design of a separator able to carry the highest ion current possible; developing a cooling system for isotope collection pockets that heat up due to both kinetic energy of incoming ions and due to ion radioactivity; and solving all the engineering problems associated with the objective of creating highly stable power and vacuum pumping systems, ensuring regular input of substances and replacement of accumulating pockets [2].

The task of creating high-power plasma-based ion sources with high extraction efficiency was not easy, but by early 1960s it was solved by employing the plasma arc ionization method. An essential problem of passing considerable ion currents through the mass separator remained, however [6]. To solve this problems, developers of EMS systems from different countries used the traditional approach: by accelerating ions to highest energies possible, increasing the spatial section of ion beams in order to reduce the charge-space effect, and using the movement of the ion beam in low vacuum to gain advantage of the self-compensation effect of the spatial charge due to slow electrons forming during the ionization of residual gas molecules with ions of the beam. Unfortunately, despite theoretical attractiveness of these directions, their practical implementation has led to considerable problems that, apparently preordained the limited use of electromagnetic isotope separation by modern-day technologies.

The use of high energies called for large magnetic poles (1.5 to 3 m). The aspiration to make the beam section as large as possible resulted in the increase of the distance between the poles which in a number of devices reached 20 to 30 cm, whereas in a conventional analytical mass spectrometer this distance is usually about 6 to 10 mm. In order to enable magnetic fields sufficient for effective rotation of ions with such clearances and such areas (in practice, these did not exceed 0.3 to 0.4 T [6]), huge magnetomotive coils and systems had to be built providing them with highly stable power (with currents numbering into hundreds of amperes and capacitances of hundreds of kilowatts). The transition to non-homogenous magnetic fields made it possible to somewhat downscale the dimensions of EMS electromagnets, but did not alter the situation essentially.

Considerable progress of the ion-optical theory of magnetic mass analyzer achieved over the span of 70 years since the development of the above mass separators now enables to remove all the image aberrations that occurred in the previously developed mass separators and thus improve the degree of isotope separation. Certain studies in 1970s of peak “tails” occurring due to the diffusion of isotope ion beams at the residual gas [20] at the surface of pole tips of the magnet and at diaphragm slit edges that limit beams [21] also greatly facilitate the improvement of separation degree by preventing the influx of intensive isotope ions into the accumulator pockets of less intensive isotopes. An even more noteworthy breakthrough affecting mass separators is the introduction of certain elements of the transportation theory into the ion-optical theory which made it possible to evaluate the effect of the space charge and thus to adjust geometrical positions of ion beam focusing arms, i.e., to determine their location with higher precision. Incomplete theoretical knowledge in the field of ion optical theory available to designers of electromagnetic separation installations built in 1960s led to the emergence of inherently persistent effects that were alleviated only by increasing separator dimensions. The above effects of poor focus and dissipation existed even in the large

separators of the 1960s, and they limited both the maximum performance of installations and the achievable degree of separation [6].

The potential for the enhancement of the electromagnetic isotope separation method

Consistent demand for high-precision isotope analysis and the development of elemental analysis witnessed during the most recent decade have led to the emergence of novel ion-optical and engineering solutions and the development of static magnet mass analyzers that employ new ionization methods. These installations ensure high separation and isotope focus characteristics with high dynamic ranges of their content. Since the method of electromagnetic isotope separation is related to mass spectrometry, progress in the latter opens up new possibilities in the development of electromagnetic separators.

The new concept of mass spectrometer building which has been perfected in production and proven through practice is based on modern advancements of ion-optical theoretical knowledge of separation and focusing charged particle beams, new techniques of estimation and synthesis of magnetic fields with complex configuration, production technologies of strong permanent magnet (Sm-Co, Nd-Fe-B) and the Ms-platform technology of constructing electrophysical devices [22]. The Ms-platform solution involves assembly of ion-optical elements of the separator on a common base which is afterwards placed in a vacuum chamber (the chamber's only purpose is to ensure hard vacuum). Considering the characteristics of new ion-optical solutions, such a separator operating under the incoming ion current of 1 mA would feature relatively small dimensions and weight. These separator units may be arranged into a multiple channel system of arbitrary configuration - both universal, with a magnet radius which permits separation of any isotopes up to those of heavy elements, and special-purpose systems designed for one specific task. The substitution of electromagnets with permanent magnets in the design of EM separators makes the isotope separation process much less expensive since no electricity is required to generate the magnetic field.

In the context of low effect of space charge, ion-optical systems with double focus may be used which would lower ion energy to some kilovolts. This, in turn, would make the separator much lighter and smaller. The theory of non-uniform electrical and magnetic fields that are at the same time uniform according to Euler's equation developed by the academic school of Yu. K. Golikov and A.S. Berdnikov and presently researched, makes it possible to develop ion-optical arrangements with double focus and non-uniform magnetic fields of complex form. This results in further decrease of dimensions [23].

Let us discuss a possible example of implementation. The used system has a 120-degree magnet, the radius of 400 mm and a non-uniform field of a complex form, a cylindrical electrostatic accumulator and an aberration corrector. Each separator uses its own small-size plasma-based ion source. The distance between peaks within the mass region of 150 AMU is 3 to 3.5 mm, the abundance sensitivity (the degree of intensity of the isotope falling into an adjacent pocket) is 10^{-4}, the width of the crossover at the ion source discharge (this is similar to the slit in mass spectrometry) is 1 mm, the peak width at the separator discharge is 1.5 mm. Ion beam current is 10^{-4} A, the acceleration voltage is 4 kV. A calculation based on the Peirce representation [18, 25] adjusted for ion mass demonstrates that the consumed current is 5 to

10 times less than that at which space charge effects begin to manifest noticeably. Each of the separators is equipped with additional easily detachable pockets for capturing the flow of neutral atoms of the separated substance from the source. Vacuum in the chamber is supported at the level of $(5\text{-}7)\cdot10^{-6}$ torr during the operation of all sources.

The separators have the height of about 50 mm above the platform. Twenty separators may be installed in the common vacuum chamber. They have a shared magnetic system and a common system of electrostatic condensers. The chamber is equipped with two vacuum-proof doors for loading the material into the sources and removal/replacement of the accumulating pockets. The system is evacuated by three standard turbomolecular pumps of nominal diameter DU100 and a common vacuum booster pump. All the separators are supplied using a common power circuit and are controlled by one computer. The area required for the device in a laboratory or a shop is 3 sq. m. and its weight is about 150 to 200 kg. The device is designed for 24/7, year-round operation with brief stops for loading the working substance and removal of produced isotopes.

Economic indicators of isotope separation costs attainable by using the electromagnetic method

Let us discuss the engineering parameters that were described in the previous section. We shall analyze only the engineering portion of costs since the general economic portion is determined by organization of activities and is beyond the scope of this publication. From the engineering point of view, costs are subdivided into those related to capital expenditure amortization and those related to operation; in the estimation of the first part we shall disregard discounting and when estimating the second part we shall proceed from the assumption of constant current prices for resources.

The multi-channel separation device described above (for 20 channels) would have the manufacturing cost of approximately 10 million rubles measured in 2018 prices. Consequently, 5 separation devices (100 separation channels) would cost to a consumer 50 million rubles. The operating life of the device before overhaul is about 20 years of virtually continuous operation. Thus, the amortized cost of the equipment would be about 2.5 million rubles per year.

To assess the cost of operation, let us estimate energy intensity of the device by using the data stated in [2] adjusted for the technical parameters that would be used in practice. Apparently, there will be no energy costs of maintaining the magnetic field of the installation and the cost of ion acceleration would be negligible 100 W. Pumping equipment would require around 1 kW and about the same energy would be needed for ionization, i.e., about 2 kW. With the system operating continually, this would approximately amount to the daily rate of 50 kW·h or the annual level of 15,000 kW·h. With 1 kW of power costing 5.5 rubles, total costs would amount to 80 thousand rubles, a negligible amount. Even if we double or triple the above estimate considering the energy needed to provide illumination and air conditioning, power the control computer etc., the electricity costs would not exceed 150 to 250 thousand rubles per annum, that is, it would amount to no more than 10% of capital expenditures.

On the other hand, a 100-channel device with ion current per channel of 10^{-4} A would ensure processing of 10^{17} atoms or ~ $2 \cdot 10^{-7}$ mol of the initial product. When operating continually and considering 20% downtime required for scheduled repair and loading/unloading per year, this would correspond to approximately 6 mols of the product separated by isotopes having the purity of about 99.95%. For minor actinides, e.g., curium, this would amount to about 1.5 kg of metal, for gadolinium and erbium -- about 950 g.

If the degree of purity is reduced to, e.g., 95%, ion current may be increased up to almost 10 times. This would result in 10-time increase in productivity of the equipment. This degree of purity is quite sufficient for a number of applications. As an example, if the most valuable isotopes ^{167}Gd and ^{167}Er were to be extracted from the natural mixture to be used as burnable nuclear fuel absorbers, their efficiency would reduce the effect of enrichment only by 5% if nominally 100%-enriched isotopes are replaced with products of 95% purity. Benefits of using these products as fuel as compared to natural gadolinium and erbium will be considerable - six- and four-fold, respectively.

Let us estimate the cost of isotope-separated metals on the example of ^{167}Er with content in the naturally-occurring metal of about 23%. In a year of operation of the separation system, one could expect separation of about 50 mols of the element with the purity of around 95%. Isotope ^{167}Er would account for approximately 1/4 of these 50 mols. Consequently, the produced volume will be about 12 mols or just under 2 kg. Energy cost alone would amount to approximately 200 thousand rubles, and if capital expenditures divided by the standard service life of 20 years, the cost would be about 2.7 million rubles. Thus, the prime cost of 1 g of the isotope in terms of energy only would amount to 100 rub/g, and together with capital expenditures - 1350 rub/g.

It should be noted that the above costs are somewhat lower than market prices of the most expensive metals produced without isotope separation. As an example, 1 g of gold currently costs 2.830 thousand rubles, 1 g of palladium – 3.154 thousand rubles. Moreover, the price of the former increased during the previous year by 40% [25].

As often as not, isotope in estimating separation costs capital investments are ignored and such estimations are limited to energy costs only [26]. We would like to underline that the above estimation shows that energy intensity of electromagnetic isotope separation may be reduced by an order, as compared to the value used previously [6]. Indeed, direct energy consumption of an electromagnetic separator which operates in the Kurchatov Institute amounted to ~ 30 kW [6], i.e., they were almost 15 times as high, while their capacity was comparable to that of the device described above and a somewhat lower separation degree. The authors have no immediate data on the level of capital expenditures in the construction of traditional electromagnetic separating devices, however, indirect assessments indicate that they exceed the costs stated in the beginning of the section by two orders minimum, with comparable capacity.

Conclusions

Based on the results of the analysis, it was shown that modern methods of development and design of electrophysical installations provide give new momentum to the development of

the electromagnetic isotope separation method and allow to develop a conceptually new type of separation devices. Its energy intensity may be reduced by an order as compared to conventional solutions. Capital expenditures on the commissioning of new capacities may also be reduced considerably (by two orders, as a minimum). This makes it possible to obtain the cost of isotope-separated element comparable to the market cost of the most expensive isotope-separated metals.

The developed approach would enable the construction of flexible process lines wherein the performance of the used apparatuses would be determined only by the problem at hand and the market situation. The proposed approach is based on time-tested engineering solutions, which makes the potential installations reliable and maintainable. These installations would be highly sought both in Russia and abroad in solving a wide range of isotope separation problems, benefiting, above all else, fundamental scientific research and the medical industry. Moreover, the development and implementation of high-performance and cost-effective devices of this type may facilitate the development of new areas of consumption of rare-metal isotopes and many other elements, in particular by the atomic industry.

References

1. Henry De Wolf Smyth Atomic Energy for Military Purposes (The Smyth Report); The Official Report on the Development of the Atomic Bomb Under the Auspices of the United States Government. http://www.atomicarchive.com/Docs/SmythReport/smyth_ix-a.shtml, November 2018

2. Koch J. [ed.].Electromagnetic Isotope Separators and Applications of Electromagnetically Enriched Isotopes. Amsterdam, 1958.

3. V.S. Letokhov The principles of laser separation of isotopes. Coll. vol: Isotopes: properties, production and application. Eds V.Yu. Baranov – M.: Fizmatlit, 2005, vol. I, pp. 357-374.

4.Stanley Whitley, Review of the gas centrifuge until 1962.Part I: Principles of separation physics, Rev. Mod. Phys., 1984, 56, pp. 41–66.

5. Spicer H.G., Methods for separating stable isotopes, (Isotec Incorporated, Miamisburg, OH (United States)), Proceedings of the international symposium on isotope separation and chemical exchange uranium enrichment; Tokyo (Japan); 29 Oct - 1 Nov 1990, Fujii, Yasuhiko (Tokyo Inst. of Tech. (Japan). ResearchLab. for Nuclear Reactors); Ishida, Takanobu; Takeuchi, Kazuo (eds.); 519 p; 1992; p. 91-95; Tokyo Institute of Technology; Tokyo (Japan);

6. Bondarenko V.G., Kuzmin R.N. The electromagnetic method. Main concepts. Coll. vol: Isotopes: properties, production and application. Eds V.Yu. Baranov – M.: Fizmatlit, 2005, vol. I, pp. 290-307.

7. Chernov I.I., Kalin B.A., Binyukova S. Yu., Staltsov M.S. The effect of alloying and thermal treating on the structure and properties of zirconium. Learning guide. – M.: MIFI, 2007, 84 p.

8. Polyakov L.A., Tatarinov A.N., Monastyrev Yu.A., Ogorodnikov S.G. / Patent RU 2160153 – Method of separation of zirconium isotopes in an electromagnetic separator with the use of a source of ions. // 2000

9. Pokhitonov Yu.A., Romanovskiy V.N. Palladium in spent nuclear fuel of NPP. Prospects of isolation and use Radiochemistry. 2000, Vol. 47, No. 1, pp. 3-14.

10 Pokhitonov Yu.A., Romanovskiy V.N. Methods of isolation of palladium from irradiated fuel and prospects of its use in immobilization of long-lived radionuclides. Publications of V.G. Khlopin Radium Institute St. Petersburg, Vol. XVII, 2014, pp. 5-55.

11. Novikov V.V., Bibilashvili Yu.K., Mikheev E.N. et al. A study of VVER fuel containing alloying additive. // Atomic energy. 2008. Vol. 105 Issue 4. pp. 205-210.
12. Lysikov A.V., Kuleshov A.V., Samokhvalov A.N. / Patent RU 2362223 – Nuclear urania-gadolinia fuel with high burn-up based on uranium dioxide, and methods of its production (options) // Invention Bulletin. 2009. No. 20.
13. Kazmin D.N., Yakubenko I.A. Nuclear fuel for NPP: the current state and promising developments. // Global nuclear safety, 2013, No. 4(9), pp. 53-57.
14. Levin V.I. Production of radioactive isotopes // M., Atomizdat, 1972, 256 p.
15. V. Tarasov, O. Andreev, E. Romanov et al. Production of no-carrier added Lutetium-177 by irradiation of enriched Ytterbium-176 //Current radiopharmaceuticals, V.8(2), p.95–106.
16. Buchachenko A.D. Kuznetsov D.A. Magnetic isotope effect of magnesium -- the key to understanding the mechanical chemistry behind phosphorylazing enzymes as biological machines // Molecular Biology. - 2006. – Vol. 40. – p. 12.
17. Thomas Walczyk and Friedhelm von Blanckenburg. Science. 15 March 2002: Vol. 295. no. 5562, pp. 2065.
18. Alyamovskiy I.V., Electron beams and electron beam guns, M., 1966.
19. Description of Separative Work Unit, (https://web.archive.org/web/20130209041119 /http://www.fas.org/programs/ssp/nukes/effects/swu.html) // Nuclear Information Project, FAS, December 2018.
20. Alexandrov M.L., Gall L.N., Pliss N.S. A study of ion dispersion in mass spectrometers using the statistical modelling method. ZhTF, 1974, vol. 44, No. 6, p. 1302.
21. Alexandrov M.L., Gall L.N., Pliss N.S., Shcherbakov A.P. A study of ion beam dispersion reflected from slit edges of collimating diaphragms. ZhTF, 1978, vol. 48, No. 5, p. 1026.
22. Blashenkov N.M., Samsonova N.S., Semyonov A.A., Gall L.N, Gall N.R. Application of mass spectrometry using ERIAD for the detection of trace amounts of beryllium. 3rd Assembly of Analysts of Russia, Moscow, October, 2017, p.
23. Averin I.A., Berdnikov A.S., Gall N.R., The principle of similarity of trajectories of charged particles having various masses traveling in Euler-uniform electric and magnetic fields. PZhTF, 2017, No. 3, pp. 39-42.
24. Molokovskij S.I., Sushkov A.D. Intensive electron and ion beams, 2nd ed., L., 1991/
25 https://skolko247.ru/zoloto-serebro-platina-palladij-kurs-tsena-segodnya, February 2019
26. http://portal.tpu.ru:7777/departments/otdel/publish/izdaniya_razrabotanye_v_ramkah_ IOP/ Table /metod_obespechh_obor_zac.pdf, December 2018.

UDC 621.039.548

FINITE-ELEMENT STRENGTH ANALYSIS OF WELDED JUNCTIONS OF WWER REACTOR FUEL ELEMENTS

A. V. Krupkin, V. I. Kuznetsov, V. V. Novikov, O.M. Petrov
SC «A.A. Bochvar High-Technology Research Institute of Inorganic Materials», Moscow

The publication discusses a study of welded junction strength of WWER-1000 reactor fuel element when removed from a fuel assembly.
A stress raiser occurs at the welded ridge, which adversely affects the strength of the welded junction.
The ridge has a complex geometry which requires estimates in 2D. Finite-element analysis, as part of this study, was carried out using the finite-element software suite ANSYS.
It was shown that the developed analytical model may be used for the substantiation of welded junction strength of WWER reactor fuel elements.

Keywords: fuel element, welded junction, power-producing reactor, finite-element method, computational simulation, strength analysis.

Introduction

Modern design of fuel assemblies permits the removal of fuel elements in order to inspect them for possible breakdown, loss of containment and failure.

The disassembly may be carried out at an inspection bench or in a hot cell with relevant equipment.

The process involves a potential hazard of a rupture of the upper caps followed by undesirable depressurization of fuel elements during their disassembly.

Due to these considerations, Chief Designer has set the task of determining the effort needed to remove a fuel element from fuel assembly.

The authors assume the possible location of fuel assembly breakdown to be the welded junction site at the upper hermetic seal where the highest strains occur.

The task is further complicated by a structural feature of fuel element welded junctions: welded ridges on the outside and the inside of the welded junction that act as stress raisers.

A typical slice of a welded junction is shown in Fig. 1.

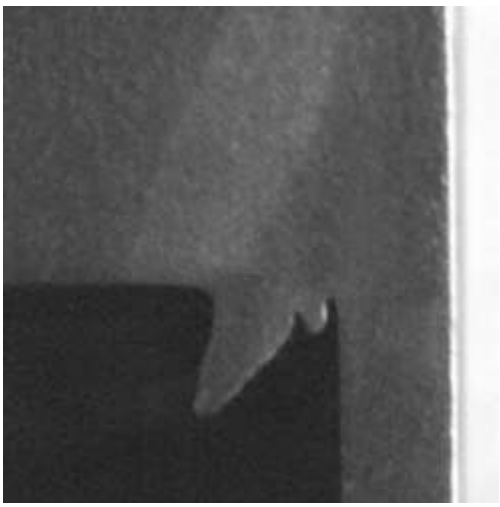

FIG. 1. An example of a welded junction of a fuel element.

It should be noted that a welding ridge has a complex geometry which calls for computer-aided estimations.

In this study, the analysis of welded junction was carried out in a 2D representation using the ANSYS finite-element software suite [1]. This definition is an assumption for problems featuring axial symmetry. Despite the fact that an actual welding ridge does not feature an ideal axial symmetry, the above definition of the problem is applicable for the declared objective (determination of the critical force of fuel element removal). This deviation will be considered when selecting the design assurance coefficient.

The objective of the study is to research the effect of a specific welded junction (welding ridge) type on the strength of fuel element structure.

To study the effect of a specific form of welding ridge on the stress-strain behavior, the *"submodeling"* technique is used.

Stress-strain behavior (SSB) of various configurations of welded junction was analyzed as part of the study.

1. Design features of the welded junction

The location of the upper cap attachment to the fuel element cladding is shown in Fig. 2 (welded junction No. 2).

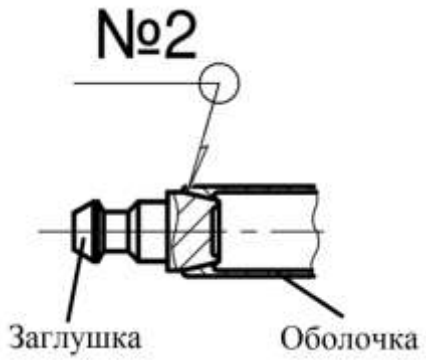

Заглушка	Cap
Оболочка	Cladding

FIG. 2. The site of the upper cap attachment to the fuel element cladding.

Welding is performed by way of pressing the cap with forced fitting. During this process, electric current is passed through the joint. Electricity heats the material.

One particular feature of this type is the formation of a welding ridge which acts as a stress raiser within the structure under stress.

2. Problem definition

The study evaluates the strength of the welded junction site of the upper cap and fuel element cladding.

The problem of continuum dynamics in an axially symmetrical 2D representation was addressed.

It should be noted that stresses on the welded junction are defined by the difference of the external and internal pressures. These are compressing stresses, and they do not threaten the strength.

The most crucial, in terms of welded junction strength, is removal of the fuel element from the fuel assembly. Fuel element is removed by force applied to the upper cap which subjects the welded junction to considerable tension stresses.

An analysis of force factors shows that the stress-strain behavior (SSB) of the lower part of the fuel element is determined by the force applied during the disassembly of the collet junction. This force is supplemented in the upper section by the friction force of the fuel element at spacer grids. For this reason, welded junction No. 2 is always more strained during the fuel element removal. Considering the above, the strength of welded junction No. 2 during the fuel element extraction from the fuel assembly was analyzed.

3. Geometrical representation and boundary conditions

The geometrical representation of welded junction No. 2 is shown in Fig. 3.

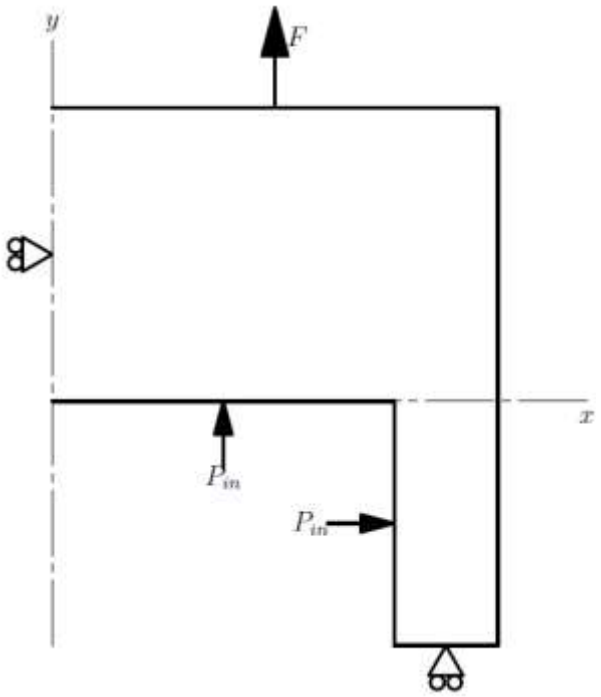

FIG. 3. Geometrical representation of the welded junction site

The following boundary conditions were applied to the model (Fig. 3):

– radial displacements (UX = 0) were determined for the axis of symmetry (y);

– vertical displacements (UY = 0) were determined along the bottom surface of the cladding;

– a tensile force F was applied to the top surface of the cap;

– pressure P_{in} was applied to the inside surface of the model.

The tensile force F was increased from 0 to the limit value corresponding to structure rupture, this was determined by the moment of infinite deformation buildup with further force increase (the divergence of the numerical algorithm of the solution).

The assumed structural parameters of the fuel element are shown in Table 1. The “new generation” fuel element was analyzed. This type features a thinner cladding and increased injection pressure.

TABLE 1

Structural parameters of fuel element used in the estimation

Parameter	Value
Outer diameter of the cladding, mm	9.06
Inner diameter of the cladding, mm	7.99
Injection pressure (cold), MPa	2.7

4. Finite-element model

The developed geometrical model was automatically broken down to finite elements having the dimension of ≈ 0.1δ where δ is the cladding thickness.

Simulation was carried out using the eight-node isoparametric element PLANE183.

The PLANE183 element is intended for the simulation of mechanics problems that involve nonlinearities of various types, e.g., plasticity, creep, significant deformations etc.

Geometric parameters of PLANE183 are shown in Fig. 4.

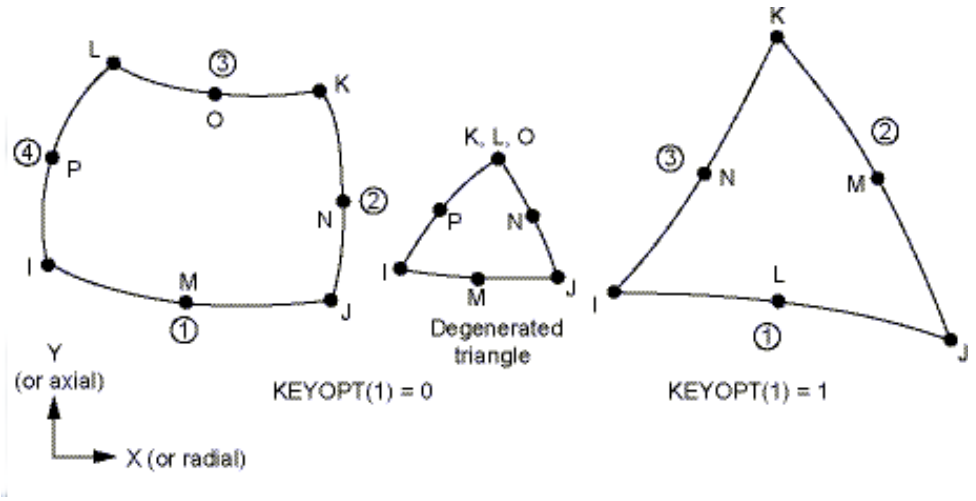

FIG. 4. Geometric parameters of PLANE183

The parameters of the finite-element model are shown in Table 2.

TABLE 2

Model parameters

Parameter	Value
Degrees of freedom	*UX, UY*
Number of elements	8165
Number of nodes	25,024
Time required for simulation of one option, h	0.05

The view of the finite-element model together with the applied boundary conditions is shown in Fig.5

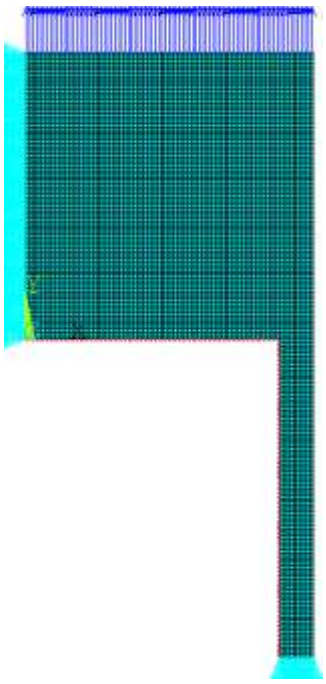

FIG. 5. The finite-element model of the welded junction site

5. Properties of the material

The strength analysis of the structure uses the bilinear elastic-plastic model with isotropic hardening.

The deformation diagram together with the designations assumed for the model is shown in Fig. 6.

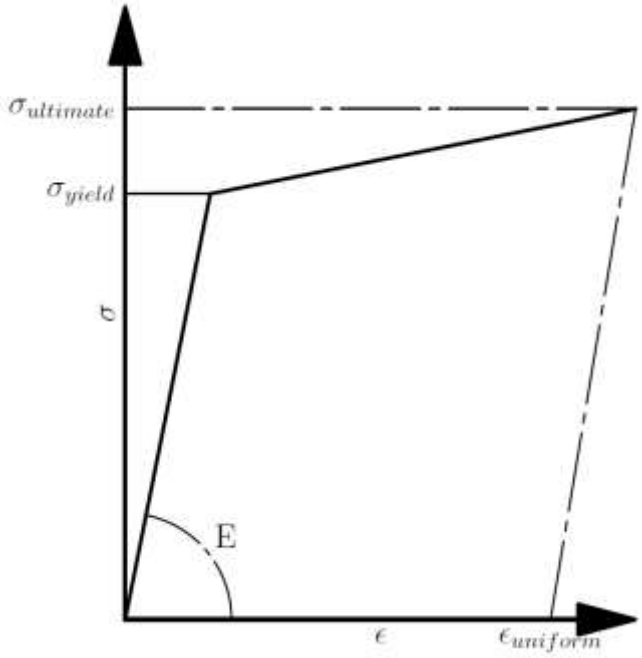

FIG. 6. Bilinear diagram of material deformation

Elastic constants were preset in accordance with the data base [2], the constants are shown in Table 3.

TABLE 3

Elastic constants of E110 alloy at room temperature

Parameter	Value
Young's modulus, hPa	95
Poisson’s ratio, nondimensional	0.408

The data obtained by straining cladding tubes made of E110opt alloy longitudinally at room temperature [3] were used in order to set transient mechanical properties. The conservative approach was used in the selection of the junction area material with minimum properties (the fuel element cladding material).

The values of constants assumed for the estimations are shown in Table 4.

TABLE 4

Transient mechanical properties of new cladding
tubes of fuel element made of E110opt alloy in the longitudinal direction at 20°C

Parameter	Value range	Assumed value
Breaking strength, MPa	384 -- 412	384
Creep limit, MPa	299 -- 341	299
Relative elongation, %	32 -- 42	32

5. Estimation results

5.1 The force/displacement diagram

The dependency of the axial displacement of the cap on the force applied is shown in Fig. 7.

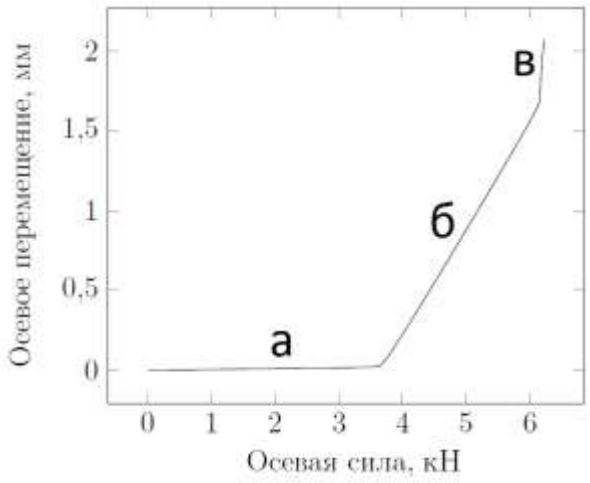

Осевое перемещение, мм	Axial displacement, mm
Осевая сила, кН	Axial force, kN

FIG. 7. Dependency of the axial displacement of the upper cap on the applied force

Fig. 7 shows three typical deformation sites:

a) elastic deformation, $F < 3.62$ kN;

b) plastic hardening, 3.62 kN $< F < 6.23$ kN;

в) infinite deformation buildup (rupture), $F > 6.23$ kN.

Based on the above, if we assume that plastic deformation of the material is unacceptable, the critical force of removal would have the value of $F = 3.62$ kN.

The insignificant decrease of the critical removal force is caused by:

– taking into consideration the internal pressure; and

– taking into consideration the plasticity zone around the stress raiser.

Following the estimation results, the following conclusions can be made:

a) the effect of internal pressure and the stress raiser at the welded junction site on the critical fuel element removal force is insignificant;

b) granted that plastic deformation of the material is unacceptable, the critical removal force has the value of 3.62 kN.

It should be noted that the simulation took into consideration the work of the material in the elastic zone. Here, the creep limit of the new cladding was assumed as the criterion. The creep limit will be much higher during irradiation. Thus, this estimation is conservative in the case of extracting a fuel element from a spent assembly.

5.2. The stress-strain behavior of the welded juncture area.

Fig. from 8 to 11 show the distribution of maximum primary stresses and equivalent plastic deformations for axial forces within the 2 kN - 3 kN range.

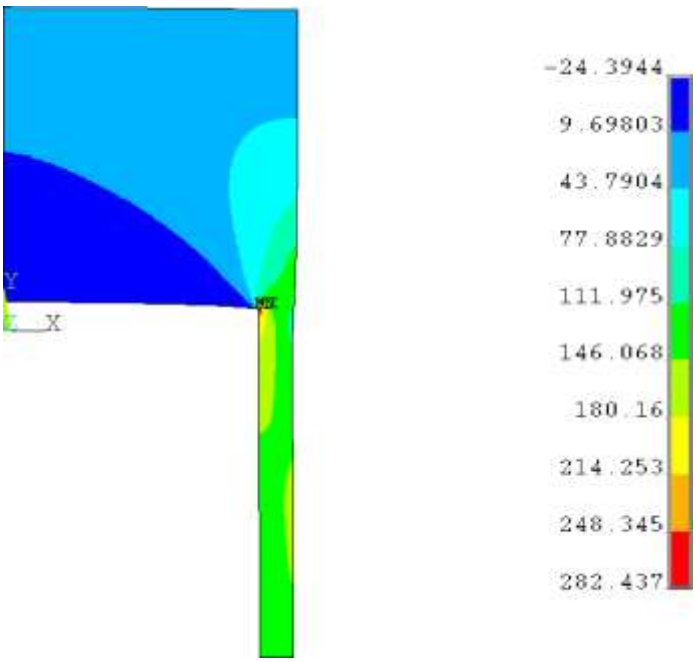

FIG. 8. Distribution of the first primary stress in the welded juncture area under the fuel element removal force of 2000 N. Strain scale in MPa

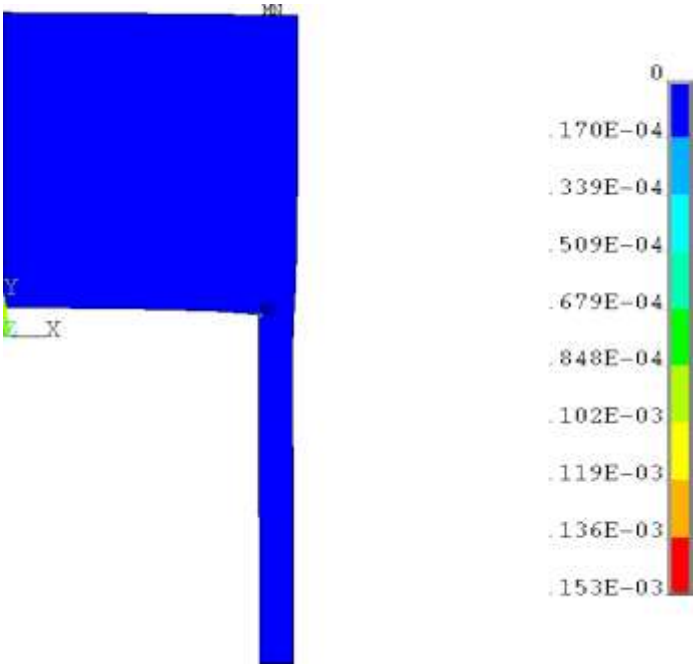

FIG. 9. Distribution of the plastic deformation intensity within the welded junction area under the fuel element removal force of 2000 N. Deformation scale in relative units

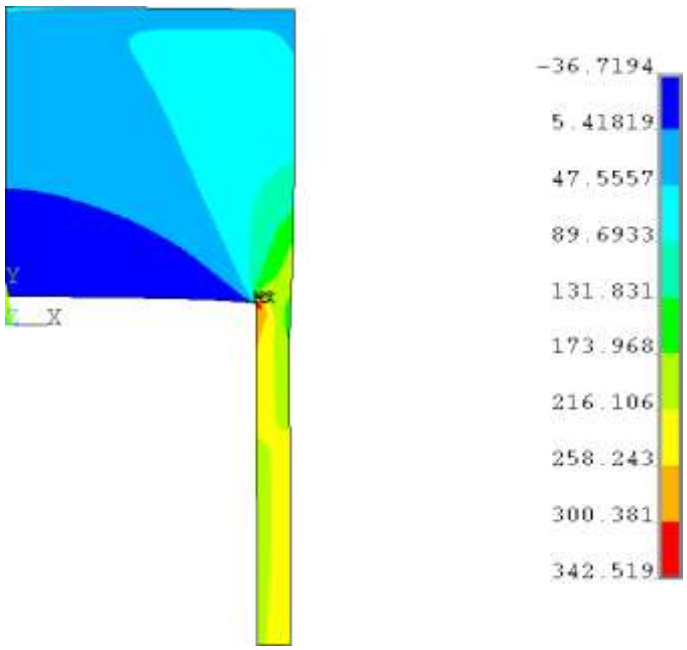

FIG. 10. Distribution of the first primary stress in the welded juncture area under the fuel element removal force of 3000 N. Strain scale in MPa

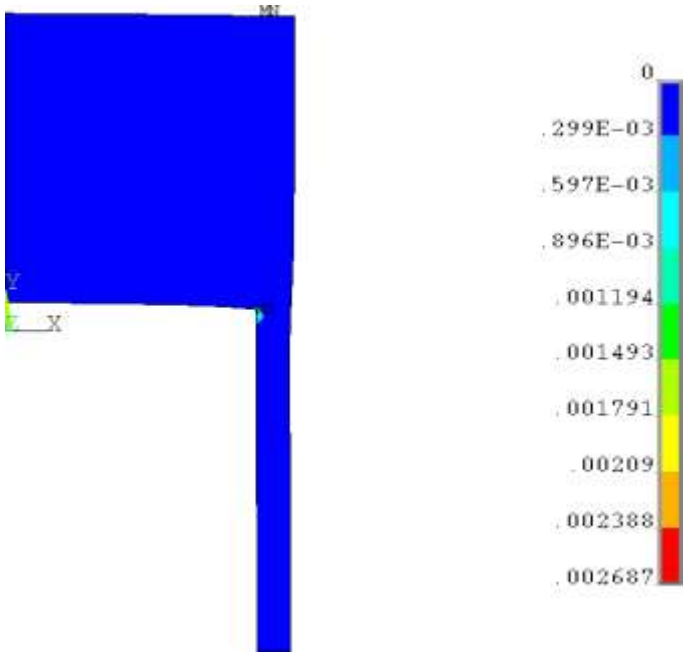

FIG. 11. Distribution of the plastic deformation intensity within the welded junction area under the fuel element removal force of 3000 N. Deformation scale in relative units

The results of the estimation are summarized in Table 5.

TABLE 5.

Results of SSB estimation at the stress raiser site of the welded junction

Axial force, kN	Maximum equivalent plastic deformation in relative units	Maximum primary strains, MPa
1.00	0.000	165
2.00	$0.153 \cdot 10^{-3}$	282
3.00	$0.269 \cdot 10^{-2}$	343

Fig. from 8 to 11 show that a plastic deformation area forms in the stress raiser area at stresses exceeding 2 kN. The area expands with a stress increase.

However, when stresses approach the point of structure rupture of F > 4 kN, the area of maximum plastic deformation moves downwards from the stress raiser. This indicates structure rupture along the thickness of the casing.

The destruction of the material over its thickness is corroborated by experimental tensile tests of welded junctions [4].

6. SSB at the stress raiser site

This part of simulation was performed to further determine the SSB structure obtained during previous estimations for the dangerous area of the stress raiser.

The objective of this part of simulations was to evaluate the effect of a specific geometrical configuration of the welded junction on SSB.

The analysis uses the submodeling technique. This technique uses a method involving transfer of the solution obtained for the principal model to a more detailed sub-model as boundary conditions.

6.1. The analysis of geometrical configurations of welded junctions

The analysis was based on the data obtained for slices of actual configurations that were converted into digital form.

The analyzed geometrical configurations are shown in Fig. 12.

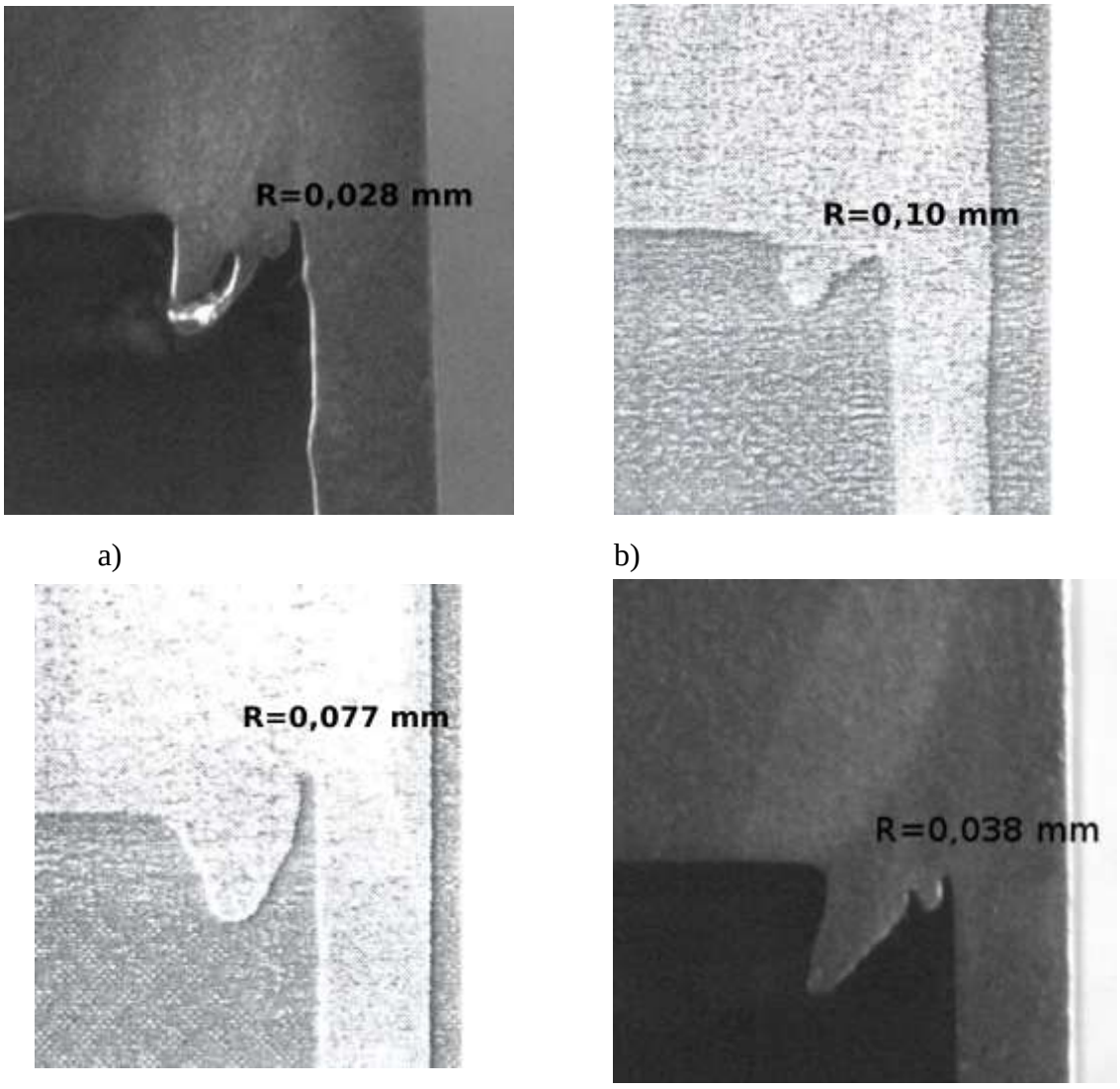

FIG. 12. Different geometrical configurations of welded junctions

Rounding radii at the cap/cladding interface are stated for each configuration shown in Fig. 12.

As we can see from Fig. 12, rounding radii lie within the range of 0.028 mm to 0.10 mm.

A considerable variance of the final welded junction geometry can be observed.

6.2 Simulation of welded junction geometry using the ANSYS suite

In order to allow simulation using the ANSYS software, the geometrical parameters of welded junctions shown in Fig. 13 were converted into digital form using Bezier curves [5].

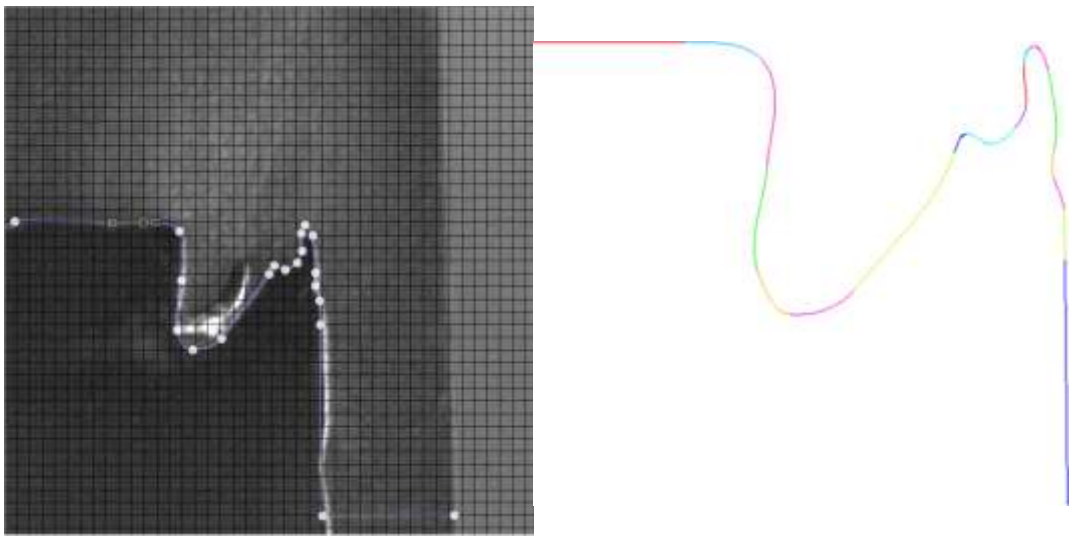

a) b)

FIG. 13. Simulation of welded junction geometry using the ANSYS software suite: a) digitalization of the geometry using Bezier curves; b) simulation of curves using the ANSYS software

The resulting curves were simulated with ANSYS using special curve sections.

As the result, the initial geometry was converted without the loss of curve smoothness (this would have been impossible to avoid if the geometry had been simulated using a polynome).

6.3. The finite-element models

The average size in all the models of an element was assumed as 1δ where δ is cladding thickness.

This dimension was assumed based on finite-element studies of models featuring varying element sizes. The absence of disruptions in the solution along element boundaries was assumed as the suitability criterion.

The resulting finite-element models for each geometrical configuration are shown in Fig. 14.

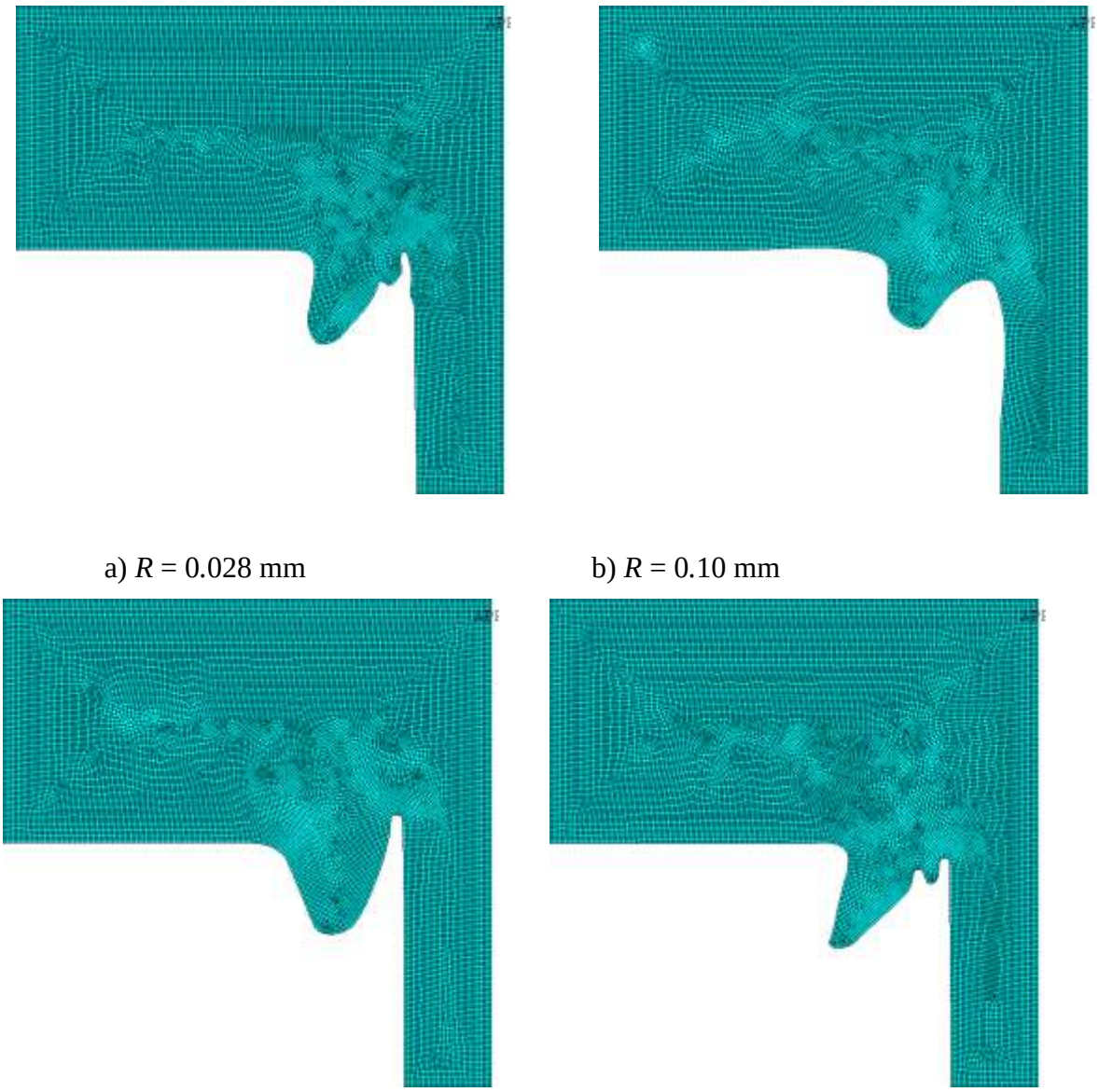

a) R = 0.028 mm b) R = 0.10 mm

c) R = 0.077 mm d) R = 0.038 mm

FIG. 14. Finite-element models of various welded junction configurations

The parameters of the finite-element models generated are shown in Table 6.

TABLE 6

Finite-element model parameters

Model No.	1	2	3	4
Rounding radius, mm	0.028	0.10	0.077	0.038
Number of elements	20,310	19,176	19,337	19,947
Number of nodes	61,655	58,219	58,740	60,568
Simulation time, min	1.916	1.633	1.866	1.983

6.4. The estimation results

For the presentation of the estimation results, two typical removal forces were chosen at the elastic and elastic-plastic deformation areas of the force-displacement curve (Fig. 7): 3000 N and 5000 N, respectively.

6.4.1 SSB within the elastic deformation area

Fig. 15 and 16 show the distribution of maximum primary stresses and equivalent plastic deformations under the force at the cap equal to 3000 N.

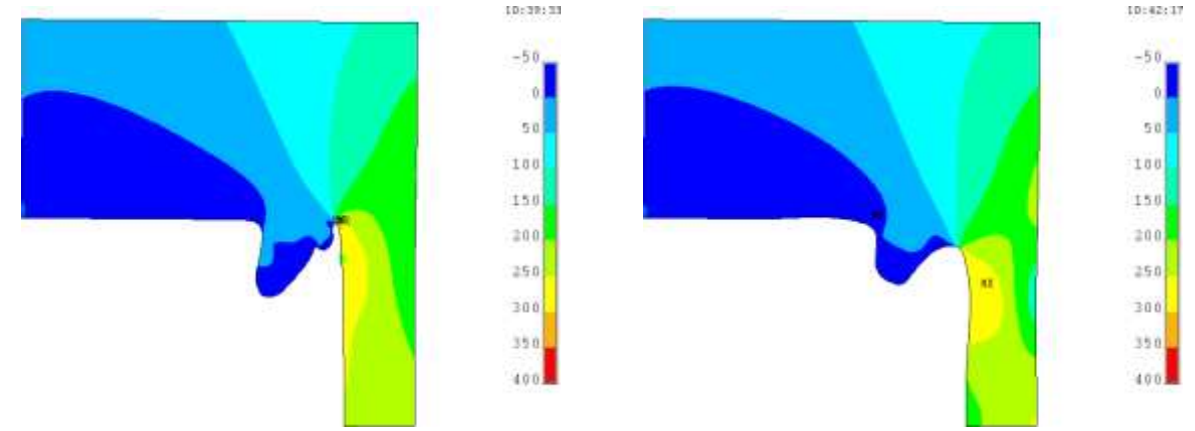

a) R = 0.028 mm b) R = 0.10 mm

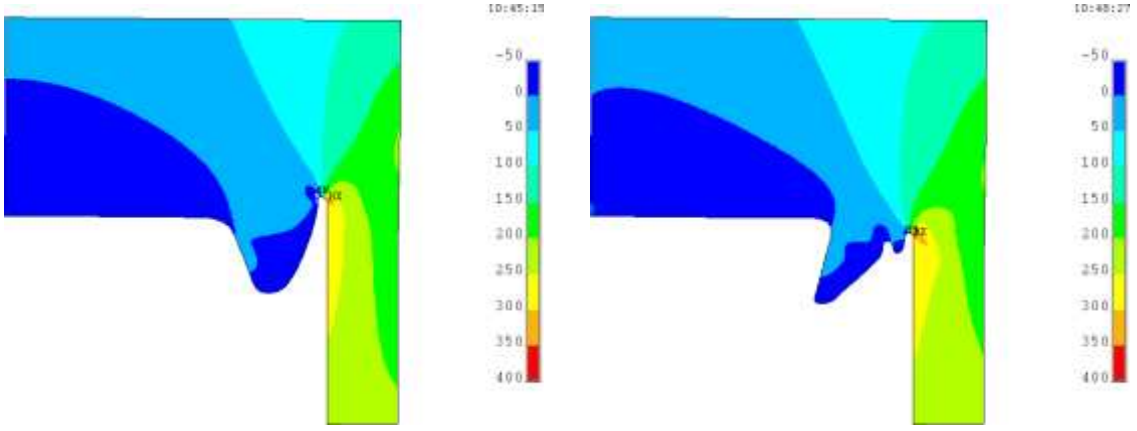

c) R = 0.077 mm d) R = 0.038 mm

FIG. 15. Maximum values of primary stresses under the removal force of 3000 N, in MPa

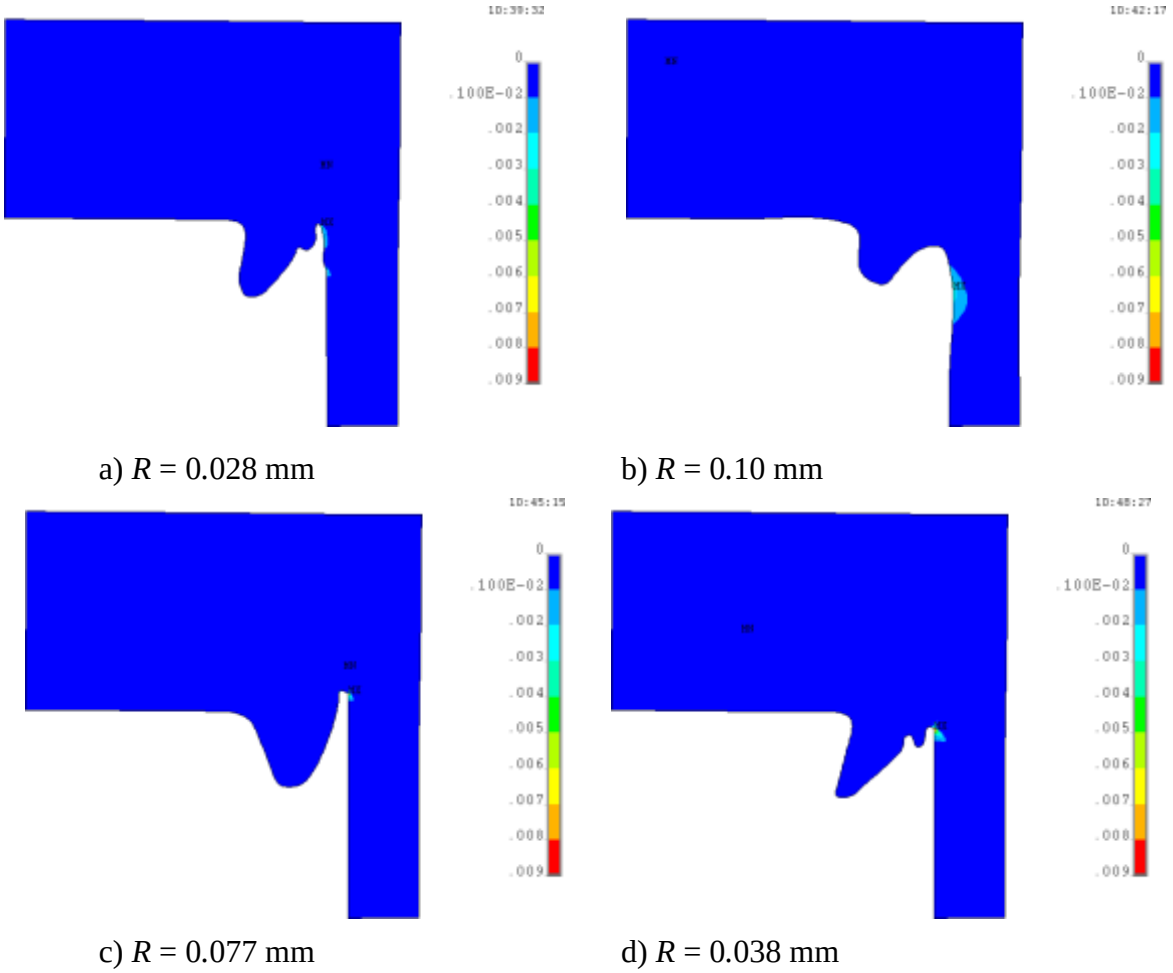

a) R = 0.028 mm b) R = 0.10 mm

c) R = 0.077 mm d) R = 0.038 mm

FIG. 16. Values of equivalent plastic deformations under the removal force of 3000 N, in relative units

Limit values of stresses and plastic deformations under this force are stated in Table 7.

TABLE 7

Results of the estimation of SSB at the welded junction area under the fuel element removal force of 3000 N

Model No.	Rounding radius, mm	Maximum primary strains, MPa	Maximum equivalent plastic deformations, relative units
1	0.028	316	0.0030
2	0.10	294	0.0022
3	0.077	366	0.0092
4	0.038	377	0.0161

The results of the simulations show that a plasticity area forms at the stress raiser site. However, the size of the plasticity zone is much smaller than the claddingg thickness, thus it has no significant effect on the structure tightness.

Maximum stresses develop at the stress raiser site, they vary among the structures within the range of 294 to 377 MPa. This means that the geometry of the welded junction has a significant effect on the SSB of the structure.

The lowest stresses developed in the structure with the largest rounding radius at the stress raiser site.

6.4.2 SSB in the elastic-plastic deformation area

Fig. 17 and 18 show the distribution of maximum primary stresses and equivalent plastic deformations under the force at the cap equal to 5000 N.

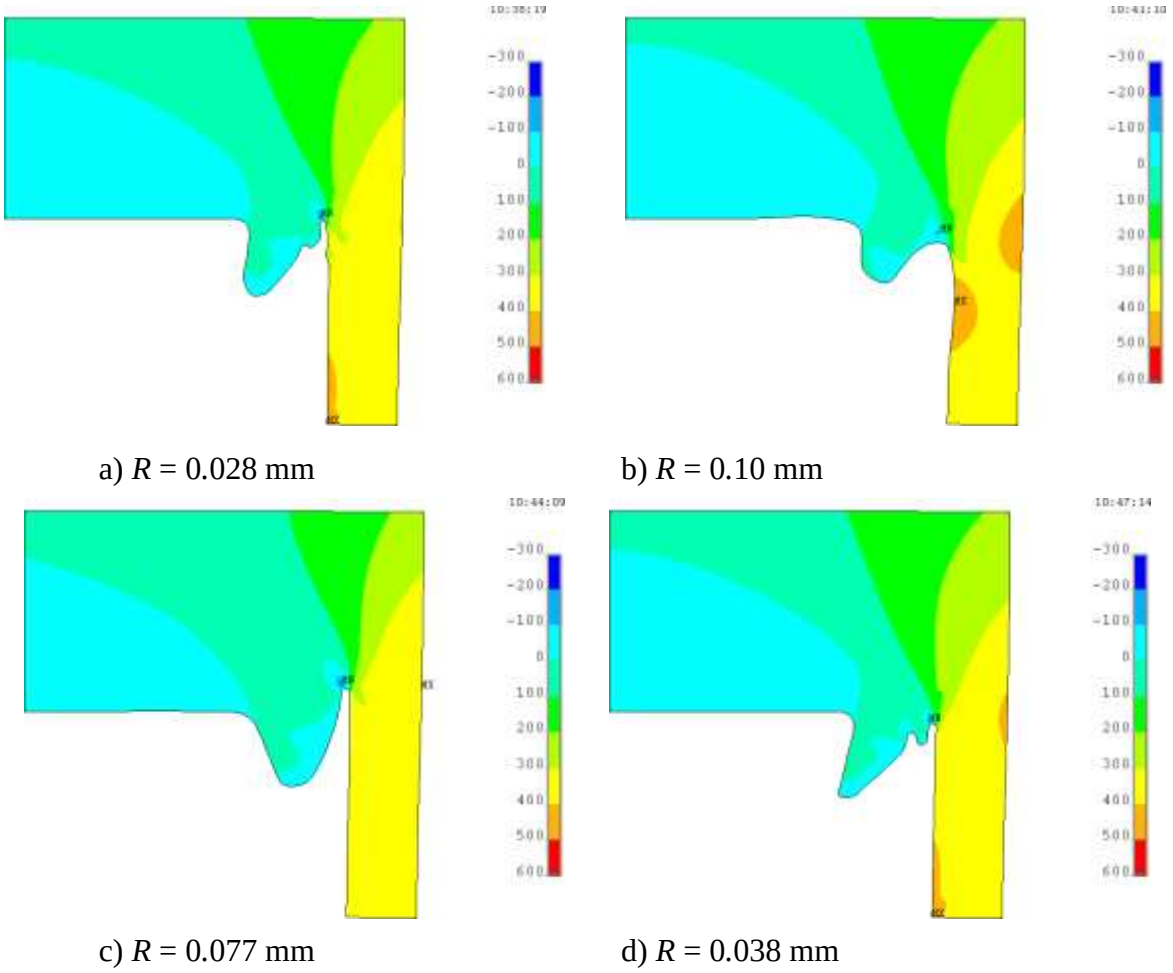

a) R = 0.028 mm b) R = 0.10 mm

c) R = 0.077 mm d) R = 0.038 mm

FIG. 17. Maximum values of primary stresses under the removal force of 5000 N, in MPa

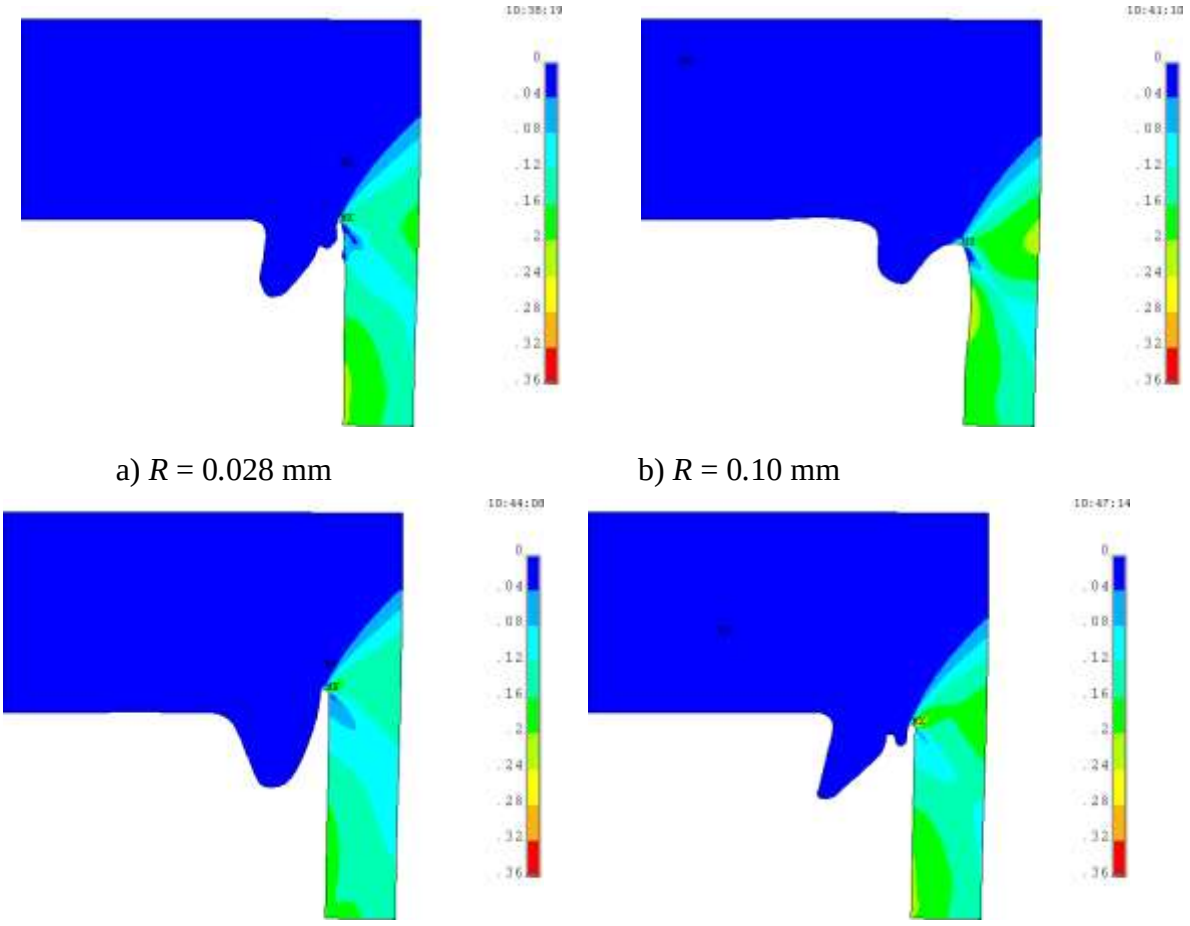

a) R = 0.028 mm b) R = 0.10 mm

c) R = 0.077 mm d) R = 0.038 mm

FIG. 18. Values of equivalent plastic deformations under the removal force of 5000 N, in relative units

Limit values of stresses and plastic deformations under this force are stated in Table 8.

TABLE 8

Estimation results of the SSB at the welded junction area under the fuel element removal force of 5000 N

Model No.	Rounding radius, mm	Maximum primary strains, MPa	Maximum equivalent plastic deformations, relative units
1	0.028	456	0.316
2	0.10	440	0.273
3	0.077	392	0.251
4	0.038	480	0.324

The analysis of the results reveals that stress-strain behavior in this area is fundamentally different.

The plasticity zone now stretches throughout the thickness of the casing. The maximum of primary stresses is displaced downwards, from the stress raiser site towards the cladding surface.

Thus, rounding radius at the stress raiser site no longer plays the defining role in the distribution of stresses.

Conclusion

The study determines the critical force of fuel element removal from a fuel assembly. The effect of a specific type of welded junction (welding ridge) on the strength of fuel element structure was studied to analyze the complex geometry of welded junction.

To this end, an analytical model of the welded junction of the fuel element in an axially symmetrical 2D representation was developed with the ANSYS finite-element software. The model included:

– a geometric model;

– a finite element mesh;

– applied boundary conditions and stress; and

– solver parameters.

The estimation used the submodelling technique. This technique enables to account for the geometrical form of a specific welded junction.

The analysis of the simulation results revealed a significant response of SSB of the structure to the welded junction geometry under elastic deformation: the smaller the rounding radius is at the stress raiser site, the higher the maximum stress level is. Under the elastic-plastic deformation, the rounding radius no longer plays the defining role in the distribution of stress. This indicates that estimations must be carried out in the elastic-plastic representation.

The critical force of fuel element removal from the fuel assembly was found to be equal to 3.62 kN (without regard to the assurance coefficient). Estimations revealed that rupture during the operation occurred within the cladding material. This is consistent with experimental data (tensile tests of welded junctions).

References

1. ANSYS, Inc. ANSYS finite element software. User number 662129 dated 28.12.2011.

2. G. Kobylianskiy Radiation resistance of zirconium and zirconium alloys / G.P. Kobylianskiy, A.E. Novoselov. — CRC RF RIAR, 1996.

3. V.I. Kuznetsov, P.V. Fedotov et. al. Development of the first version of E110 alloy property library for PRIME software: Report: 12330 / JSC VNIINM – Moscow: 2016.

4. A. V. Kozlov, O.K. Peslyak Development of butt resistance welding methods for the pressurization of fuel elements with casings made of zirconium alloys: Report: 1419 / JSC VNIINM – Moscow: 1978.

5. D. Rogers, Mathematical principles of computer graphics / D. Rogers, J. Adams – M.: Mir, 2001.

UDC: 669.293-669.295]:538.945

A STUDY OF THE CURRENT-CARRYING CAPABILITY OF Nb-Ti-BASED SUPERCONDUCTORS FOR CBM DETECTOR MAGNET

Yu. V. Karasev, V.Yu. Korpusov, N.I. Salunin, A.V. Malchenkov, S.A. Shevyakova, I.N. Gubkin, E.V. Nikulenko, P.A. Lukyanov, M.V. Polikarpova, Yu.V. Konovalov, I. M. Abdyukhanov

SC «A.A. Bochvar High-Technology Research Institute of Inorganic Materials»,Moscow

For the development of CBM detector magnet as part of the FAIR accelerator facility, a monolithic version of conductor with the section of 2.02×3.25 mm comprising 23 clusters of 31 Nb-Ti filaments each. The required level of critical current in the wire (4.2 K; 5 T) is more than 2.3 kA. Field dependencies for critical current density $J_c(B)$ within the magnetic field range of 7.5 T to 10 T were determined and magnetization loops M(H) were recorded for fields ranging from 0 to 8 T. Based on the pinning models and experimental data, $J_c(B)$, the field dependency of the critical current density was plotted for a wide range of fields. The estimated critical current density of the wire is at least 3000 A/mm^2 (4.2 K, 5 T). This corresponds to the critical current level of more than 2.5 kA. The value correlates with the critical current density estimated based on magnetization degree within a 5 T field. The temperature and field dependency of the critical current density $J_c(B, T)$ was determined and, on the basis of this calculation, the critical current of wires under the operating conditions of magnet winding (3.25 T and 4.5 K) was estimated.

Keywords: Nb-Ti-based superconductor, critical current, critical current density, “cold assembly”.

Introduction

Facility for Antiproton and Ion Research (FAIR) is being erected on the outskirts of Darmstadt (Germany). The facility will provide unique opportunities for studies in the field of plasma physics. The accelerator facility is powered by advanced superconductor magnet technologies, and will include a compressed baryonic matter (CBM) detector. The strategy of experiments conducted at CBM involves systemic tests of particles formed in nuclear collisions at various energies with unprecedented accuracy and produces unique statistical data.

The core of the detector is a superconducting dipole magnet with the cross-section diameter of 2 m. The magnet is essentially comprised of two superconducting coils weighting approximately 1 ton made of insulated NbTi wire directly cooled by liquid helium. The maximum field strength achieved at the magnet winding is 3.25 T.

To implement the CBM magnet, the customer initially selected the conductor design in the form of a NbTi strand sealed within a copper bus-bar having the dimensions of 2,02×3,25

mm (the so-called “wire-in-bus-bar” which has the minimum intensity of critical current of ≥ 1754 A (4.2 K; 5 T) and the Cu/NbTi ratio of 9.1±0.5.

A similar wire featuring a soldered contact (“wire-in-bus-bar”) was implemented by OST [1] in the FAIR Super-FRS dipole project. Nevertheless, the soldered contact may cause additional heating of the wire in cases of high contact resistance, and complicates the manufacturing of a wire with the required characteristics if the soldered-in NbTi strand diameter is increased by more than 0.9 mm.

Following the results of additional studies, the developers of the magnet restated their requirements to the NbTi wire of the CBM detector magnet. They are shown in Table 1.

TABLE 1

Main requirements to the NbTi wire of the CBM detector magnet

Parameter	**Value**
Wire height, mm	2.02
Wire width, mm	3.25
Corner radius R_1, mm	0.45
Estimated filament diameter, μm	< 40
Twist pitch, mm	≤ 45
RRR	> 100
I_c (4.2 K, 5 T), min., A	2270
Piece length, km	5
Number of pieces, pcs.	≥ 6
Cu/NbTi ratio	$7.4^{-1.0}$

In order to achieve the required characteristics of the future dipole magnet while preserving initial physical dimensions of cross-section of the NbTi wire and the number of windings, minimum critical current and the ratio of the NbTi alloy within the wire section were increased, to ≥ 2270 A (4.2 K; 5 T) and 7.4:1, respectively. In this case, manufacturing the CBM detector wire using the “wire-in-bus-bar” does not seem realistic due to manufacturing structural limitations of the soldered-in NbTi strand.

JSC VNIINM has developed an alternative solution for the manufacturing of the wire compliant with the stated requirements which involves manufacturing a monolithic version of the wire by way of “cold assembly” from a long length integrated pipe-like blank using a reiterated assembly arrangement. At the final stage of manufacturing, the round wire was twisted and gaged to produce the ultimate rectangular section. In order to evaluate the effect of twisting and gaging on the degradation of current-carrying capacity of the wire, test specimens of a round wire with the same section were produced, both with twisting and without it. Cross-sections of the resulting wires are shown in Fig. 1

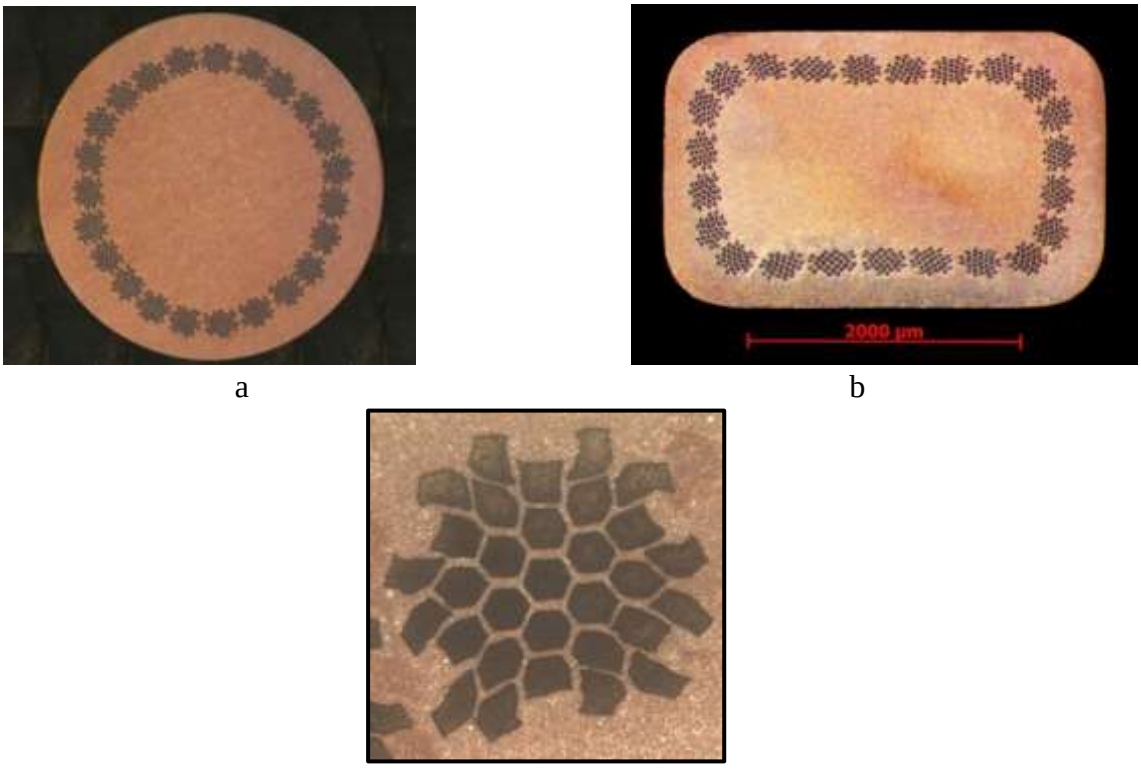

a b

c

FIG. 1. Cross-section of the 713- filament NbTi wire for the dipole magnet of CBM detector (the monolithic version): a - test round section wire (Ø 2.85 mm); b - finished square section wire (2.02×3.25 mm); c - fragment of the 31-filament cluster of the finished wires

1 Methods of critical current density estimation $J_c(B)$

Critical current density was determined on the basis of current-voltage relationships obtained during tests of samples having the approximate length of 1.5 m cut from the test and production batch wires with the section of 2.02×3.25 mm, as well as tests of the model wire which was produced by drawing a 31-filament cluster down to the diameter of 0.31 mm. The specimens were wound on a cylindrical mandrel with the diameter of 32 mm made of Ti-6Al-4V alloy which featured grooves for the specimen. Current-voltage relationships (CVR) were measured on specimens submerged in liquid helium, in cryostats accommodating 13 T solenoids. Measurements were carried out in cryogenic superconductor test laboratories of JSC VNIINM and NRI KI using equivalent procedures. CVR measurements were done after stabilization of magnetic field of the solenoid at four magnetic field induction levels within the range of 10 to 8.5 T (at JSC VNIINM) and 10 to 7.5 T (at NRI KI). The lower limit of magnetic field induction was established by the threshold values of critical current for given test conditions (1300 A). CVR were recorded when the intensity of current in the specimen was increased to 10 A/s, up to the voltage of 50 to 100 mkV/m. The current corresponding to electric field of 10 mkV/m within the specimen was taken as the critical current.

In fields with the intensity of less than 5 T where direct transport measurements of critical currents are impossible, critical current density was determined by measuring

magnetization $M(B)$ using a vibrating-coil magnetometer submerged in liquid helium (- 5 T, +5 T).

2 Experimental results and discussion

2.1 Field dependencies $J_c(B)$ of the model wire

The superconducting properties of Nb-Ti conductor was optimized at model 31-filament wires (Fig. 2) with total duration of annealing and the magnitude of final deformation varying within the limits shown in Table 2.

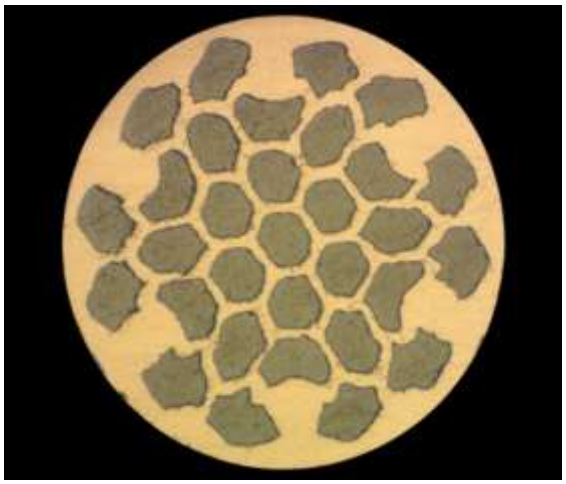

FIG. 2. Model 31-filament wire with the diameter of 0.31 mm

TABLE 2

Current-carrying properties and manufacturing regimes of the model Nb-Ti wire (Ø 0.31 mm)

Specimen No.	Total annealing session duration at t=385°C, h	Final drawing	I_c (4.2 K; 5 T), A	J_c (4.2 K; 5 T), A/mm^2
4 (1)	320	81.6	119	3145
No. 1-2	320	75.9	111	2935
No. 1-5	400	125.3	103	2723
No. 2-1	400	81.6	120	3173
No. 2-2	400	75.9	120	3173

Table 2 indicates that the optimal value of the final drawing is approximately 80, with the total duration of five annealing sessions of 400 h. Under these conditions, the resulting J_c (4.2 K; 5 T) is > 3000 A/mm^2.

In order to determine field dependency of critical current within the wide range of magnetic fields, the following empiric equation based on the pinning mechanism [2] was used.

$$J_c(B) = \frac{C_0}{B} b^{\alpha} (1-b)^{\beta} \qquad -1$$

where $b = B/B_{c2}$ is the reduced field,

B_{c2} is the upper critical field;

C_0, α *and* β are parameters that depend on the structure and composition of the material. The combination of these parameters determines the microstructure of Nb-Ti strands achieved during technological conversion. The equation (1) is solved by selecting an optimal combination of parameters stated in Table 3 by stepwise approximation of the design curve to experimental points. The estimated dependency $J_c(B)$ for the model wire as compared to experimental points is shown in Fig. 3.

TABLE 3

Equation (1) solution parameters

C_0 A×T	$B_{c2}(0)$, T	α	β
46,959	10.0	0.8	0.87

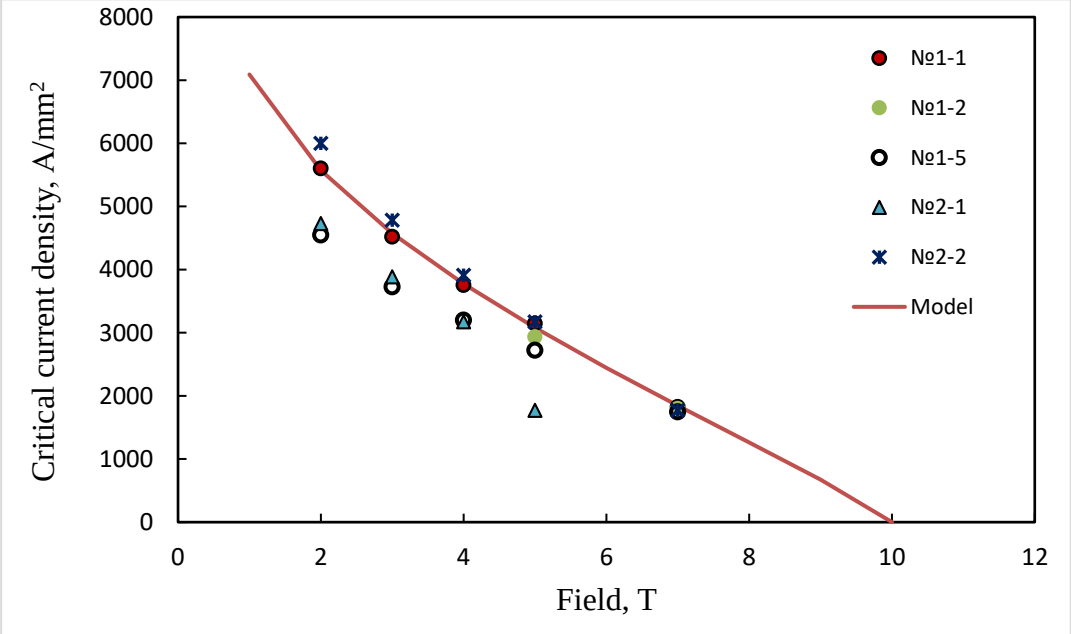

FIG. 3. Field dependency of the 31-filament model wire

2.2 Field dependencies $J_c(B)$ for the monolithic wire of the test and production batches

The estimation results of critical current density J_c (A/mm^2) of the test and production batches of monolithic wires (Fig. 1) are shown in Table 4 and Fig. 4.

TABLE 4

Critical current (A) and CV values for Nb-Ti of the test (1-c3-37-1-18) and production batches of the monolithic wire with the cross section of 2.02×3.25 mm

B(T)	1-C3-37-2-18 к1	1-C3-37-3-18 к1	1-C3-37-4-18 к1	Test (round wire)	Test (without twisting)	Test (twisted wire)
10	58	70	65	58	-	60
9.5	169	-	-	179	194	181
9	331	386	364	357	375	358
8.5	538	-	-	590	611	584
8	768	824	790	-	-	-
7.5	-	1068	1031	-	-	-
CV (share of Nb-Ti filaments)	0.1275	0.1315	0.1295	0.1315	0.1315	0.1315

The field dependency of critical current density $J_c(B)$ for test specimens of the monolithic wire was based on the solutions of the equation (1) for the model wire, and is shown in Fig. 4 together with experimental values $J_c(B)$ that were determined with consideration of the factor of Nb-Ti content in the wire (Table 4).

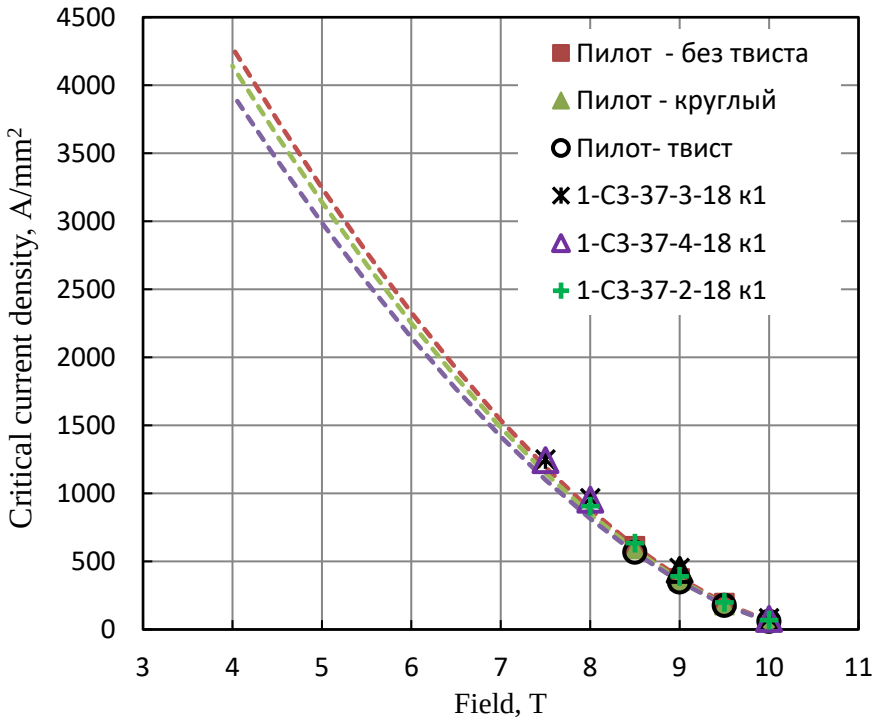

Пилот – без твиста	Test - no twisting
Пилот - круглый	Test - round
Пилот - твист	Test - twisted

FIG. 4. The dependency $J_c(B)$ (experimental and estimated) of the monolithic wire

The developed dependency $J_c(B)$ indicates that the extrapolated values $J_c(B)$ in a magnetic field of 5 T are approximately 3000 A/mm^2, however, when extrapolation of dependency $J_c(B)$ beyond experimental data leaves an uncertainty; the obtained value is still an imputation. As was stated above, direct measurements of critical current are limited by current intensity of about 1300 A, and are not possible for the field of 5 T. Due to this, critical current of production batch specimens in the 5 T field was determined by the magnetization measurement method.

2.3 Field dependencies of monolithic wire magnetization *M(B)* taken from production batches

Measurement of magnetization *M*(*B*) of a short (11 mm) specimen of monolithic wire were carried out using a vibrating-coil magnetometer in the magnetic field of (-5 T, +5 T). The cylinder of the vibrating-coil magnetometer holding the specimen was submerged in liquid helium at the temperature of 4.2 K. The dependency *M*(*B*) is shown in Fig. 5. It shows that magnetization loops of the two production specimens are virtually identical; magnetization amplitude under 5 T is 7.5 and 8 mT for specimens *1-C3-37-2-18 and 1-C3-37-3-18*, respectively.

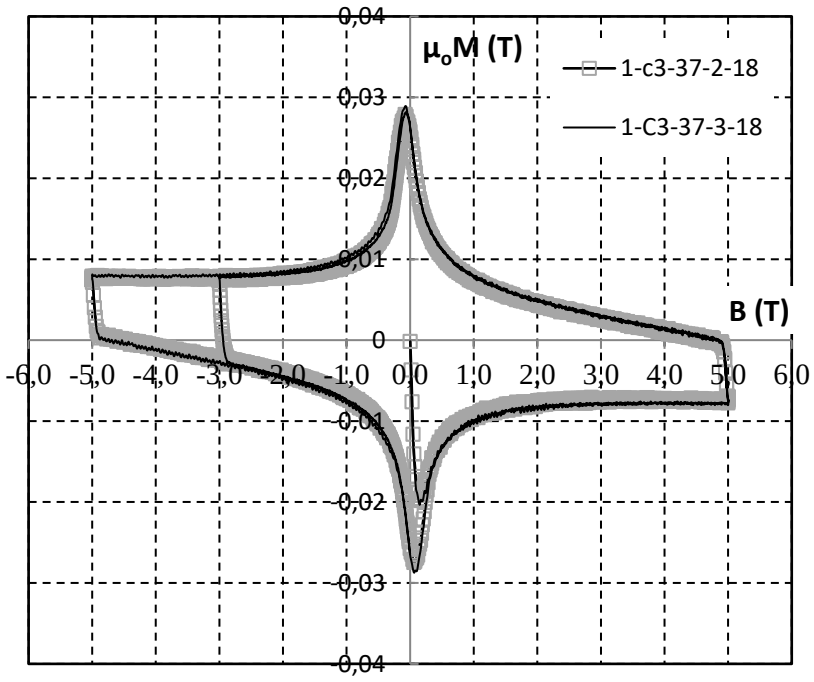

FIG. 5. Dependency of $\mu_o M(B)$ for production grade wires 1-C3-37-2-18 and 1-C3-37-3-18

According to [3], engineering critical current density (J_{c_e}) the magnetization amplitude and the effective filament diameter are tied within the correlation (2)

$$d_{eff}(B) = \frac{3\pi \cdot \Delta M(B)}{4\mu_0 \cdot J_{c\_e}(B) \cdot} \qquad (2)$$

Here, ΔM is the value of magnetization amplitude A/м; μ_0 is the magnetic constant ($1.25663706 \cdot 10^{-6}$ h/m), d_{eff} is the effective diameter of filament in meters; J_{c_e} *is* the engineering critical current density A/m^2, i.e., current density over all the cross section of the superconductor.

The equation (2) has two interrelated unknown qualities – J_{c_e} and d_{eff}. Assuming the average diameter of an Nb-Ti filament calculated on the basis of the total area wire cross-section and the total number of filaments as d_{eff}, the intensity of critical current may be estimated. The estimation should account for possible deviations due to the actual form and distribution of filament diameters. The solution of the equation 2 with allowances made for the minimum and the maximum filament diameter is shown in Table 5.

TABLE 5

Estimated values of critical current density (A/mm^2) in a 5 T field using the formula 2

Filament diameter, μm		*1-c3-37-2-18 (CV=0.1275)* ΔM=7.5 mT		*1-c3-37-3-18 (CV=0.1315)* ΔM=8 mT	
		J_{c_e}*(A/mm^2)*	J_c*(A/mm^2)*	J_{c_e}*(A/mm^2)*	J_c*(A/mm^2)*
$Ø_{min}$	36.9	380	2914	404	3187
$Ø_{av}$	38.4	365	2806	389	3061
$Ø_{max}$	39.1	358	2753	382	3006

Table 5 shows that current density determined from magnetization has the range related to the span of filament diameter values. Nevertheless, absolute values of critical current density align well with the extrapolated value of critical current in a 5 T field which was determined using direct transport measurements (Fig. 4).

2.4 Determining critical current density in operational conditions of the CBM magnetic winding

As we mentioned in the introduction, the maximum achievable field at the CBM magnet is 3.25 T with operating temperature just above boiling temperature of liquid helium, specifically, 4.5 K. In order to determine J_c*(4.5 K; 3.25 T)* under the operating conditions of the magnet, the temperature/field dependency of the critical current density J_c*(T, B) must be determined.* The equation based on the temperature-field dependency of the pinning force [1] is used to solve this problem.

$$J_c(B,T) = \frac{C}{B} b^{\alpha} (1-b)^{\beta} (1-t^{1,7})^{\gamma} \qquad (3)$$

where $t=T/T_c$ and $b=B/B_{c2}$ are temperature and magnetic field adjusted for critical characteristics of the Nb-Ti superconductor, the critical temperature (T_c) and the upper critical field B_{c2}. C is the scaling constant; α, β and γ are free parameters dependent on the composition and structure of the material.

Thus, in order to determine the value of the function $J_c(T, B)$, an optimal combination of the six parameters must be selected. Two of the parameters, T_c and B_{c2}, must be close to actual critical characteristics of the specific wire.

To find a more accurate solution to the equation (3), the voltage-temperature characteristic of the monolithic wire was measured after the outer copper layer has been removed from it in order to increase residual resistance of the specimen (Fig. 6). Using the characteristic, critical temperature of the superconducting junction T_c was determined.

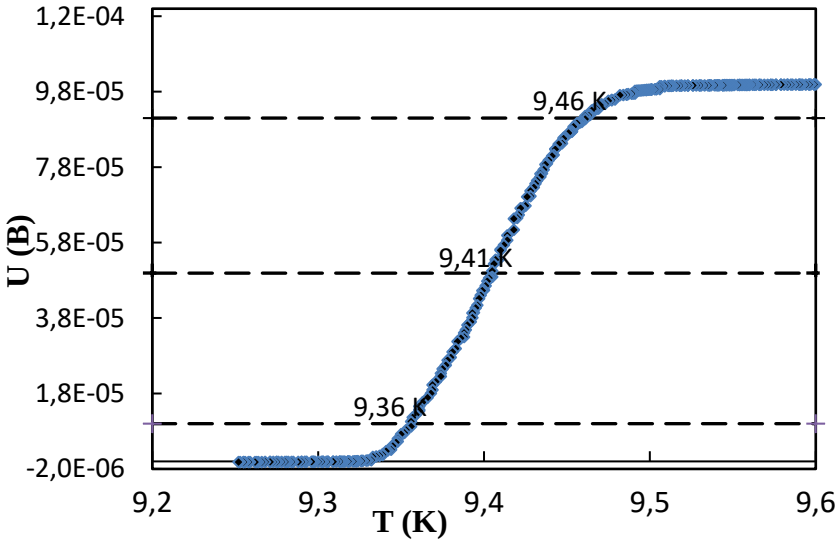

FIG. 6. Voltage-temperature characteristic (VTC) of the monolithic version of wire T_c = 9.41 K was determined using the medium amplitude of the phase transition

The value of the upper critical field B_{c2} was determined using the Cramer function and experimental values of $J_c(B)$ in production grade specimens *1-c3-37-2-18; 1-c3-37-3-18* and *1-c3-37-4-18* (Fig. 7 and Table 4).

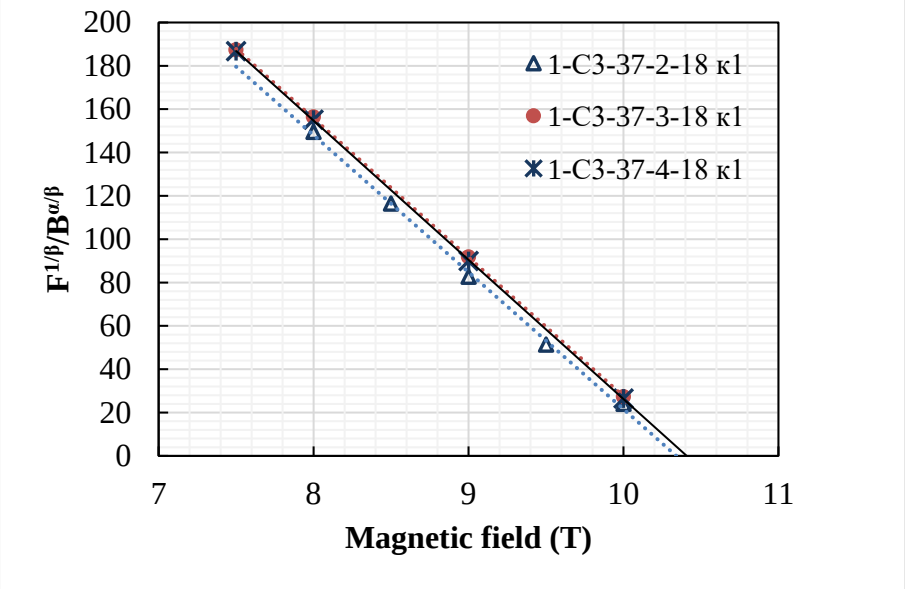

FIG. 7. Cramer function for production grade specimens of the monolithic wire for the determination of B_{c2} (4.2 K)

Estimated values of B_{c2} *(4.2 K),* that were determined using the Cramer function, as well as B_{c2} *(0 K)* and B_{c2} *(4.5 K),* obtained by way of conversion using the formulas *(4)* and *(5),* and values of the scaling constants are shown in Table 6.

$$C(T) = C_0\left(1 - \left(\frac{T}{T_c}\right)^{1,7}\right)^{\gamma} \quad (4)$$

$$B_{c2}(T) = B_{c2}(0)\left(1 - \left(\frac{T}{T_c}\right)^{1,7}\right) \quad (5)$$

TABLE 6

Estimated values of the upper critical field B_{c2} *(0 K),* B_{c2} *(4.2 K),* B_{c2} *(4.5 K)* and scaling constants

Parameter	1-С3-37-2-18 к1	1-С3-37-3-18 к1	1-С3-37-4-18 к1
C (4.2 K)	71,568	74,449	74,291
B_{c2} (4.2 K), T	10.3	10.4	10.4
C (0 K)	125,096	130,131	129,857
B_{c2} (0 K), T	13.9	14.0	14.0
C (4.5 K)	66,270	68,938	68,792
B_{c2} (4.5 K), T	9.9	10.0	10.0

Based on the data of Table 6, the critical current density in the operating conditions of the magnet system's winding was determined using the formula (3) (values for wires taken from various batches are shown in the summary Table 7.)

TABLE 7

Final estimation of J_c (4.5 K; 3.25 T) and I_c (4.5 K; 3.25 T) of production batch wires

	1-С3-37-2-18 к1	1-С3-37-3-18 к1	1-С3-37-4-18 к1
J_c (3.25 T, 4.5 K)	**4284**	**4448**	**4440**
CV for Nb-Ti	0.13	0.131	0.127
I_c (3.25 T, 4.5 K)	3656	3825	3701

Thus, the level of critical current within production grade wires under the operating conditions is more than 3.5 kA. This value may serve as the basis for the estimation of a magnetic system, accounting for its configuration, thermal margin and other operational parameters.

Conclusion

Superconductors of the test and production batches were manufactured based on Nb-Ti alloy with the cross-section of 2.02×3.25 mm and share of Nb-Ti filaments equal to 0.13, as well as a model conductor in the form of a strained 31-filament cluster, i.e., a section of a

large cross-section wire. The field dependency of critical current density of the model wire $J_c(B)$ was studied over a wide range of magnetic fields (7 to 2 T) and $J_c(B)$ of production batch wires on magnetic fields accessible for transport critical current measurements (7.5 to 10 T). Critical current density in the magnetic field of the reference intensity of 5 T was determined by extrapolation of the dependency $J_c(B)$ and with the use of a vibrating-coil magnetometer. The values obtained with the use of the two methods $J_c(5\ T)$ match within 3 to 9 %. Based on the temperature/field dependency of the pinning force $J_c(B, T)$, critical current under the operating conditions of the magnet I_c (3.25 T; 4.5 K) was determined. Its value exceeds 3.5 kA.

References

1. P. Szwangrubera, F. Toralb, E. Flocha, I. Rodriguezb, H. Leibrocka, X. Yua, W. Wuc,d, M. Lizhenc, W. Weic, X. Zhangc, B. Guod, A. Zellere, T. Weilandf « Quench calculations and measurements on the FAIR Super-FRS dipole», Physics Procedia, 36, pp. 872-877, 2012.

2. L. Bottura, "A practical fit for the critical surface of NbTi," IEEE Trans.Appl. Supercond., Vol. 10, no. 1, pp. 1054–1057, 2000.

3. R.B. Goldfarb, K. Iton "Reduction of interfilament contact loss in Nb_3Sn superconductor wire" J. Appl. Phys. Vol. 75, No 4, 1994 pp. 2115-2118.

UDC: 669.725:621.386.2

X-RAY STUDIES OF COMPOSITE MATERIALS BASED ON POROUS BERYLLIUM

E.V. Kozlova [1], M.S. Sheverdyiaev[1], A.A. Semyonov[1], V.V. Gorlevskiy[1], A.V. Laushkin [1], A.A. Chebotaryov [1], V.V. Volkov [2]

[1]SC "A.A. Bochvar High-Technology Research Institute of Inorganic Materials", Moscow

[2]FRC Crystallography and Photonics of the RAS, Moscow

Production methods, structural properties and the elemental composition of the "porous beryllium -- nanodiamond" composite materials were studied. The materials show promise in x-ray optics applications. Specimens with various nanodiamond content were studied. Using electronic microscopy, it was determined that the composite material has the form of a porous beryllium matrix with nanodiamonds dispersed within it. Specimens with various nanodiamond content were studied. It was determined that the composite materials have a relatively higher intensity of small-angle X-ray scattering than pure beryllium or detonation diamond individually. Scattering intensity curve forms and irregularity size distribution figures estimated on the basis of the curves indicate that the composite material beryllium-nanodiamond is a promising material for speckle suppression at synchrotron tomographic stations.

Keywords: porous beryllium, detonation nanodiamonds, composite material, SAXS.

Beryllium is a material of global strategic importance. Due to its unique properties, beryllium is used in energy engineering, space technologies, the military industrial sector, synchrotron-based research and other fields of research and engineering.

JSC VNIINM possesses vast experience of working with beryllium and its compounds, and has achieved several breakthroughs concerning the production of beryllium-based materials.

This study presents data related to the research of beryllium-containing composite materials based on technologies of beryllium hydride application [1].

Materials and Procedures

JSC VNIINM has developed a process of production of a unique material -- high-porosity microcellular beryllium with a nanocrystalline structure [2]. The process of porous beryllium production is based on the process of metastable beryllium hydride (BeH_2) pyrolysis which occurs in accordance with the following equation: $BeH_2 \rightarrow Be+H_2$ (ΔH= -(18.86±0.05) kJ/mol). As pyrolysis degree increases in the BeH_2-Be system, the content of beryllium metal increases as well, its viscosity rises steeply, and the resulting cellular structure settles (hardens) in space. At the final stage of pyrolysis, pores emerge within the

walls (partitions) that separate the cells [3]. As the result, the final structure of porous beryllium includes both large interparticle pores with the size of a few microns and pores with the size of about 100 nm concentrated within the cell walls. Data of mercury porosimetry confirm that the structure of porous beryllium includes pores with sizes ranging from 0.01 um to 1 um, with the average size of 0.2 um. (Fig. 1).

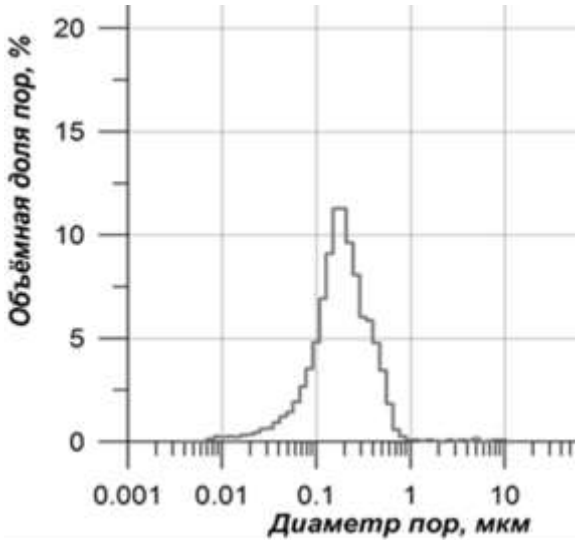

Объемная доля пор, %	Volume of pore fraction, %
Диаметр пор, мкм	Pore diameter, um

FIG. 1. Sizes of high-porosity beryllium according to mercury porosimetry

Due to its nonuniform structure and radiotransparency, porous beryllium may repeatedly dissipate x-rays that pass through it. This provides for its use as a speckle-suppressing material for the devices serving to remove artifacts from transmission type images [4].- When such devices are used in x-ray studies that use full-field x-ray microscopy, the resulting images enjoy shading correction, which allows to obtain more comprehensive information on the object. The operation theory of this type of devices is based on the degree of radiation coherence owing to its small-angle scattering on structural irregularities (pores, pore walls, grains) of the material used. That is why the number of structural irregularities in the beryllium matrix needs to be increased to obtain an artifact-free image. To achieve this, the beryllium matrix was impregnated with detonation nanodiamonds that have dimensioning specifications of about 5 nm [5-8]. The detonation nanodiamonds were chosen because the used material should possess the highest possible degree of X-ray absorption.

The composite material is produced by heat treatment of the pre-pressed mixture of the nanodiamond powder and beryllium hydride. Preceding blending of the initial components to improve the homogeneity of the composition is carried out in a liquid medium (hexane), followed by drying at room temperature for 24 hours to remove the solvent. After the heat treatment, the composite material forms a microcellular structure in which the foamed beryllium plays the role of a porous grillwork with the nanodiamond phase particles distributed within it.

During the studies, specimens of the beryllium-nanodiamond composite material of four differing compositions was obtained, with the content of the filler of 5, 25, 45 and 55% by weight, respectively.

The obtained specimens of the composite material and the initial detonation diamond powder were studied at a Philips XL-30 scanning microscope/microprobe analyzer under the accelerating voltage of 30 kV and the emission current of 50 μA. To determine the composition of the specimens, a microroentgen spectral analysis was conducted using an energy dispersive spectrometer (EDS) with a Sapphire detector.

The X-ray scattering intensity of the composite specimens was measured at AMUR-K automatic small-angle X-ray diffractometer which featured a single-coordinate position-sensitive detector ODZM operating at a fixed emission wavelength λ equal to 1.542 Å (the CuKα line of the fine-focus tube with a copper anode and a monochromator made of pyrolytic graphite) and the Kratki collimation system [9]. Estimations of size variations of the irregularities were also performed based on the small-angle X-ray scattering data. The estimations were performed using the POLYMIX software, this is an extension of MIXTURE software [10].

Obtained results and discussion

According to literature data [5,11,12], detonation nanodiamond particles tend to form agglomerations of submicronic and micron sizes due to their high surface energy. Presence of such aggregations in the initial nanodiamond powder (Fig. 2) was confirmed by the scanning electron microscopy method.

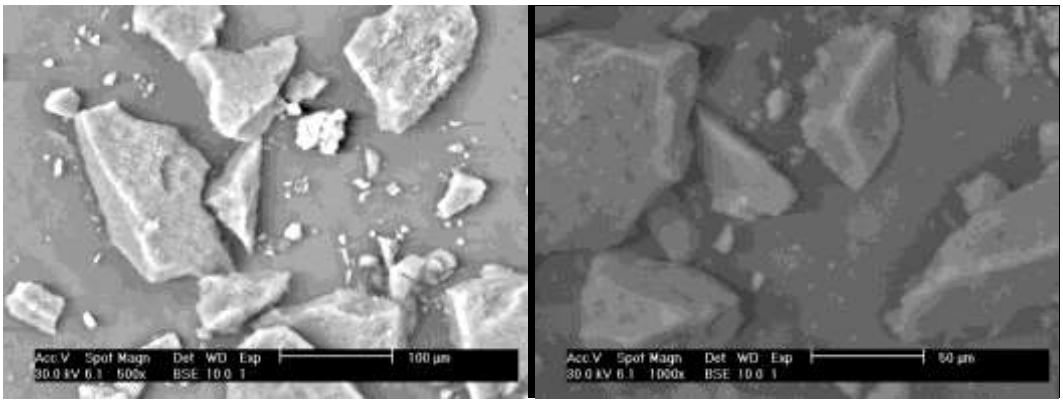

FIG. 2. SEM of nanodiamond powder

Microscopic studies of the composite material specimen fracture with diamond filler content of 55% wt are shown in Fig. 3. The surface structure of the fracture was examined, and its element analysis was performed.

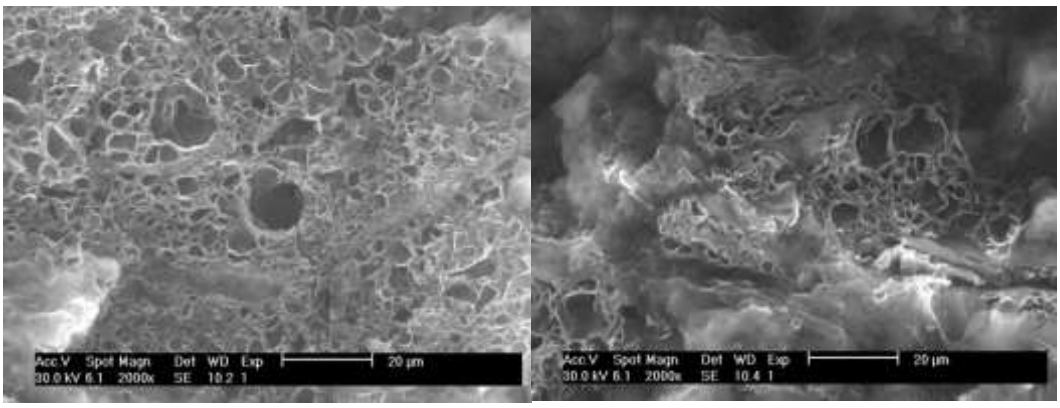

FIG. 3. SEM of the composite specimen

Fig. 3 shows that the sponge-like structure of the obtained composite material is similar to the structure of porous beryllium and its pore sizes are rather heterogeneous. According to the elemental analysis data (Fig. 4), the carbon phase occurs in various areas along the height of the composite's fracture, and the content of carbon in different locations varies from 69 to 81% wt. This indicates a relatively uniform distribution of nanodiamond particles in the beryllium matrix.

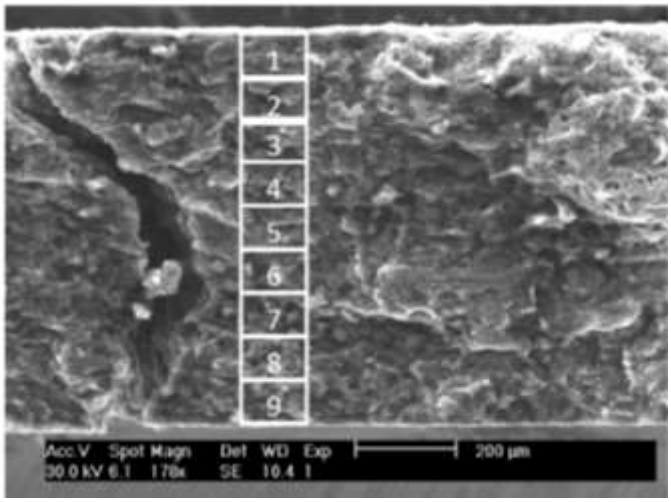

1	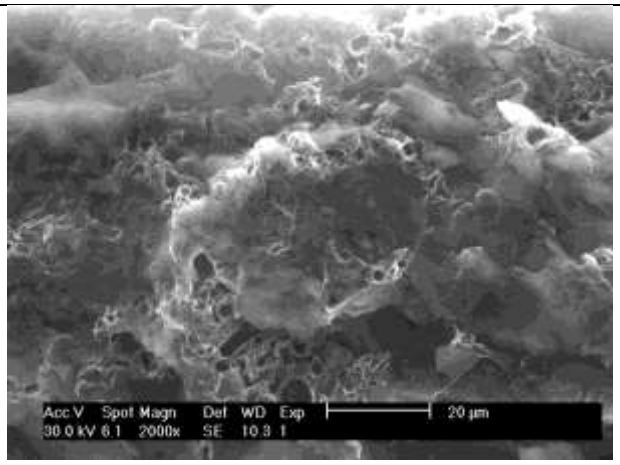	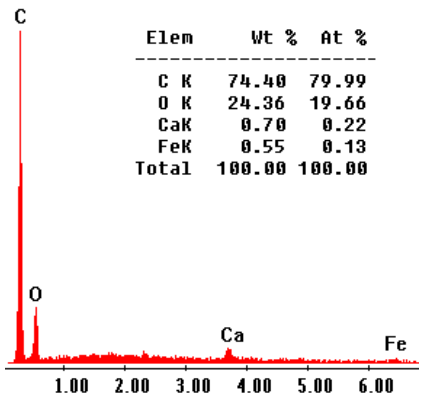

Elem	Wt %	At %
C K	74.40	79.99
O K	24.36	19.66
CaK	0.70	0.22
FeK	0.55	0.13
Total	100.00	100.00

2	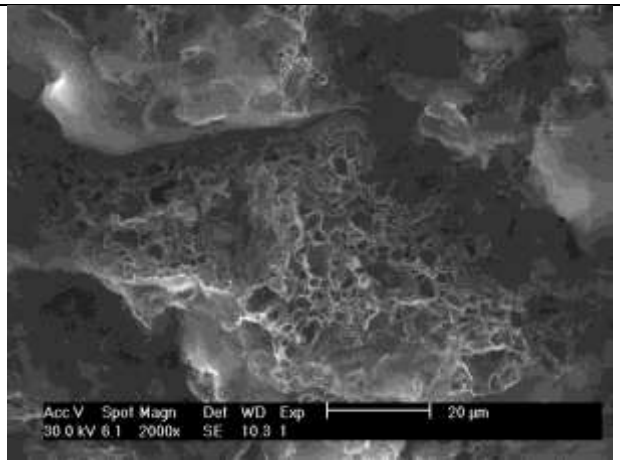	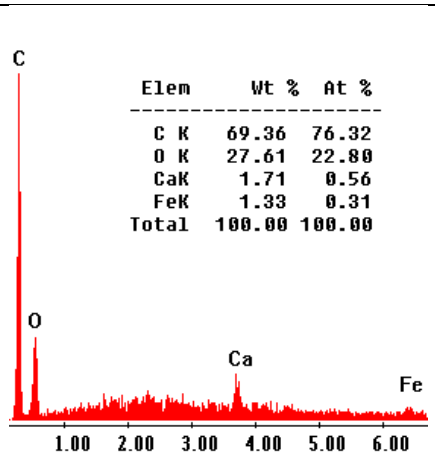 Elem Wt % At % C K 69.36 76.32 O K 27.61 22.80 CaK 1.71 0.56 FeK 1.33 0.31 Total 100.00 100.00
3	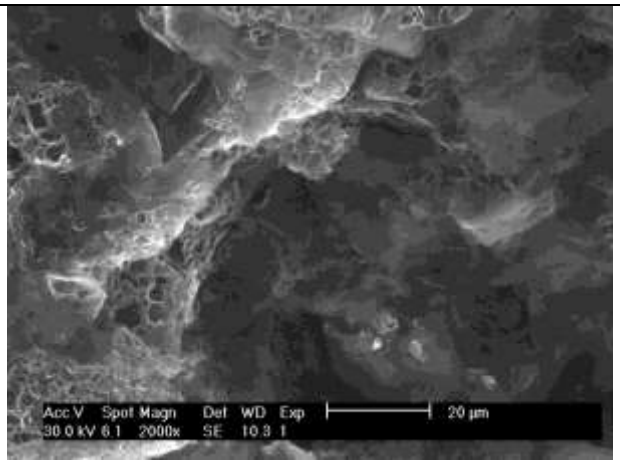	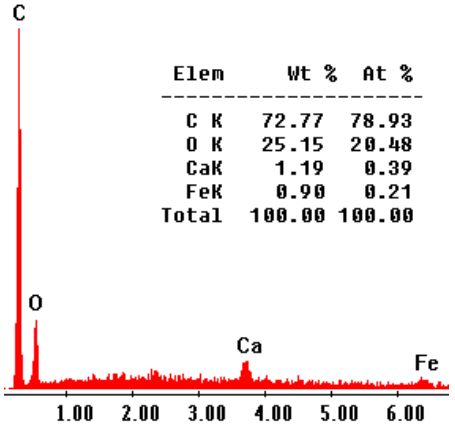 Elem Wt % At % C K 72.77 78.93 O K 25.15 20.48 CaK 1.19 0.39 FeK 0.90 0.21 Total 100.00 100.00
4	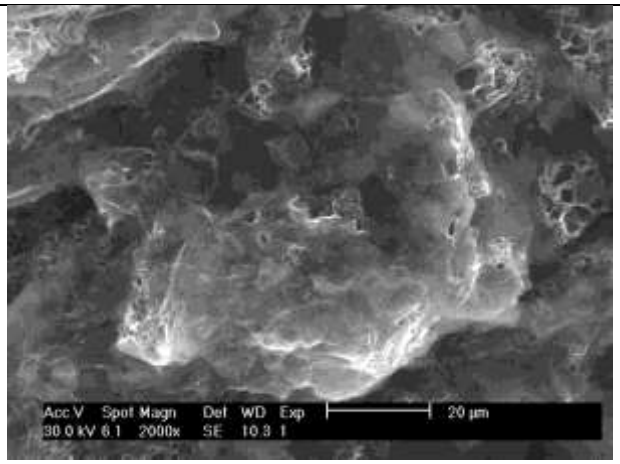	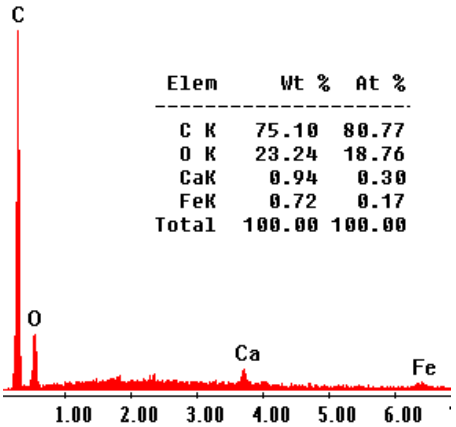 Elem Wt % At % C K 75.10 80.77 O K 23.24 18.76 CaK 0.94 0.30 FeK 0.72 0.17 Total 100.00 100.00

5	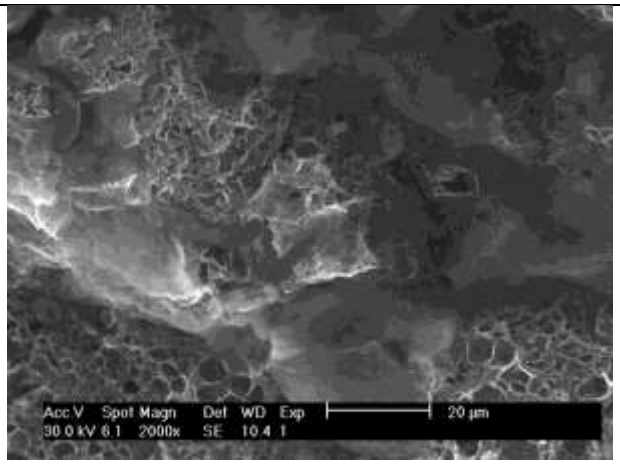	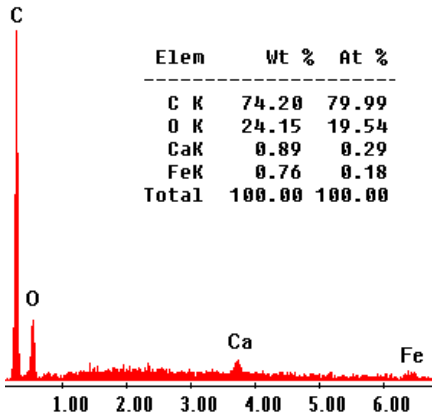 Elem Wt % At % C K 74.20 79.99 O K 24.15 19.54 CaK 0.89 0.29 FeK 0.76 0.18 Total 100.00 100.00
6	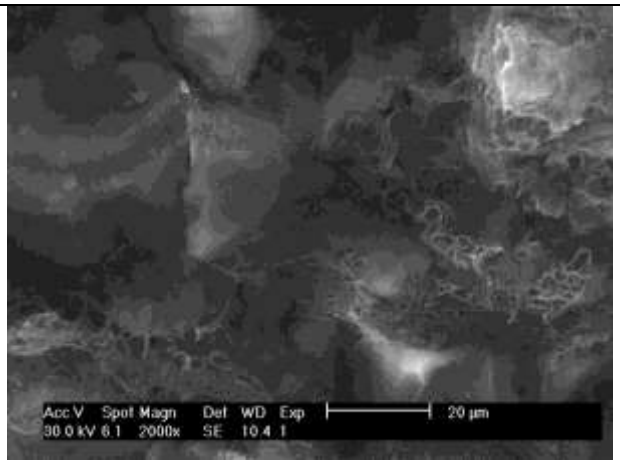	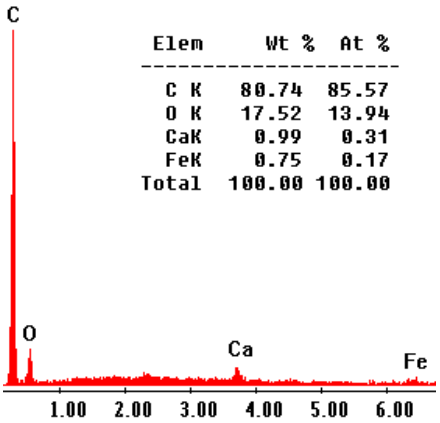 Elem Wt % At % C K 80.74 85.57 O K 17.52 13.94 CaK 0.99 0.31 FeK 0.75 0.17 Total 100.00 100.00
7	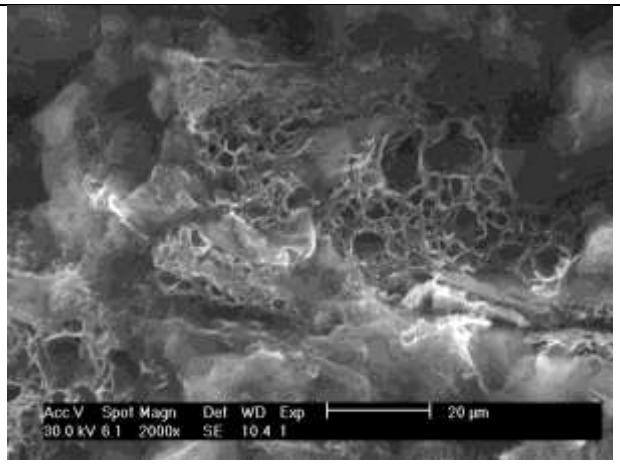	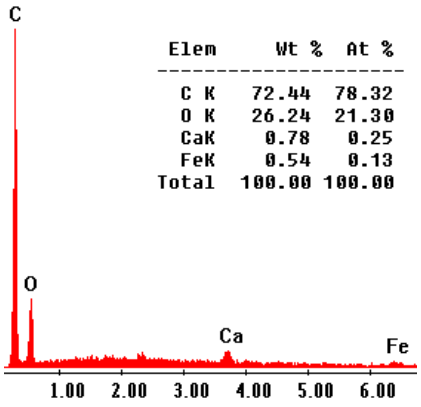 Elem Wt % At % C K 72.44 78.32 O K 26.24 21.30 CaK 0.78 0.25 FeK 0.54 0.13 Total 100.00 100.00

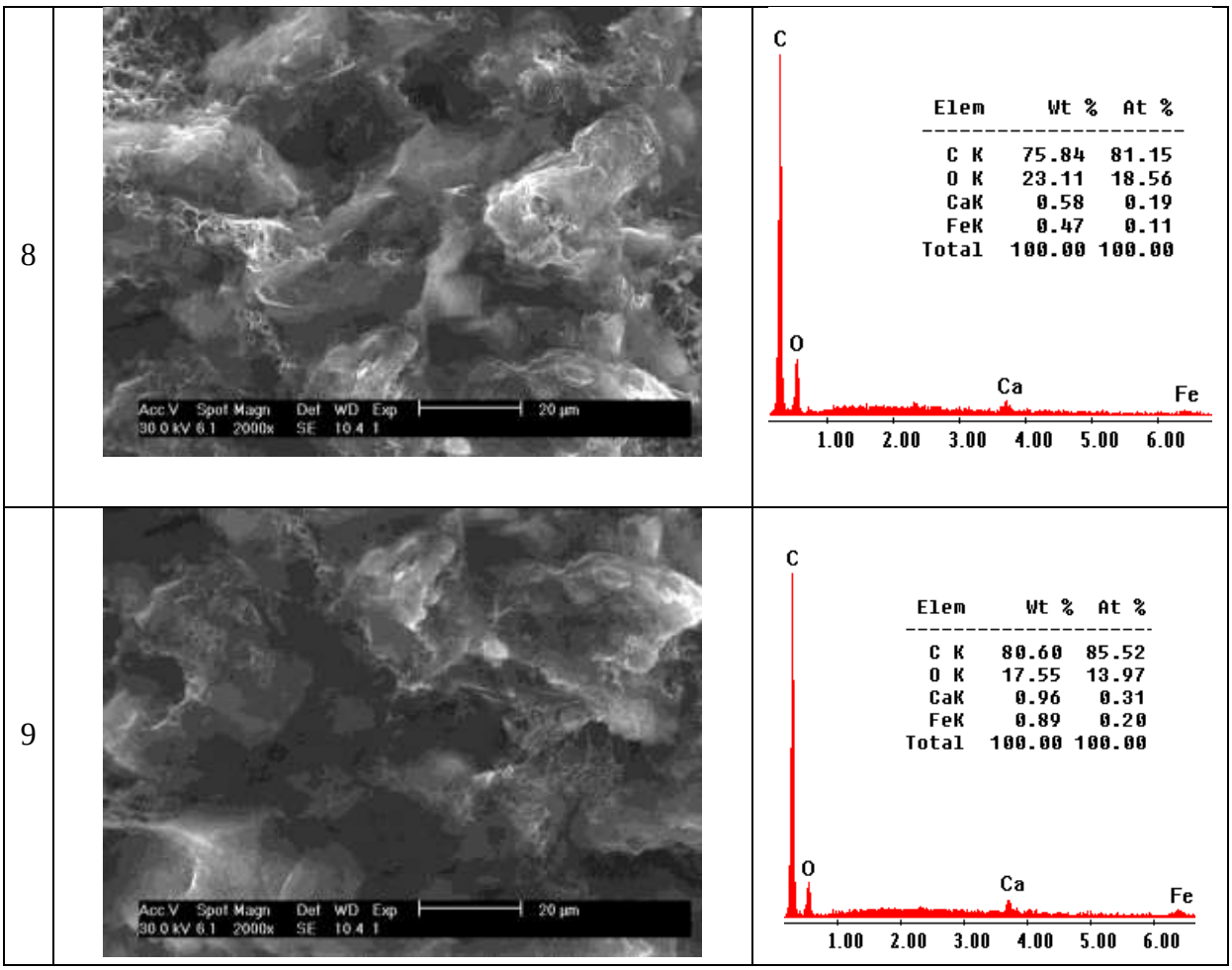

FIG. 4. Elemental analysis of the composite specimen

Small-angle X-ray scattering (SAXS) curves represented in the coordinates of "intensity logarithm - module of vector of scattering" in inverted nanometers ($s = 4\pi \sin\theta/\lambda$, 2θ - angle of scattering, λ – wavelength), are shown in Fig. 5 and 6. Fig. 5 shows that , an increase of SAXS intensity is observed within the range of 0.5 to 2.0 nm^{-1} with the increase of the nanodiamond content in the composite material.

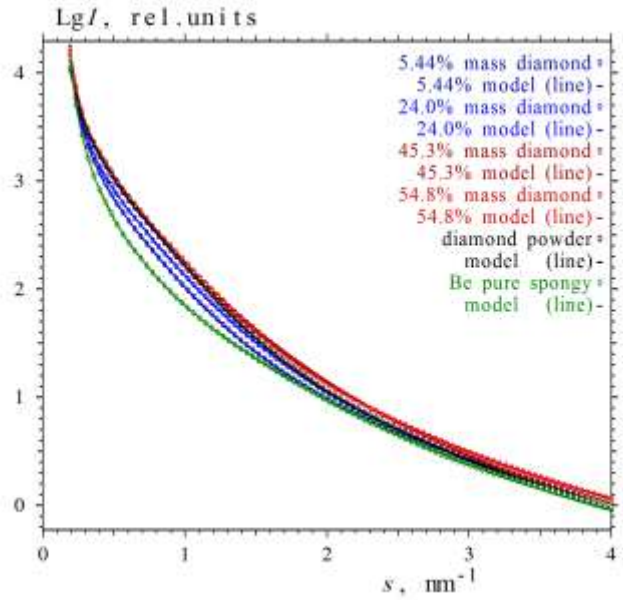

FIG. 5. Intensity of small-angle X-ray scattering from the specimens of porous beryllium doped with nanodispersed diamond, the initial diamond powder and plain porous beryllium

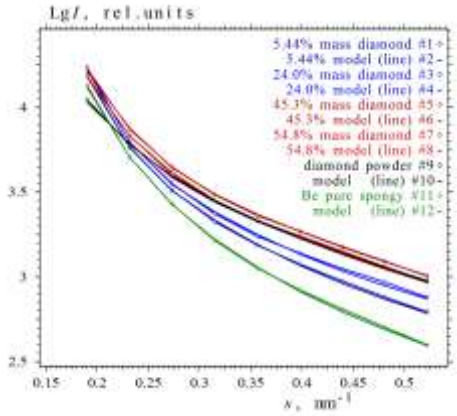

FIG. 6. Initial area of intensity of small-angle X-ray scattering from the specimens of porous beryllium doped with nanodispersed diamond, the initial diamond powder and plain porous beryllium

It is noteworthy that within the range of narrow angles at $s < 0.5$ nm^{-1} the intensity of scattering of the composite material specimens having the nanodiamond content of 45 to 55% wt is much higher than that of porous beryllium matrix or diamond dust taken separately (Fig. 6). The increased scattering at initial angles, as compared to wide-angle scattering should be considered an advantage of the material since the work beam of x-ray stations is formed within the area which lies close to the initial beam.

As we can see, in the neighborhood of the central x-ray beam ($s < 0.25$ nm^{-1}), at the initial section of the diagrams shown in Fig 6, the scattering intensity at the composite material specimens and the beryllium matrix without a filler is not substantially different, however, it exceeds the scattering intensity observed in the detonation nanodiamond powder. Within the value range of s 0.25 nm^{-1} to 0.5 nm^{-1}m the intensity of scattering of the beryllium

matrix reduces, and is lower than the scattering intensity of diamond powder. That being said, the composite material demonstrates high values of scattering intensity within the whole small-angle scattering range (*s* of 0 to 0.5 nm^{-1}) that exceed those of the beryllium matrix without a filler and of detonation nanodiamond powder.

The analysis of the dependency of the scattered radiation intensity on the angle of scattering allowed us to estimate the size distribution of nanometric irregularities by their relative content in the studied specimens of composite materials of various composition. The obtained data are shown in Fig. 7.

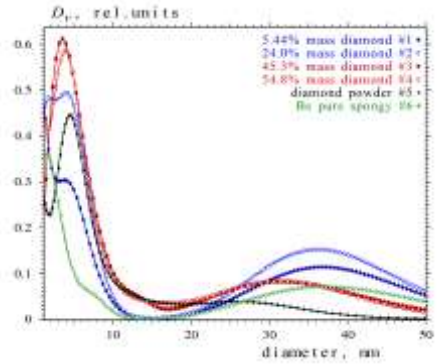

FIG. 7. Distribution of scattering irregularity diameters

It can be easily seen that as the content of the nanodiamond filler increases within the beryllium matrix, the proportion of irregularities with the average diameter of 4 to 5 nm increases as well. Peaks of the curves at average diameters of 30-50 nm are apparently caused by the contribution of the porous structure of beryllium.

An analysis of the obtained results lets us deduce that the composite material comprising a beryllium matrix impregnated with detonation nanodiamonds shows a higher SAXS intensity than the same materials taken separately. This evidences a synergic effect of the matrix and the filler of the composite material.

Thus, the composite material “beryllium -- nanodiamonds” is deemed advantageous to the development of effective speckle suppression devices.

Conclusions

1) For the first time ever, materials based on porous beryllium impregnated with detonation nanodiamonds were obtained and studied.

2) The effect of the nanodiamond particle content on the behavior of SAXS in the “beryllium-nanodiamond” composite specimens was determined.

3) Distribution of irregularities within the volume of the produced materials was estimated.

4) It was determined that the composite materials with the content of nanodiamonds of 44-55% wt show a relatively higher intensity of small-angle X-ray scattering than pure porous beryllium or detonation diamond powder taken separately.

5) The obtained data evidence that the composite material “beryllium -- nanodiamonds” is advantageous to the development of enhanced speckle suppression devices used in synchrotron-based research.

Small-angle scattering was measured with the use of equipment of the Collective Use Center of FRC Crystallography and Photonics of the RAS with the support of the Ministry of Science and Higher Education, as part of activities performed under the Government Assignment performed by FRC Crystallography and Photonics of the RAS in the field of investigation of x-ray scattering and data interpretation.

References

1. A.A. Semenov. Beryllium Technology at Bochvar All-Russia Research Institute for Inor-ganic Materials: Past, Present, Future. Atomic energy. 2015. vol. 119. No.5. Pp. 255-259.

2. Yu.E. Markushkin , M.I. Solonin, V.V. Gorlevsky, V.A . Gorokhov, D.A.,Davydov, G.N. Nikolaev. Method for the production of porous beryllium goods. Patent RF, No 2106931. 1998

3. V.V. Gorlevsky, A.S. Vorontsov, A. V. Zabrodin, Yu.E. Markushkin, et al. Structure and properties of high-porous (foamed) nanoberyllium.Selectas of VNIINM, Jubilee collection dedicated to the 100th anniversary of Russian largest scientist and metal expert Academician Andrei Anatolyevich Bochvar. Vol. 2. Moscow. VNIINM Publ..2002, Pp 89-99 (In Russian).

4. Highly porous nanoberyllium for X-ray beam speckle suppression / A. Goikhman, I. Lyatun, P. Ershov and others // J. Synchrotron Rad. – 2015 – № 22 – P. 796-800

5. Vul' A. Y. Detonation Nanodiamonds: Science and Applications / A. Y. Vul’, O.A. Shenderova //Pan Stanford Publishing – 2013. / P. 320

6. G.V. Sakovich Detonation nanodiamonds. Synthesis. Properties. Application [text] / G.V. Sakovich, A.S. Zharkov, E.A. Petrov //Industrial Research and Engineering. - 2011. No. 4. pp. 53-61.

7. V.Yu. Dolmatov Ultra-disperse detonation synthesis diamonds: properties and application [text] / V.Yu. Dolmatov - Uspekhi Himii – 70 (7) – 2001 – pp. 687–708

8. V.Yu. Dolmatov Detonation nanodiamonds: synthesis, composition, properties and application [text] / V.Yu. Dolmatov - Uspekhi Himii – 76 (4) – 2007 – pp. 375–397

9. L.Yu. Mogilevskiy Automatic small-angle X-ray diffractometer with position-sensitive detector [text] / L.Yu. Mogilevskiy, A.T. Dembo, D.I. Svergun et al. // Crystallography. – 1984. – vol. 29. – No. 3. pp. 587-591

10. Svergun, D. I A small angle X-ray scattering study of the droplet–cylinder transition in oil–rich sodium bis(2–ethylhexyl) sulfosuccinate microemulsions / D. I. Svergun, P. V. Konarev, V. V. Volkov, M. H. J. Koch, W. F. C. Sager, J. Smeets, E. M. Blokhuis // J. Chem. Phys. – 2000. – V. 113. – P. 1651 – 1665

11. Chang L. Confirmation of the electrostatic self-assembly of nanodiamonds / L. Chang, E. Osawa, A.S. Barnard // Nanoscale, – 2011, – 3, P. 958–962

12. Aleksenskii A.E. Ultradisperse Diamond Cluster Aggregation Studied by Atomic Force Microscopy / A.E. Aleksenskii, V.Yu. Osipov, A. T. Dideikin, A.Ya. Vul’, G. J. Adriaenssens , V. V. Afanas’ev // Technical Physics Letters. – Vol. 26, – No. 9, – 2000, – P. 819–821